THE STRUCTURAL AND PETROLOGIC EVOLUTION OF THE RED HILLS ULTRAMAFIC MASSIF: COUPLED MELT MIGRATION AND DEFORMATION DURING SUBDUCTION INITIATION

A Dissertation

by

ERIC DONALD STEWART

Submitted to the Office of Graduate and Professional Studies of
Texas A&M University
in partial fulfillment of the requirements for the degree of

DOCTOR OF PHILOSOPHY

Chair of Committee,	Julie Newman
Committee Members,	Will Lamb
	Andreas Kronenberg
	Debbie Thomas
	Basil Tikoff
Head of Department,	Rick Giardino

August 2015

Major Subject: Geology

ABSTRACT

The Red Hills ultramafic massif, located on the South Island of New Zealand, contains a three-stage history of overprinting deformation which occurred during the onset of Permian subduction along the Australian-New Zealand portion of the Gondwanan margin. Geologic mapping of the massif delineates four compositional units which are, from east to west: Massive harzburgites (two tarns harzburgite); Plagioclase lherzolites and plagioclase harzburgites (plagioclase zone); Banded dunite, harzburgite, and lherzolite (Plateau complex); Banded dunite and harzburgite (Ellis Stream complex). Geothermobarometry, major and trace element geochemistry, geochronology, and structural analysis are combined with the geologic mapping to place the history of the rocks in an incipient subduction environment.

The kinematic history of the rocks is ultimately tied to transtensional plate boundary conditions imposed by the foundering of oceanic crust and initiation of subduction along an active oceanic transform margin. The style of strain accommodating transtensional deformation was largely a function of the distribution of melt during exhumation and cooling of the massif. At 1200° and at pressures >6 kbar (Stage 1), melts were homogeneously distributed, and strain was homogeneous and highly constrictional. At 1000°C and 5 kbar pressure (Stage 2), melts were focused into kilometer scale conduits, and deformation produced lineated and foliated rocks that overprinted the earlier constrictional fabrics. When no melts were present at temperatures less than 600°C (Stage 3), deformation became highly localized into

serpentinized faults. In addition to its influence on the kinematic history of the massif, the two stages of melt migration altered the composition of the massif. Early melting associated with the first stage of deformation produced depleted harzburgites with a small range in whole-rock compositions. During Stage 2, melts were channelized and initially undersaturated in orthopyroxene, producing dunite bands. During the waning phases of Stage 2, melts became saturated in clinopyroxene ± plagioclase, resulting in local refertilization of the massif. Refertilization was particularly prevalent along the margins and upper terminations of Stage 2 melt conduits, forming a refertilization front enriched in plagioclase and clinopyroxene, but presumably due to lower melt fluxes, lacking dunite bands. A key result is that melt migration, not any pre-existing compositional heterogeneity, plays a fundamental role in the kinematic history of the massif. Rather, the compositional heterogeneity within the massif is the end result of multiple episodes of melt migration and refertilization during the earliest stages of subduction. Thus the Red Hills ultramafic massif provides a pristine record of how the mantle flows and changes composition as a result of melt migration during the earliest stages of subduction.

ACKNOWLEDGEMENTS

This work was supported by NSF EAR 1419849 to Julie Newman, Basil Tikoff, Will Lamb, and Seth Kruckenberg. I gratefully acknowledge numerous helpful conversations and guidance from my committee chair, Julie Newman, as well as the rest of my committee. Field help from Basil Tikoff, Will Lamb, Virginia Toy, Seth Kruckenberg, Esther Stewart, Dana Peterson, Marco Bilia, Charlotte Buxton-Blue, and Zoe Reid-Lindroos is much appreciated. Sara Donnelly, Lindsey German, Zach Michels, Vasilis Chatzaras, Caleb Holyoke, and Gordon Medaris are thanked for helpful conversations. I also thank Ray Guillemette and Lindsey Hunt for their help and expertise on the electron microprobe. Thanks to Brent Miller for his help with geochronology. External reviews of parts of this dissertation by J. Pearce, H. Rollinson, S. Sano, S. Arai, B. Sullivan, T. Gerya, and an anonymous reviewer provided invaluable insight and helped clarify much of the text.

TABLE OF CONTENTS

Page

LIST OF FIGURES

LIST OF TABLES

CHAPTER I

INTRODUCTION

Subduction initiation remains a fundamental problem in plate tectonics. Numerous models have been proposed for initiating new subduction zones, including forced convergence along pre-existing faults (Casey and Dewey, 1984; Hall et al., 2003; Gurnis et al., 2004), spontaneous plate subsidence due to density driven differences along pre-existing faults (Stern and Bloomer, 1992; Dymkova and Gerya, 2013), and spontaneous initiation along passive margins due to sediment loading and density differences (Marques et al., 2014). Though numerical models have tested plate tectonic conditions necessary for subduction initiation, more detailed structural and petrologic investigations into how strain is accommodated and how the petrology of the nascent mantle wedge evolves have not been dealt with in much detail. Such studies have traditionally been undertaken by field workers, but field studies have been traditionally thwarted by the lack of exposure of subduction zone mantle rocks. However, significant progress has been made on understanding the genesis of ophiolites, and many studies have shown that ophiolites record supra-subduction zone fabrics that developed during subduction initiation. Sometimes these fabrics are found in close spatial relation to prior mid-ocean ridge fabrics (Choi et al., 2008), illustrating the complexity of the problem. As a result, detailed histories of mantle sections of ophiolites can be used to elucidate subduction initiation processes (e.g. Stern et al., 2012), and once the history of an

ophiolite has been worked out, such surface exposures can be used to provide key constraints to numerical models investigating subduction initiation processes.

This dissertation contains two main goals: First, to understand the geologic history of the Red Hills ultramafic massif, and its development in an incipient subduction zone setting; Second, to utilize the geologic history as a means to understand upper mantle wedge processes during subduction initiation. The dissertation is organized into three papers, each of which applies the geologic history towards a different fundamental problem or process in subduction initiation: First, how did the style of strain and degree of strain localization change with time, depth, and temperature, and what was the fundamental control on strain localization during subduction initiation; Second, how did the petrologic composition of the mantle wedge change through time, and what was the role of melts in creating a compositionally heterogeneous mantle wedge; Third, how did subduction initiate and what were the tectonic boundary conditions that drove mantle flow and deformation during subduction initiation.

CHAPTER II

LINKED KINEMATIC AND COMPOSITIONAL EVOLUTION OF THE RED HILLS ULTRAMAFIC MASSIF, NEW ZEALAND: OBLIQUELY DIVERGENT MANTLE FLOW IN A NASCENT MANTLE WEDGE

SYNOPSIS

The Red Hills ultramafic massif, part of the Permian Dun Mountain Ophiolite, New Zealand, contains evidence for overprinting deformation and melt migration occurring during the onset of subduction. Geologic mapping of the entire massif allows subdivision of the Red Hills ultramafics into four compositional members. From east to west, these are: 1) Pervasively lineated harzburgites (two tarns harzburgite); 2) Plagioclase lherzolites and plagioclase harzburgites (plagioclase zone); 3) Banded lherzolites, harzburgites, and dunites (Plateau complex); 4) Banded harzburgites and dunites with a strong planar fabric (Ellis Stream complex). A large-offset serpentinized fault, the Porter fault, separates the latter Ellis Stream complex from the rest of the compositional units.

Microstructures and field observations from the four compositional units are interpreted to reflect a record of melting and refertilization processes in the nascent mantle wedge. Geothermobarometry results and microstructures from the two tarns harzburgite suggest lineation development was coupled to melt migration. This early fabric (Stage 1) developed at approximately 1200°C and >6 kbar pressure. The linear fabric likely formed from transtensional deformation during subduction initiation. The

remaining three units record melting and refertilization processes at cooler and shallower conditions of approximately 1000°C and 4.4-5.4 kbar pressure (Stage 2). The geometry of the different mapped units delineates the areas of mantle affected by pervasive melt migration. At temperatures <600°C, the Ellis Stream complex was juxtaposed against the other ultramafic units by the late-stage Porter fault (Stage 3). Finally, I develop a model for the complex tectonic evolution of the massif, which links the compositional evolution of the massif, melt migration, and the development of deformational fabrics.

INTRODUCTION

Supra-subduction zone ophiolites are thought to form during forearc seafloor spreading at the onset of subduction (Casey and Dewey, 1984; Pearce et al., 1984; Stern and Bloomer, 1992). Conceptual models for forearc development during subduction initiation predict strongly extensional deformation as a result of space opening up above the subsiding slab (Stern and Bloomer, 1992; Stern et al., 2012). The combination of extensional decompression, followed by a flux of volatiles originating from the subducting plate, result in melting of the nascent mantle wedge (Shervais, 2001; Reagan et al., 2010). This early phase of volcanism creates new forearc lithosphere during a brief period of seafloor spreading during the incipient phases of subduction (Stern and Bloomer, 1992; Ishizuka et al., 2011).

Mantle flow that accommodates this early forearc formation is poorly understood. Numerical models have considered mantle flow during subduction initiation, but typically within a two-dimensional framework (e.g. Regenauer-Lieb et al., 2001;

Hall et al., 2003; Burov and Cloetingh, 2011). Field studies of supra-subduction ophiolites created during subduction initiation have mostly focused on melt movement and volcanism during the early stages of subduction (e.g. Shervais, 2001; Shervais et al., 2004; Dilek and Thy, 2009; Pearce and Robinson, 2010; Reagan et al., 2010; Batanova et al., 2011) with little emphasis on the structures that accommodate mantle deformation.

This paper follows the explicit suggestion of Stern et al. (2012): To study supra-subduction zone ophiolites in order to elucidate subduction initiation processes. I investigate the structures and composition of the Red Hills ultramafic massif (RHUM), which is part of the Dun Mountain Ophiolite Belt (DMOB), previously interpreted as a supra-subduction zone forearc ophiolite (Kimbrough et al., 1992; Sivell and McCulloch, 2000; Jugum, 2009). Within the DMOB, the RHUM is a particularly well-exposed ultramafic massif with minimal serpentinization, making it an excellent location to study upper mantle deformation. In this chapter, I describe results from geologic mapping, microstructural observations, and geothermobarometry in four distinct compositional units within the massif, which reveal a history of overprinting deformation synchronous with melt migration. I further interpret the deformational setting of the RHUM within an incipient subduction zone, and find that in such a setting, deformation at the map scale (km scale) is strongly coupled to the presence of melt.

GEOLOGICAL BACKGROUND

Dun Mountain ophiolite belt (DMOB)

The DMOB is part of the Eastern Province of New Zealand, which is composed

of several elongate tectonostratigraphic terranes (Fig. 1). Other than the Brook Street Terrane, which represents a Permian and Triassic volcanic arc and associated volcaniclastic sediments (Coombs et al., 1976; Houghton and Landis, 1989), most of the tectonostratigraphic terranes are made up of Latest Paleozoic through Mesozoic forearc and accretionary prism sedimentary successions (Wellman, 1956; Coombs et al., 1976). These successions are interrupted by the DMOB, which consists of a mafic crustal section and an ultramafic mantle section. The ultramafics are in fault contact with the structurally overlying mafic volcanics (Johnston, 1981; 1983; 1990, Rattenbury, 1998), with an uncertain amount of section missing. On their western margin, the mafic section of the DMOB is overlain by forearc siliciclastic and carbonate rocks of the Maitai Group (Landis, 1969; Johnston, 1981; Adams et al., 2007). Mafic intrusions into the base of the Maitai Group (Upukerora Formation) suggest sedimentation began during the waning phases of igneous activity (Jugum, 2009). On the eastern margin of the DMOB, the ultramafic section is tectonically separated from the Paleozoic to Mesozoic Caples Terrane by the serpentinized Patuki Melange (Fig. 1).

Middle Permian (285-269 Ma) plagiogranites have been dated in both the mafic and ultramafic sections along the entire length of the DMOB (Kimbrough et al., 1992; Sivell and McCulloch, 2000; Jugum, 2009). These plagiogranites are interpreted to record the eruption of the mafic section of the rocks preserved in the ophiolite (Kimbrough et al., 1992; Jugum, 2009), and immediately precede arc volcanism in the adjacent Brook Street terrane.

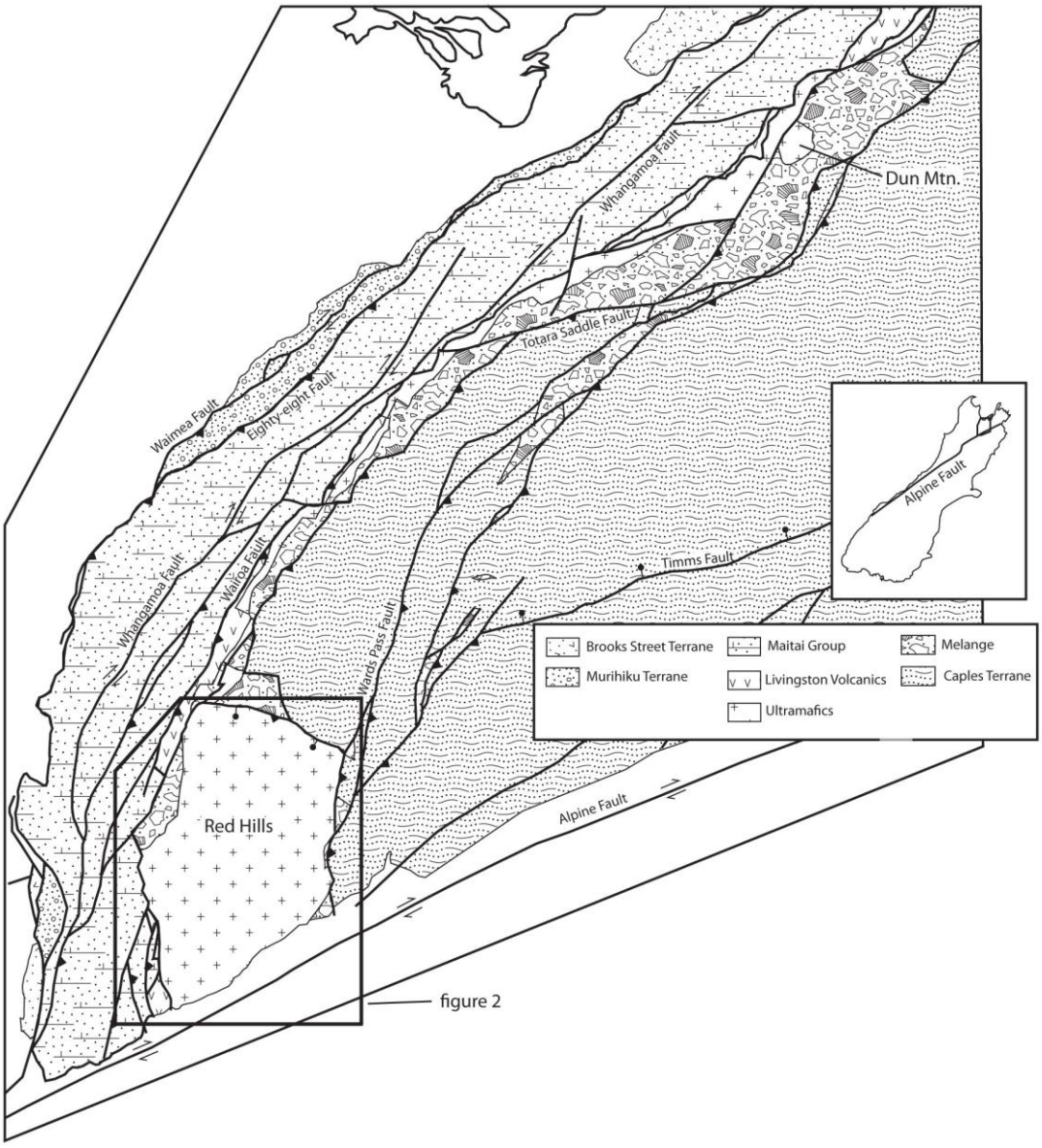

Figure 1 – Regional geologic map of the northern South Island, New Zealand. Modified from Rattenbury (1998).

Red Hills ultramafic massif (RHUM)

The Red Hills massif is an approximately 8 km wide by 12 km long ultramafic body surrounded by crustal rocks, and is located within the northern part of the DMOB (Walcott 1969; Johnston 1982; 1983; 1990). Walcott (1969) divided the ultramafics in

the Red Hills area into an eastern massive harzburgite unit and a western layered dunite and harzburgite unit that locally contains plagioclase. More recent mapping by Johnston (1982; 1983; 1990) interpreted the ultramafics of the RHUM as part of an ophiolite, and mapped faulted contacts between the western edge of massif and the crustal succession. Johnston (1990) also mapped the Porter fault, located entirely within the ultramafic section, and found that it separated distinct structural domains.

Several subsequent detailed studies attempted to ascertain the compositional and structural variations within the RHUM. Geochemical studies by Sano and Kimura (2007) and Kimura and Sano (2012) in the northern Red Hills modeled clinopyroxene and whole rock rare earth element compositions. They concluded that the massive harzburgites of the eastern massif formed from a two-phase melting history, beginning in the garnet stability field and continuing into the spinel stability field. In the layered peridotites of the western massif, they concluded the dunites formed synchronously with melting in the massive harzburgites, but were later refertilized during late-stage melt impregnation at shallow pressures within the plagioclase stability field. Webber et al. (2008; 2010) examined a ~2 km^2 area around Porter's Knob (central Red Hills, Fig. 2), and divided the area into distinct structural fabrics reflecting several episodes of overprinting deformation. Webber et al. (2008, 2010) further calculated upper mantle deformation temperatures between 750°C and 1050°C based on geothermometry results from co-existing pyroxenes.

These previous studies are limited by the lack of a synoptic view of the whole massif, and particularly the significant offset on the Porter fault. Consequently, I

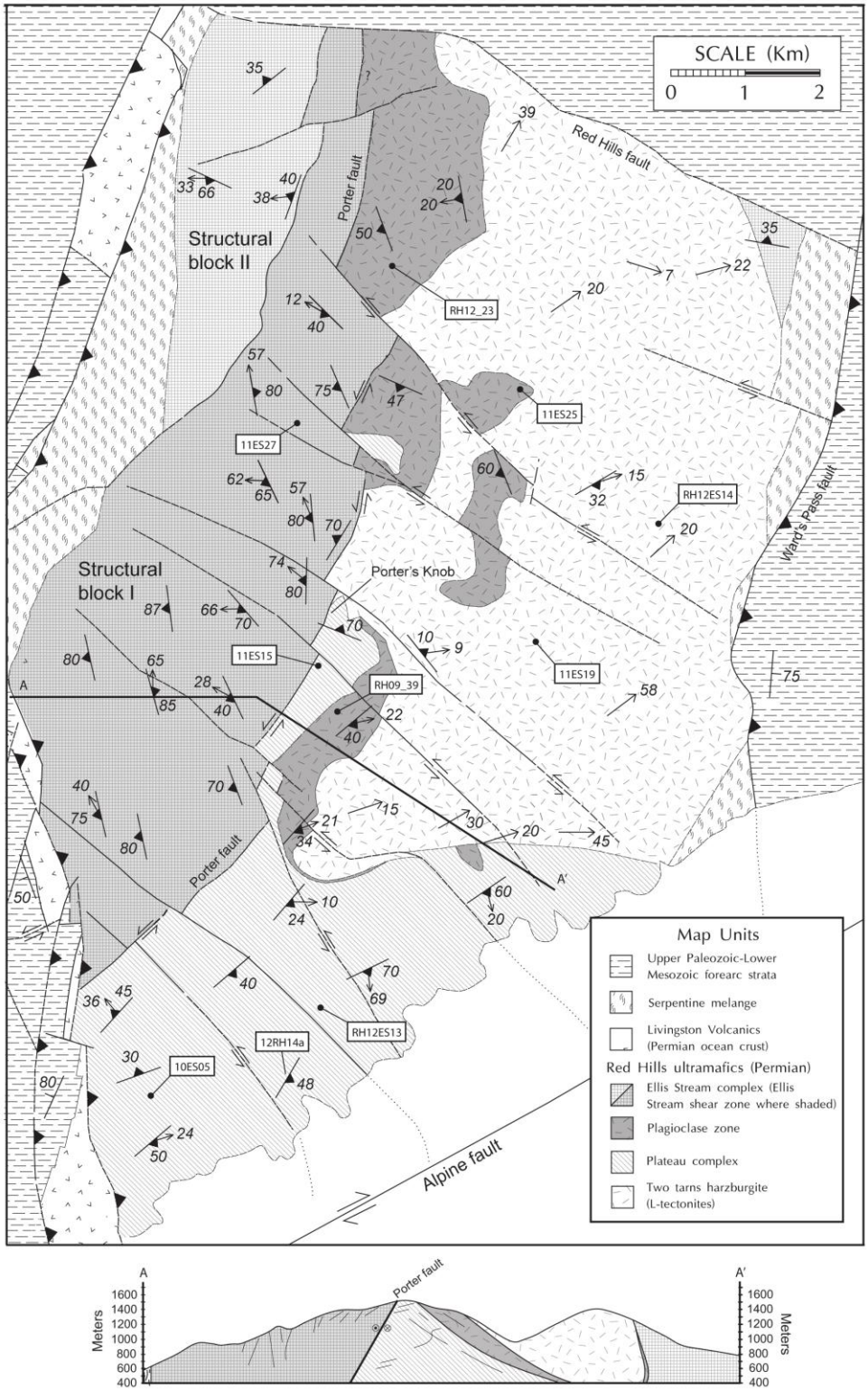

Figure 2 - Simplified geological map of the Red Hills ultramafic massif. The crustal portion of the map is modified from Johnston (1982; 1983; 1990).

conducted a comprehensive mapping of the entire massif. The new map of the internal composition and structure of the massif – and new pressure and temperature estimates – allows us to elucidate the role of melt in localizing deformation. Further, I can place the entire geologic history of the RHUM within the tectonic context of an incipient subduction zone.

COMPOSITIONAL UNITS

New geologic mapping in the Red Hills ultramafic massif (Fig. 2) delineates four distinct lithologic units that, from east to west, comprise: 1) Pervasively lineated harzburgites; 2) Plagioclase lherzolites and plagioclase harzburgites; 3) Banded lherzolites, harzburgites, and dunites; and 4) Banded harzburgites and dunites with a strong planar fabric. I hereafter refer to these informally named members as the two tarns harzburgite, plagioclase zone, Plateau complex, and Ellis Stream complex, respectively. Table 1 provides a correlation chart of previously used nomenclature for these compositional units. Full map unit descriptions and descriptions of important structures are included within a more detailed 1:20,000 scale geologic map, which accompanies this dissertation as Plate 1.

Two tarns harzburgite

Unit description

The two tarns harzburgite is composed of harzburgite, although lherzolite and dunite occur locally. This unit corresponds to the eastern massive harzburgite unit of

Walcott (1969) lithologic divisions	Sano and Kimura (2007) lithologic divisions	Webber et al. (2008) structural domains	Stewart et al. (2014) lithologic divisions
Basal Zone (protoclastic)	Harzburgite zone	not in study area	Two Tarns Harzburgite
Upper zone	not in study area	Central Domain	Plateau complex
Upper zone	Moho transition zone	Western Domain	Ellis Stream complex
Upper zone	Plagioclase-bearing harzburgite	Eastern Domain	Plagioclase zone

Table 1 - Correlation chart. Correlation of nomenclature used in different studies of the Red Hills ultramafic massif.

Walcott (1969), and is characterized by a coarse-grained harzburgite that contains minor amounts of clinopyroxene (~3%). On the outcrop scale, it is characterized by reddish weathering and a rough surface texture caused by weather resistant pyroxene grains (Fig. 3a). Orthopyroxene bands, ranging from 0.5 cm to tens of cm wide, are also present, but they are typically not pervasive throughout the unit. In contrast to the rest of the massif, the two tarns harzburgite is noted for its relative lack of dunite bands.

The two tarns harzburgite occupies the eastern half of the massif, and is bound on the east by Ward's Pass fault and the Patuki mélange (Johnston, 1982; 1990). Outcrops are generally absent within 100 m of the eastern edge of the massif, and the isolated outcrops present are serpentinized. On its western boundary, the two tarns harzburgite either grades into the plagioclase zone or is truncated by the Porter fault (Fig. 2). To the south, the two tarns harzburgite grades into the Plateau complex, with isolated zones of plagioclase lherzolite along the boundary. Our mapping confirms the presence of the

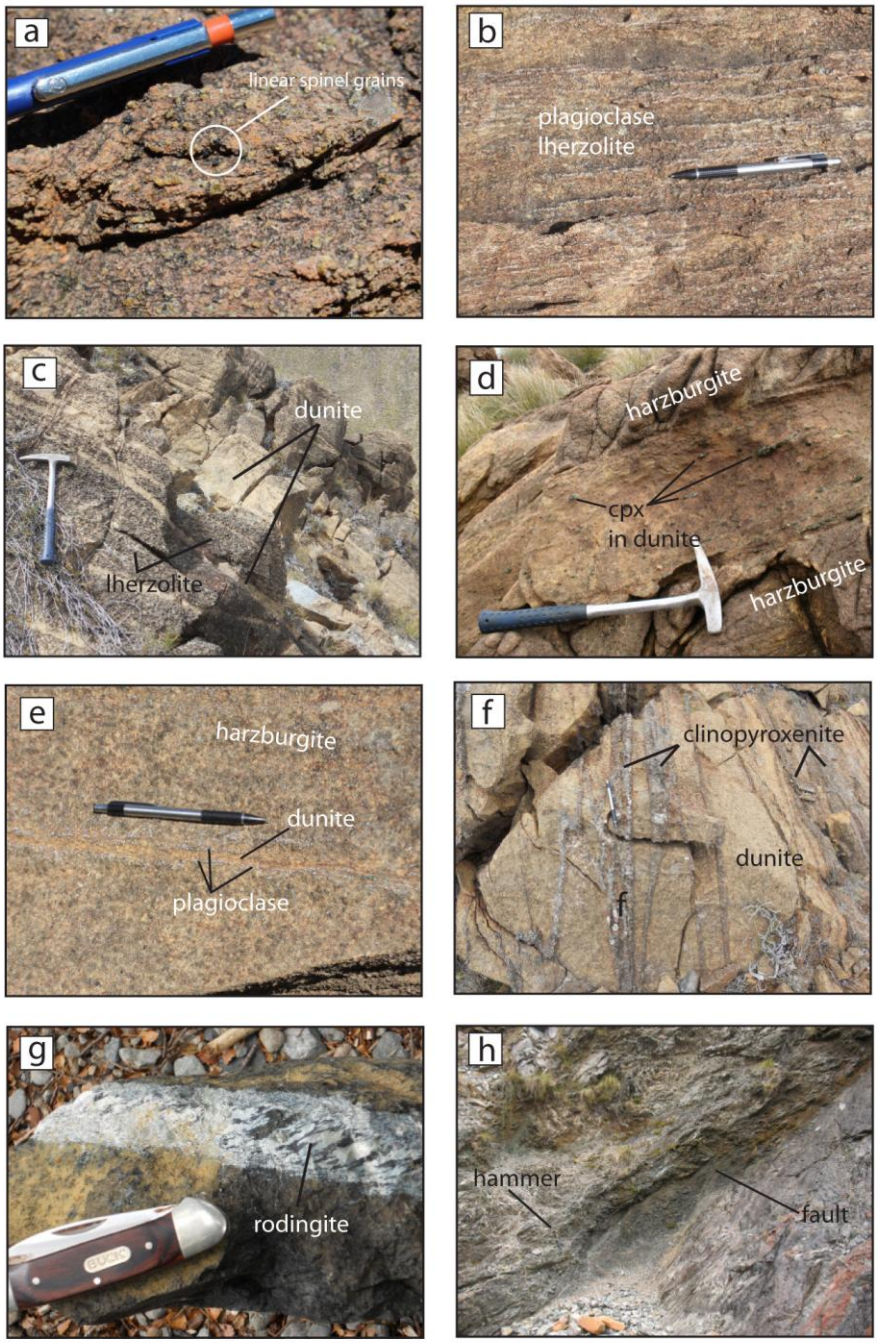

Figure 3 - Outcrop photos. a.) two tarns harzburgite showing subtle lineation in spinel; b.) Plagioclase foliation in the Plagioclase zone; c.) Banded, coarse-grained lherzolite and dunite of the Plateau complex; d.) Interstitial clinopyroxene within a dunite band, Plateau complex; e.) Plagioclase within and along the margins of a thin dunite band, Plateau complex; f.) Folded and planar pyroxenite bands in dunite of the Ellis Stream complex; g.) Syn-tectonic plagiogranite dike in the Ellis Stream complex; h.) Porter fault, showing a ~2 meter thick fault core, where is crosses the Right-branch of the Motueka River.

Porter fault, originally mapped by Johnston (1990).

Meso-scale structures

The two tarns harzburgite typically appears massive, although it contains a consistent lineation defined by the orientation of elongate spinel minerals and less commonly aligned pyroxene (Fig. 3a, 4a, 4b). Spinel lineations are subtle in outcrop (Fig. 3a), but are consistently oriented and pervasive. The lineation typically plunges ~20° toward the ENE (Fig. 4b). In contrast, foliations are much more poorly developed compared to lineations, and in some outcrops no foliation could be observed. On the scale of the complex, poles to foliation display a rough girdle distribution (Fig. 4a).

Plagioclase zone

Unit description

The plagioclase zone is defined as map areas containing abundant plagioclase, either in the form of plagioclase-lherzolite or plagioclase-harzburgite (Fig. 2). Clinopyroxenite bands, websterite bands, and rare orthopyroxenite bands occur throughout this zone; dunite bands are largely absent. Plagioclase occurs as thin (mm to cm long) stringers (Fig. 3b), and is associated with the development of strong foliations near the contact with the Plateau complex.

The plagioclase zone occurs as pods and sills along the western margin of the two tarns harzburgite and eastern margin of the Plateau complex. In general, the amount of plagioclase-bearing peridotite in the plagioclase zone progressively decreases to the

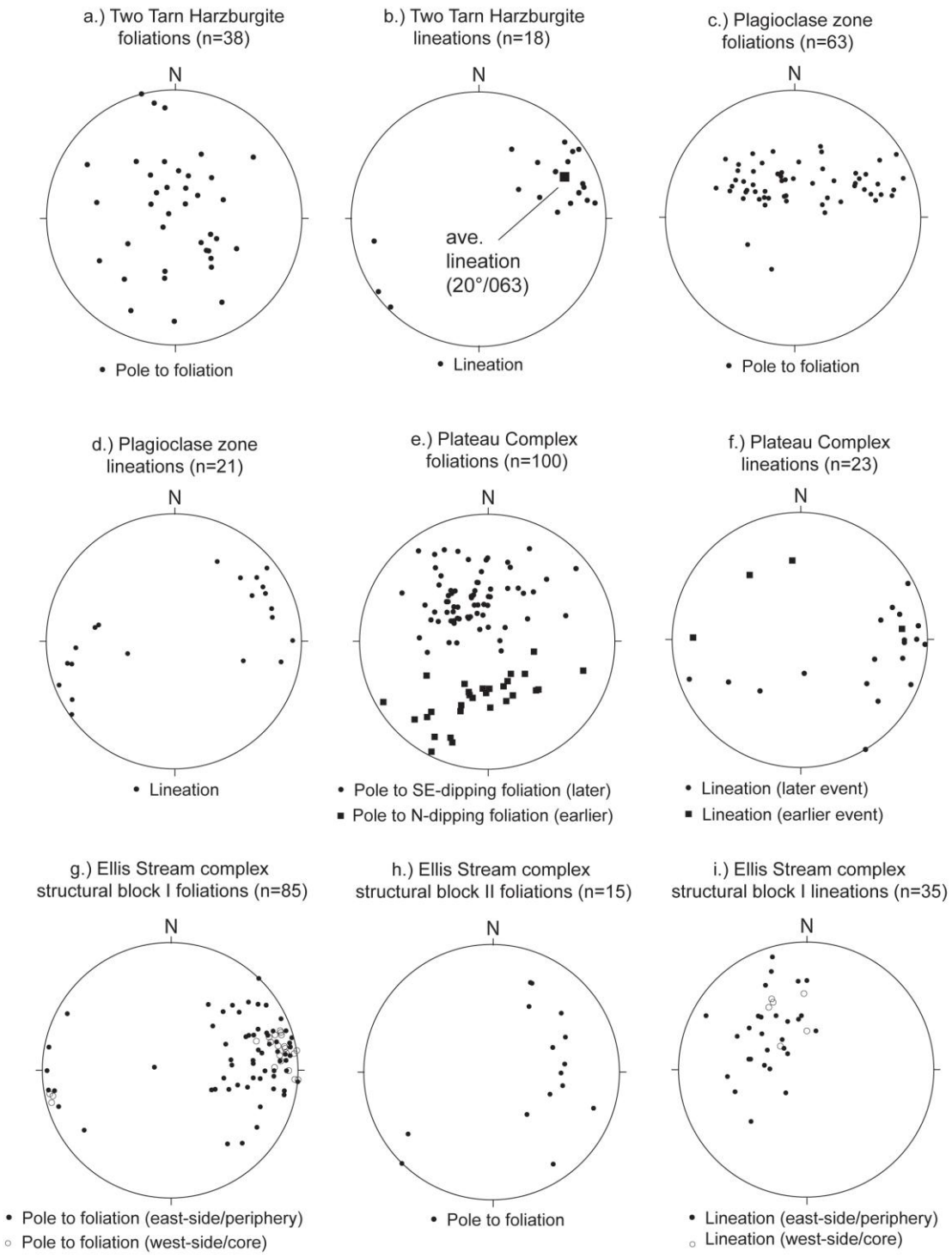

Figure 4 - Equal area stereographic plots. Foliations and lineations are plotted for each ultramafic unit.

east, grading into the two tarns harzburgite. On the west, it abruptly grades into banded peridotites of the Plateau complex. The Porter fault truncates the plagioclase zone on its western margin in the northern massif.

Meso-scale structures

Outcrop foliations are characterized by the strong planar alignment of plagioclase, and sometimes pyroxene and olivine (Fig. 3b). Near the contact with the Plateau complex adjacent to and south of Porter's Knob (Fig. 2), plagioclase foliations are well developed, and plagioclase foliations have a mean orientation of 043/32°SE, very similar to the southeast-dipping compositional banding of the Plateau complex. In the north-central portions of the massif, plagioclase foliations typically dip to the southwest or northwest (Fig. 2). Lineations are defined by elongate spinel, plagioclase, or pyroxene grains, and typically plunge shallowly to the east-northeast or west-southwest (Fig. 4d). Clinopyroxenite bands vary from strongly folded to planar, and likely developed during more than one event. Deformed pyroxenite bands in plagioclase lherzolites from the north-central massif suggest right-lateral shear sense. Elsewhere no shear sense indictors were observed.

Plateau complex

Unit description

The Plateau complex is composed of dominantly spinel-harzburgite with less common spinel-lherzolite, both of which are inter-layered with dunite, pyroxenite, and websterite bands (Fig. 3c, 3d). Dunite bands commonly contain large clinopyroxene

grains within them (Fig. 3d), and locally contain plagioclase (Fig. 3e). Large pods and sills of dunite and olivine-rich lherzolite occur throughout the unit, varying from meters to hundreds of meters wide. Plagioclase-spinel-lherzolites also occur throughout the unit, but are far less common. The rocks that comprise the Plateau complex are largely unserpentinized, with the exception of units exposed along the southwestern extent of the unit.

Near Porter's Knob, in the central part of the massif (fig. 2), the Plateau complex forms a thin, <1 km wide NE-SW trending zone (Central Domain of Webber et al., 2008), but southward the unit widens significantly. The unit is bounded on the southwest by the Cenozoic (?) Maitland's Creek reverse fault, on the northwest by the Porter fault, and to the north and east it grades into either the plagioclase zone or the two tarns harzburgite (Fig. 2).

Meso-scale structures

The Plateau complex contains lherzolite-dunite and more commonly harzburgite-dunite compositional banding dipping both to the north and to the southeast (Figs. 2; 4e). Outcrop observations suggest pyroxene and spinel shape preferred orientations commonly parallel compositional banding. North-dipping foliations have a mean orientation of 285/41°N, and outcrop in a zone along the western boundary of the map unit (Figs. 2; 4e). Southeast-dipping foliations have an average orientation of 060/31°SE, and occur throughout the entire unit. Spinel and pyroxene mineral lineations for the southeast-dipping fabric vary locally, but most commonly plunge shallowly to the east with a mean orientation of 23° at 092 (Fig. 4f). Lineations in the N-dipping fabrics

are not well constrained, but appear to have a wide range in orientations (Fig 4f). In both the N-dipping and SE-dipping foliations, there is considerable local variability in fabric orientation (Fig. 2, Fig. 4e). Cross-cutting relations evident at Porter's Knob indicate the southeast-dipping foliation developed after the north-dipping fabric (Webber et al., 2008). A diffuse, but penetrative, plagioclase foliation occurs locally parallel to the southeast-dipping banded harzburgite-dunite fabric. Southeast-dipping pyroxenite bands sub-parallel to southeast-dipping dunite bands are either planar or boudinaged, while pyroxenites oriented at high angles to the southeast-dipping dunite bands are often strongly folded. Cross-cutting relations indicate at least two generations of pyroxenite bands are present in the Plateau complex, and the earlier generation of bands is often folded and oriented at high angles to the southeast-dipping dunite bands.

Ellis Stream complex

Unit description

The Ellis Stream complex is composed of banded harzburgite and dunite with minor lherzolite and uncommon plagioclase dunite and wehrlite. Dunite pods that are several hundred meters wide are also observed locally. Overall, the unit contains more dunite than the Plateau complex. Pyroxenite and websterite bands, varying from several millimeters to ~1 m in thickness, occur throughout the unit. Serpentine progressively replaces olivine towards the western margin of the unit, and eventually the unit grades into a serpentinized mélange. The Ellis Stream complex also contains tabular rodingite

bands, which occur primarily on the western edge of the complex and decrease in abundance toward the east. Some rodingites are surrounded by halos of serpentinite.

The Ellis Stream complex comprises the majority of the exposed ultramafic rocks in the western portion of the Red Hills ultramafic massif (Fig. 2). The unit is bounded on its eastern side by the Porter fault (Fig. 2), on the northwest by a bounding serpentine mélange, and on the southwest by the Cenozoic (?) Maitland's Creek reverse fault. The Ellis Stream complex is truncated on the north by the Red Hills fault. Few outcrops are exposed within one kilometer of the northwestern margin due to intense serpentinization and weathering.

Meso-scale structures

I divide the Ellis Stream complex into two structural blocks, separated by a serpentinized fault (labeled blocks I and II on Fig. 2). Block I typically contains a west-dipping foliation (Fig. 4g) defined by sub-parallel dunite bands, and a planar alignment of pyroxene and spinel mineral grains. Bulk foliation orientations change across block I, changing from N-striking, moderate-to-steeply west-dipping at the eastern side of the unit to N striking, sub-vertical in the western part of the unit (Fig. 4g). Considerable variability occurs locally in foliation orientation, especially in the vicinity of the Porter fault (Fig. 2, Plate 1). Block II is characterized by a greater variability in foliation orientations (Fig. 4h), and has no systematic trends (see also Plate 1). Lineation is defined by elongate spinel and/or pyroxene grains. Within the Ellis Stream complex, lineation is variable in orientation, but generally plunges steeply to the NW in block I (Fig. 4i).

Pyroxenite and websterite bands cross-cut the dunite bands, and are folded or boudinaged in both structural blocks in the Ellis Stream complex. Folding and boudinage is particularly prevalent in structural block I. Folds are characterized by a range of inter-limb angles, ranging from gentle to isoclinal and intrafolial (Fig. 3f). Unlike pyroxenite bands, dunite bands are typically planar. Some rodingite bands cross-cut the steeply west-dipping foliation, while others are deformed (Fig. 3g). Asymmetric pyroxene porphyroclasts consistently show east-side up motion, when viewed on surfaces perpendicular to foliation and parallel to lineation.

Porter fault

The Porter fault is a particularly important late-stage structure that truncates and displaces the lithologic map units described previously. This fault is oriented approximately N20E/70NW, and is characterized by an ~2 m wide fault core of well-foliated and heavily serpentinized fabric (Fig. 3h). Locally, it contains zones of abundant breccia. Parts of the fault have been intruded by basaltic dikes, some of which have been ductilely deformed by the fault. Fault zone lineations pitch very shallowly to the southwest, and are characterized by elongate plagioclase in deformed basaltic dikes, elongate quartz in deformed plagiogranite dikes, and elongate serpentine. Shear sense indicators, defined by asymmetric tails in minerals from deformed dikes, indicate dominantly left-lateral, strike-slip motion. A series of later serpentinized faults cross-cut the Porter fault (Fig. 2), but they are not thought to play a role in the exhumation of the ultramafic body.

MICROSTRUCTURES

Two tarns harzburgite

In thin section, harzburgites contain a seriate, interlobate texture (Fig. 5a). Coarser olivine and orthopyroxene, and less commonly clinopyroxene grains are typically 1 to 5 mm in length, but range in size up to 1 cm (Fig. 5a). These larger grains generally exhibit no obvious shape preferred alignment in outcrops. Finer grains of olivine, clinopyroxene, orthopyroxene, and spinel show a continuous range in diameters down to several microns (Fig. 5b). Coarse orthopyroxene grains are surrounded by finer-grained olivine, orthopyroxene, and spinel (Fig. 5b). In contrast, coarse clinopyroxene grains are surrounded by finer-grained olivine, clinopyroxene, and spinel (Fig. 5b). Samples with less than 2% clinopyroxene contain volumetrically less fine-grained material than samples with more clinopyroxene. Where large olivine grains are surrounded by finer-grained matrix, the matrix is typically composed of olivine and orthopyroxene. Small grains often embay into larger grains, forming serrated grain boundaries (Figs. 5a, 5b). 120° triple junctions are generally uncommon in olivine, and large olivine grains typically contain abundant subgrains. Orthopyroxene and clinopyroxene grains larger than a millimeter commonly contain exsolution lamellae concentrated in grain cores, and some show evidence of kinking.

Plagioclase zone

Microstructures in the plagioclase zone vary across the unit, and may correlate to lithology. Plagioclase harzburgites contain an inequigranular to seriate, interlobate

texture. In these samples, coarse grains of olivine and orthopyroxene can exceed 1 cm in diameter, and finer grains of olivine, orthopyroxene, clinopyroxene, plagioclase and spinel can have diameters as small as 20 microns (Fig. 5c). Plagioclase lherzolites, however, contain less variation in grains sizes, and typically have olivine, orthopyroxene, clinopyroxene, and plagioclase grains with diameters ranging between 0.4 mm and 1.4 mm (Fig. 5d). Uncommonly, olivine grains from the plagioclase zone are partially surrounded by very thin (<100 micron thick) mantles of orthopyroxene (Fig. 5e). The orthopyroxene mantles are thickest at triple junctions and taper along grain boundaries (Fig. 5e). The abundance of 120° olivine triple junctions varies from approximately 40% of olivine grains to <5% across the plagioclase zone, with no obvious spatial or lithologic pattern. Olivine grain boundaries vary from straight to serrated, and have a strong to moderately weak shape preferred orientation parallel to the lineation direction. Subgrains are common in olivine grains. Orthopyroxene and clinopyroxene grains larger than several millimeters commonly contain exsolution lamellae concentrated in grain cores. Plagioclase is often lenticular shaped, and typically has curved grain boundaries.

Plateau complex

A bimodal olivine grain size population is common in spinel-lherzolites, spinel-harzburgites and plagioclase-spinel-lherzolites from the Plateau complex. Coarser olivine grains vary from several millimeters to coarser than 1 centimeter, and contain numerous subgrains. Finer olivine grains typically vary from just under a millimeter to

Figure 5 - Cross-polarized optical images (a, c-j) and backscatter electron image (b). a.) Harzburgite from the two tarns harzburgite, showing large grains of olivine and orthopyroxene mantled by very fine-grained olivine, orthopyroxene and spinel. b.) Backscatter electron image of large orthopyroxene and clinopyroxene grains mantled by olivine, spinel and likely residual ortho- and clinopyroxene, respectively. Spinel is white, clinopyroxene is light grey. Small orthopyroxene grain boundaries have been traced for clarity. c.) Plagioclase, olivine, and orthopyroxene forming a fine-grained network surrounding larger grains of olivine and orthopyroxene, from 11ES25, plagioclase zone. d.) Olivine, orthopyroxene, and less common clinopyroxene containing abundant interlobate grain boundaries, from a plagioclase-bearing lherzolite, plagioclase zone. Grain size variation is less than in 5c. e.) Orthopyroxene occurring along an olivine triple junction, from RH12_23, northern plagioclase zone. f.) Orthopyroxene wedging into olivine containing subgrains, indicating the orthopyroxene formed after crystal plastic deformation of olivine. From 12RHES13, southern Plateau complex g.) Orthopyroxene embaying into olivine containing subgrains. Orthopyroxene forms a halo around the olivine, from 12RHES13, southern Plateau complex. h.) Lherzolite from the Plateau complex (12RH14a) containing a mix of polygonal olivine grains, often joining in 120° triple junctions (arrow), and interlobate clinopyroxene and orthopyroxene grains boundaries. i.) Dunite with smaller olivine forming a network of grains surrounding larger olivine, from central Ellis Stream complex. j.) Heavily serpentinized coarse-grained dunite from the Ellis Stream complex, showing a large elongate orthopyroxene grain.

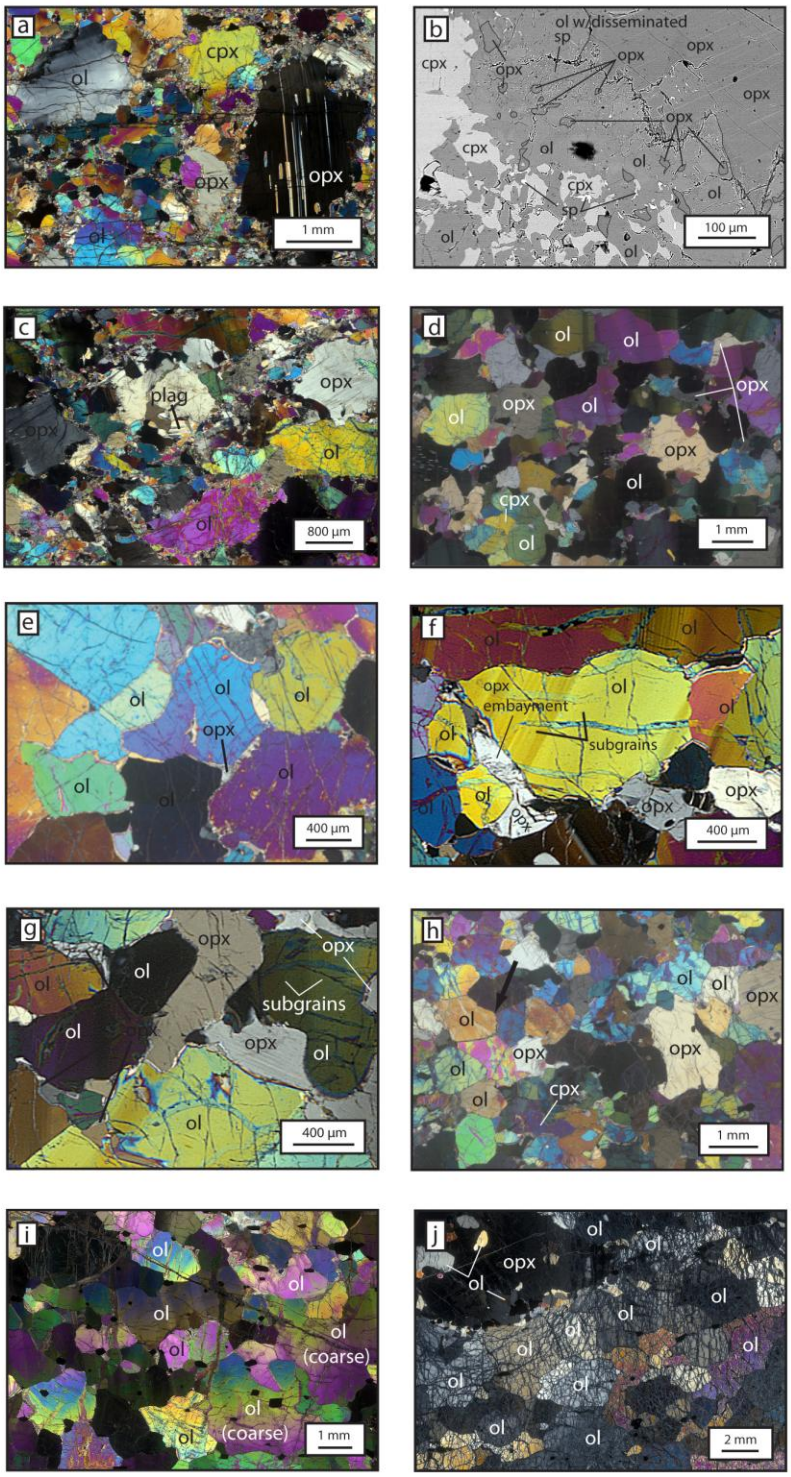
a
cpx
ol
opx
opx
ol
1 mm
b
ol w/disseminated
sp
opx
opx
cpx
opx
opx
cpx
ol
ol
cpx
sp
ol
ol
ol
100 µm
c
plag
opx
opx
ol
ol
800 µm
d
ol
ol
opx
ol
opx
ol
opx
ol
cpx
ol
1 mm
e
ol
ol
ol
opx
ol
ol
ol
400 µm
f
ol
ol
opx
embayment
ol
ol
ol
subgrains
ol
opx
ol
opx
400 µm
g
opx
opx
ol
ol
subgrains
opx
ol
ol
400 µm
h
ol
ol
opx
ol
opx
opx
ol
ol
cpx
1 mm
i
ol
ol
ol
ol
ol
(coarse)
ol
ol
(coarse)
1 mm
j
ol
ol
opx
ol
ol
ol
ol
ol
ol
ol
ol
ol
ol
2 mm

several millimeters. Orthopyroxene grains, however, vary continuously in size from ~1 cm to <1 mm. Clinopyroxene and plagioclase grains typically vary in size from just under a millimeter to several millimeters. Grain boundary morphology in lherzolites and harzburgites varies randomly across the Plateau complex. In some lherzolite samples, orthopyroxene and the finer olivine grains have curved, interlobate grain boundaries, and some orthopyroxene grains taper to form wedges indenting or embaying into olivine grains (Figs. 5f, 5g). Undeformed orthopyroxene often forms rims that partly to entirely surround deformed olivine grains (Fig. 5g). Elsewhere, lherzolites and harzburgites from the Plateau complex contain many grain boundary geometries that are polygonal, and olivine 120° triple junctions are common (Fig. 5h). By comparison, dunites from the Plateau complex are less variable; these typically have olivine grains that vary in size between several millimeters and several centimeters, and often contain a unimodal grain size population. 120° triple junctions are commonly observed between olivine grains in dunite, and subgrains are common. Grain boundaries are typically straight to curvilinear, and can often be classified as polygonal or weakly interlobate.

Ellis Stream complex

Dunites and harzburgites from the Ellis Stream complex contain a bimodal olivine grain size population (Fig. 5i). In dunites, fine olivine grains typically vary in diameter from ~0.6 mm to 1.6 mm (Fig 5i). Finer grains are equant with polygonal grain boundaries and 120° triple junctions common. Coarser olivine grains in dunites are irregularly shaped (Fig. 5i), and are often in excess of 3 mm in diameter. Subgrains are

common in both the coarser and finer olivine grains. Alteration to serpentine is more common than in other units (Fig. 5j), especially in the western portion of the unit. Olivine grains in harzburgites are typically between 0.6 mm and 1.6 mm in diameter, and often have polygonal grain boundary geometries. Orthopyroxene grains in harzburgites vary in diameter from less than 1 mm to coarser than 1 cm, and are often elongate parallel to the spinel lineation (Fig. 5j). Orthopyroxene commonly has a poikilitic texture (Fig. 5j). Larger orthopyroxene grains often contain thin clinopyroxene exsolution lamellae. Plagioclase occurs uncommonly.

GEOTHERMOBAROMETRY

The following section provides quantitative constraints on temperatures and pressures of equilibration for all four map units, which I interpret to reflect the timing relationships between the different units. I assume higher pressures and hotter temperatures formed prior to shallower pressures and cooler temperatures. I expand the work of Webber et al. (2008; 2010), who estimated temperatures in the central RHUM, by considering the entire RHUM and by estimating pressure conditions.

Methods

A Cameca SX50 electron microprobe equipped with four wavelength dispersive spectrometers, located at Texas A&M University, was used to determine the abundances of major and minor elements in minerals from plagioclase-spinel-lherzolites, spinel-lherzolites, and spinel-harzburgites from a suite of samples across the massif. Sample

locations are given on Figure 2, and coordinates are provided in Appendix A. Plagioclase grains were analyzed using a 15 kV accelerating voltage and a 10 nA beam current. Olivine, spinel, orthopyroxene, and clinopyroxene were analyzed using a 15 kV accelerating voltage and a 20 nA beam current. Plagioclase, olivine, and spinel grains were analyzed with a 1 micron diameter beam, while pyroxene grains were analyzed with a 20 micron diameter beam.

Mineral analyses were normalized to cations as follows: Plagioclase to five cations, pyroxenes to four cations, spinel and olivine to three cations. Fe^{3+} versus Fe^{2+} was calculated for pyroxene and spinel based on charge balance, although this method involves significant uncertainty (Canil and O'Neil, 1996). I have more accurately determined the ferric-ferrous ratios in spinels by applying the method of Wood and Virgo (1989) which involves analyzing spinel standards with known $Fe^{3+}/\Sigma Fe$ ratios (provided by B. Wood) during each microprobe session. The value of $Fe^{3+}/\Sigma Fe$ ratio, as originally determined from charge balance, is then adjusted based on the analyses of these spinel standards.

Equilibrium temperatures are based on two-pyroxene thermometry (Taylor, 1998; Brey and Köhler, 1990; Nimis and Taylor, 2000). Various formulations of pyroxene geothermometers are available and my reliance on the Taylor (1998) two-pyroxene geothermometer is based on the work of Nimis and Grütter (2010). Two additional formulations of the pyroxene geothermometer, the enstatite-in-cpx thermometer of Nimis and Taylor (2000), and Ca-in-opx thermometer (Brey & Köhler, 1990), as modified by Nimis and Grütter (2010), yield temperatures that agree well with the

Taylor (1998) thermometer (Nimis & Grütter, 2010). The agreement between the enstatite-in-cpx (Nimis and Taylor, 2000) thermometer and the Taylor (1998) 2-pyroxene thermometer is ±30˚C, while the modified Ca-in-opx thermometer agrees well with the Taylor (1998) thermometer at temperatures above 1000°C, but may deviate from Taylor's 2-pyroxene temperature by as much as +90˚C below 1000°C (Nimis and Grütter, 2010). All three thermometers, as well as the Brey and Köhler (1990) two-pyroxene thermometer, are applied in this study and I use the agreement between these formulations as an indicator of retention of equilibrium pyroxene compositions.

Some relatively large (approximately greater than 500 microns) clinopyroxene and orthopyroxene grains contain exsolution lamellae. Lamellae are generally confined to the cores of the grains, and rims generally lack lamellae. Smaller pyroxene grains lack lamellae altogether. In cases where exsolution lamellae are present, compositions of pyroxenes were determined via re-integration, using an approach similar to that of Lamb (1993) for exsolved feldspars. In these cases, microprobe analyses were performed along a series of traverses to produce a grid of 20 micron diameter spots. Between 71 and 324 spots were analyzed in each pyroxene grain containing lamellae, and the compositions based on the average of these analyses were used to estimate temperatures prior to exsolution. All other grains were analyzed in traverses, and representative analyses were chosen for core and rim compositions.

Re-integrated two-pyroxene temperatures based on the Taylor (1998) geothermometer were combined with the calculated stability of the reaction:

$$spinel + diopside + enstatite = anorthite + 2forsterite$$

$$MgAl_2O_4 + CaMgSi_2O_6 + Mg_2Si_2O_6 = CaAl_2Si_2O_8 + 2Mg_2SiO4 \quad (1)$$

to estimate equilibrium pressures in plagioclase-spinel-lherzolites from the Plateau complex and the plagioclase zone. The pressure-temperature stability of equilibria (1) depends, in part, on the activities of the end-members in the natural phases, as shown by the relation:

$$0 = \Delta G^{\circ}_{P2,T2} = \Delta G^{\circ}_{P1,T1} + \int_{P1}^{P2} \Delta V^{\circ}_{P,T} dP - \int_{T1}^{T2} \Delta S^{\circ}_{P,T} dT + RTln\left(\frac{a_{an}a_{fo}^2}{a_{sp}a_{di}a_{en}}\right) \quad (2)$$

where ΔG° is the Gibbs free energy of the end member phases (standard state), ΔV° is the standard state volume change, P is pressure, ΔS° is the standard state entropy change, T is temperature, and a refers to the activities of each end-member phase. End member activities of all natural phases except spinel were determined using composition data from the microprobe and the software package AX (Powell et al., 1998). However, the software package "MELTS" (Asimow and Ghiorso, 1998) was employed to calculate the spinel end-member (see the discussion in Lamb and Popp, 2009). The P-T location of equilibria was calculated using ThermoCalc (e.g., Powell et al. 1998). The P-T intersection of the Taylor (1998) two-pyroxene temperature with equilibria (1), adjusted for the reduced end-member activities of all phases, is interpreted to be the equilibration pressure for samples analyzed.

Compositions of pyroxene grains were determined using the electron microprobe in an effort to determine temperatures during the highest temperature (and presumably earliest) deformation events recorded by the minerals. Therefore, orthopyroxene and clinopyroxene grains analyzed, from all units, were typically coarse (≥1 mm in diameter), and contained exsolution lamellae in their cores, and hence re-integration of

these pyroxene cores provides a better estimate of pre-exsolution composition. Orthopyroxene grains from all units selected for microprobe analyses typically contain curved grain boundaries that embay into olivine grains. Within the two tarns harzburgite, I also analyzed olivine grains that were typically >3 mm in diameter, as those grains are most similar in microstructures, and, therefore, likely to have recorded similar deformation events as the pyroxenes that were analyzed from the same unit. The grain size distributions of olivine from the Plateau complex and Ellis Stream complex are bimodal, while the olivine in the plagioclase zone shows a more continuous range in grain sizes. Olivine grains chosen for analysis from these units form the outcrop foliations, as defined by shape-preferred orientation of this mineral. These olivine grains are typically 1-2 mm in diameter, part of the smaller population of grain sizes within those samples with bimodal size distributions. These grains often contain curved or lobate grain boundaries with orthopyroxene, and likely developed with orthopyroxene during the same event. Spinel, and, where present, plagioclase, show less variation in grain size and microstructure in all units. I analyzed spinel and plagioclase grains that are typically between 0.35 and 1 mm in diameter.

Pyroxene geothermometry results

Re-integrated pyroxene core compositions are listed in Table 2, and results from 2-pyroxene geothermometry are listed in Table 3. I analyzed multiple clinopyroxene and orthopyroxene grains from several samples to test for intra-sample consistency. Results are generally consistent, and the additional analyses are provided in Appendix A.

Taylor's (1998) two-pyroxene geothermometer yields temperatures ranging from 910 to 990˚C for samples from the Plateau complex, Ellis Stream complex, and plagioclase zone, with 6 of 8 values falling between 950 and 990˚C. The modified Ca-in-opx geothermometer yields temperatures of 920 to 1120˚C for these same samples, with 5 of 8 values falling between 1020 and 1080˚C. The highest Ca-in-opx temperature from the plagioclase zone, Plateau complex, and Ellis Stream complex (1120˚C) comes from a plagioclase harzburgite (Fig. 5c, sample 11ES25), and was sampled near the edge of the plagioclase zone adjacent to the two tarns harzburgite (Fig. 2). The Nimis and Taylor (2000) thermometer yields temperatures of 940 to 1040˚C for all samples from the Plateau complex, Ellis Stream complex, and plagioclase zone. Thus, reintegrated two-pyroxene core temperatures from the Plateau complex, Ellis Stream complex, and plagioclase zone typically have values of approximately 1000°C (Table 3). These results are generally consistent with the results of Webber et al. (2008) for the Plateau complex (Central domain of Webber et al., 2008) and Ellis Stream complex (Western domain of Webber et al., 2008). The difference between temperatures based on the Taylor (1998) and Nimis and Taylor (2000) averages approximately -50 ˚C, and the difference between the Taylor (1998) and modified Ca-in-opx temperature averages approximately -80˚C. These differences suggest some re-equilibration during cooling may have occurred and that the Ca-in-opx thermometer may be most resistant to re-setting. However, all three pyroxene thermometers yield average temperatures that are relatively consistent with one another with an average temperature that ranges from 960 to 1040˚C. Thus, I favor an interpretation where pyroxenes from the Plateau complex, Ellis Stream complex, and

Sample	Plateau complex - 12RH14a						Plateau complex - 12RHES13						Plateau complex - 11ES15					
Phase	opx	cpx	ol	sp core	sp rim	plag	opx	cpx	ol	sp core	sp rim	plag	opx	cpx	ol	sp (core)	sp (rim)	plag
Wt% oxides																		
SiO2	55.45	52.26	40.74	0.00	0.00	45.40	55.21	52.00	40.95	0.00	0.00	44.15	55.70	51.80	40.95	0.01	0.01	44.51
TiO2	0.12	0.27		0.26	0.21		0.04	0.11		0.11	0.06		0.05	0.12		0.09	0.08	
Al2O3	2.67	3.39	0.01	29.81	30.32	35.61	3.22	3.92	0.01	35.72	37.00	36.25	2.46	3.71	0.00	31.94	33.48	36.11
Cr2O3	0.66	1.00		36.39	35.44		0.71	1.09		31.79	29.90		0.58	1.19		34.24	32.04	
V2O3				0.27	0.26					0.18	0.18					0.24	0.29	
Fe2O3																		
FeO	6.44	2.90	10.21	19.71	20.02	0.05	5.98	2.51	9.41	16.93	17.16	0.11	6.19	2.37	9.80	19.51	19.70	0.08
MnO	0.14	0.08	0.15	0.59	0.64		0.12	0.06	0.13	0.51	0.47		0.14	0.06	0.14	0.46	0.49	
MgO	32.84	17.85	48.92	12.97	12.76		33.13	17.88	49.88	14.93	15.25		33.30	17.74	49.60	13.75	13.83	
CaO	1.34	21.77	0.02	0.01	0.00	17.92	1.24	22.02		0.02	0.02	19.01	1.07	22.38	0.02	0.00	0.00	19.04
ZnO																		
NiO	0.08	0.07	0.33	0.16	0.12		0.08	0.06	0.01	0.16	0.10		0.07	0.05	0.40	0.17	0.07	
Na2O	0.02	0.31				1.41	0.01	0.27	0.40			0.67	0.02	0.28	0.00			0.77
						100.3			100.8			100.1						100.5
Total	99.76	99.91	100.38	100.16	99.76	8	99.74	99.91	0	100.36	100.14	9	99.58	99.70	100.91	100.40	99.98	0
Atomic units																		
Si	1.93	1.89	1.00	0.00	0.00	2.09	1.91	1.88	0.99	0.00	0.00	2.04	1.93	1.88	0.99	0.00	0.00	2.05
AlIV	0.07	0.11	0.00	1.05	1.07		0.09	0.12	0.00	1.21	1.25		0.07	0.12		1.11	1.16	
AlVI	0.03	0.04	0.00	0.00	0.00	1.93	0.04	0.05	0.00	0.00	0.00	1.97	0.03	0.04	0.00			1.96
Ti	0.00	0.01	0.00	0.01	0.00		0.00	0.00	0.00	0.00	0.00		0.00	0.00		0.00	0.00	
Cr	0.02	0.03	0.00	0.86	0.84		0.02	0.03	0.00	0.72	0.68		0.02	0.03		0.80	0.74	
V			0.00	0.00	0.00				0.00	0.00	0.00							
FeIII	0.02	0.04	0.00	0.05	0.05		0.02	0.05	0.00	0.03	0.05		0.02	0.06		0.06	0.07	
FeII	0.17	0.04	0.21	0.44	0.45	0.00	0.15	0.02	0.19	0.37	0.36	0.00	0.16	0.01	0.20	0.41	0.41	0.00
Mn	0.00	0.00	0.00	0.02	0.02		0.00	0.00	0.00	0.01	0.01		0.00	0.00	0.00	0.01	0.01	
Ni	0.00	0.00	0.01	0.00	0.00		0.00	0.00	0.01	0.00	0.00		0.00	0.00	0.01	0.00	0.00	
Mg	1.70	0.96	1.78	0.58	0.57		1.71	0.96	1.80	0.64	0.65		1.72	0.96	1.80	0.60	0.60	
Ca	0.05	0.85	0.00	0.00	0.00	0.88	0.05	0.85	0.00	0.00	0.00	0.94	0.04	0.87	0.00	0.00	0.00	0.94
Zn			0.00	0.00	0.00				0.00	0.00	0.00					0.00	0.00	
Na	0.00	0.02	0.00	0.00	0.00	0.11	0.00	0.02	0.00	0.00	0.00	0.05	0.00	0.02		0.00	0.00	0.06
Total	4.00	4.00	3.00	3.00	3.00	5.00	4.00	4.00	3.00	3.00	3.00	5.00	4.00	4.00	3.00	3.00	3.00	5.00
Activity	0.72	0.73	0.8	0.41	0.45	0.88	0.73	0.74	0.82	0.45	0.48	0.94	0.74	0.77	0.81	0.44	0.49	0.93

Table 2 – Mineral compositions

Sample	Plateau complex - 10ES05					Plagioclase zone - RH09_39						Plagioclase zone - 11ES25					
Phase	opx	cpx	ol	sp core	sp rim	opx	cpx	ol	sp core	sp rim	plag	opx	cpx	ol	sp core	sp rim	plag
Wt% oxides																	
SiO2	56.42	53.45	41.36	0.00	0.00	55.50	52.01	40.86	0.00	0.00	44.41	54.81	51.78	41.02	0.12	0.02	43.43
TiO2	0.02	0.05		0.05	0.06	0.04	0.08		0.04	0.02		0.06	0.14		0.12	0.12	
Al2O3	2.30	2.67	0.00	27.78	28.38	2.86	3.89	0.04	40.43	42.04	36.40	3.06	3.45	0.00	34.66	33.99	36.38
Cr2O3	0.64	0.97		39.64	39.31	0.52	1.12		26.99	23.81		0.76	1.04		33.04	33.18	
V2O3				0.18	0.21				0.19	0.19					0.26	0.26	
Fe2O3																	
FeO	5.79	2.49	8.87	19.01	18.60	6.44	2.78	10.55	16.50	18.25	0.08	5.94	2.41	9.26	16.62	17.87	0.06
MnO	0.14	0.09	0.13	0.19	0.21	0.14	0.08	0.15	0.36	0.35		0.14	0.09	0.14	0.36	0.43	
MgO	33.44	18.22	49.78	13.33	13.36	33.52	17.90	49.46	16.19	15.38		32.59	17.53	49.55	15.14	14.38	
CaO	1.37	22.57	0.02	0.01	0.01	0.78	22.14	0.02	0.00		19.50	1.53	23.01	0.02	0.02	0.01	19.64
ZnO																	
NiO	0.10	0.06	0.42	0.09	0.13	0.08	0.04		0.13	0.20		0.09	0.05		0.13	0.13	
Na2O	0.01	0.30	0.01			0.01	0.23				0.56	0.01	0.15				0.61
Total	100.23	100.87	100.58	100.29	100.27	99.89	100.28	101.08	100.84	100.24	100.95	98.99	99.65	99.98	100.46	100.39	100.13
Atomic units																	
Si	1.94	1.92	1.00	0.00	0.00	1.92	1.88	0.99	0.00	0.00	2.03	1.92	1.88	1.00	0.00	0.00	2.01
AlIV	0.06	0.08		0.98	1.00	0.08	0.12		1.33	1.39		0.08	0.12		1.18	1.16	
AlVI	0.04	0.03	0.00	0.00	0.00	0.04	0.04	0.00	0.00	0.00	1.97	0.04	0.03	0.00	0.00	0.00	1.98
Ti	0.00	0.00		0.00	0.00	0.00	0.00		0.00	0.00		0.00	0.00		0.00	0.00	
Cr	0.02	0.03		0.94	0.93	0.01	0.03		0.60	0.53		0.02	0.03		0.75	0.76	
V				0.00	0.00				0.00	0.00					0.00	0.00	
FeIII	0.00	0.04		0.05	0.04	0.03	0.06		0.04	0.05		0.02	0.06		0.04	0.05	
FeII	0.17	0.03	0.18	0.42	0.43	0.16	0.02	0.21	0.34	0.37	0.00	0.15	0.01	0.19	0.36	0.38	0.00
Mn	0.00	0.00	0.00	0.00	0.01	0.00	0.00	0.00	0.01	0.01		0.00	0.00	0.00	0.01	0.01	
Ni	0.00	0.00	0.01	0.00	0.00	0.00	0.00	0.01	0.00	0.00		0.00	0.00	0.01	0.00	0.00	
Mg	1.72	0.97	1.80	0.60	0.60	1.73	0.96	1.79	0.67	0.64		1.70	0.95	1.80	0.65	0.62	
Ca	0.05	0.87	0.00	0.00	0.00	0.03	0.86	0.00	0.00	0.00	0.96	0.06	0.90	0.00	0.00	0.00	0.97
Zn									0.00	0.00					0.00	0.00	
Na	0.00	0.02	0.00	0.00	0.00	0.00	0.02	0.00	0.00	0.00	0.04	0.00	0.01	0.00	0.00	0.00	0.06
Total	4.00	4.00	3.00	3.00	3.00	4.00	4.00	3.00	3.00	3.00	5.00	4.00	4.00	3.00	3.00	3.00	5.03
Activity						0.74	0.740	0.81	0.49	0.51	0.95	0.72	0.79	0.81	0.4606 44	0.52	0.94

Table 2 (continued) – Mineral compositions

Sample	Plagioclase zone - RH12_23						Ellis Stream complex - 11ES27					Two tarns harzburgite - 11ES19				
Phase	opx	cpx	ol	sp core	sp rim	plag	opx	cpx	ol	sp core	sp rim	opx	cpx	ol	sp core	sp rim
Wt% oxides																
SiO2	55.20	51.92	41.10	0.02	0.03	44.39	55.71	52.26	40.68	0.02	0.00	56.31	52.52	41.07	0.00	0.01
TiO2	0.12	0.27		0.22	0.15		0.03	0.06		0.04	0.04	0.03	0.06		0.08	0.08
Al2O3	2.61	3.49	0.01	30.91	33.95	35.90	2.52	3.13	0.00	31.57	36.18	2.39	2.64	0.00	26.04	27.02
Cr2O3	0.65	1.20		35.38	33.33		0.60	0.99		33.95	28.85	0.79	1.07		41.67	40.6
V2O3				0.25	0.19					0.18	0.26				0.20	0.22
Fe2O3																
FeO	6.05	2.45	9.21	19.23	17.56	0.11	7.09	3.12	11.06	21.54	21.74	5.63	2.24	9.06	18.68	18.81
MnO	0.15	0.10	0.13	0.46	0.43		0.17	0.11	0.17	0.53	0.43	0.14		0.13	0.22	0.27
MgO	33.31	18.16	49.78	13.73	14.75		32.93	18.08	48.30	12.46	13.23	32.84	17.64	49.81	13.36	13.34
CaO	1.04	22.29	0.01	0.01	0.00	19.30	1.17	22.29	0.03	0.00	0.00	2.18	23.17	0.03	0.00	0.00
ZnO																
NiO	0.09	0.05	0.40	0.15	0.23		0.08	0.05	0.34	0.10	0.12	0.10		0.39	0.10	0.11
Na2O	0.01	0.16	0.00			0.74	0.01	0.17	0.00			0.02	0.22	0.00		
Total	99.23	100.09	100.65	100.34	100.62	100.4 4	100.31	100.24	100.58	100.38	100.85	100.4 2	99.56	100.48	100.36	100.47
Atomic units																
Si	1.92	1.88	1.00	0.00	0.00	2.04	1.93	1.89	1.00	0.00	0.00	1.94	1.91	1.00	0.00	0.00
AlIV	0.08	0.12		1.08	1.16		0.07	0.11		1.10	1.23	0.06	0.09		0.93	0.96
AlVI	0.03	0.03	0.00	0.00	0.00	1.95	0.03	0.02	0.00	0.00	0.00	0.04	0.02	0.00	0.00	0.00
Ti	0.00	0.01		0.00	0.00		0.00	0.00		0.00	0.00	0.00	0.00		0.00	0.00
Cr	0.02	0.03		0.83	0.76		0.02	0.03		0.80	0.66	0.02	0.03		0.99	0.96
V				0.00	0.00					0.00	0.00				0.00	0.00
FeIII	0.03	0.06		0.07	0.06		0.03	0.07		0.08	0.09	0.00	0.05		0.05	0.05
FeII	0.15	0.02	0.19	0.40	0.37	0.00	0.18	0.02	0.23	0.46	0.44	0.16	0.02	0.18	0.42	0.42
Mn	0.00	0.00	0.00	0.01	0.01		0.00	0.00	0.00	0.01	0.01	0.00		0.00	0.01	0.01
Ni	0.00	0.00	0.01	0.00	0.01		0.00	0.00	0.01	0.00	0.00	0.00		0.01	0.00	0.00
Mg	1.73	0.98	1.80	0.60	0.64		1.70	0.97	1.76	0.55	0.57	1.69	0.96	1.81	0.60	0.60
Ca	0.04	0.86	0.00	0.00	0.00	0.95	0.04	0.86	0.00	0.00	0.00	0.08	0.90	0.00	0.00	0.00
Zn				0.00	0.00					0.00	0.00					
Na	0.00	0.01	0.00	0.00	0.00	0.07	0.00	0.01	0.00	0.00	0.00	0.00	0.02	0.00	0.00	0.00
Total	4.00	4.00	3.00	3.00	3.00	5.01	4.00	4.00	3.00	3.00	3.00	4.00	4.00	3.00	3.00	3.00
Activity	0.74	0.76	0.82	0.42	0.43	0.93										

Table 2 (continued) – Mineral compositions

Sample	Two tarns harzburgite - RH12ES14				
Phase	opx	cpx	ol	sp core	sp rim
Wt% oxides					
SiO2	55.14	52.17	41.28	0.01	0.01
TiO2	0.03	0.07		0.03	0.02
Al2O3	4.09	3.81	0.00	41.94	45.34
Cr2O3	0.84	0.92		26.89	23.58
V2O3				0.14	0.16
Fe2O3					
FeO	5.76	2.28	9.18	14.37	13.41
MnO	0.14		0.13	0.14	0.10
MgO	32.16	17.31	49.47	17.13	17.78
CaO	1.83	23.38	0.03	0.01	0.01
ZnO					
NiO	0.10		0.41	0.21	0.21
Na2O	0.01	0.06	0.01		
Total	100.10	100.00	100.53	100.87	100.62
Atomic units					
Si	1.91	1.89	1.01	0.00	0.00
AlIV	0.09	0.11		1.37	1.46
AlVI	0.07	0.05	0.00	0.00	0.00
Ti	0.00	0.00		0.00	0.00
Cr	0.02	0.03		0.59	0.51
V				0.00	0.00
FeIII	-0.01	0.03		0.02	0.01
FeII	0.17	0.04	0.19	0.31	0.29
Mn	0.00		0.00	0.00	0.00
Ni	0.00		0.01	0.00	0.00
Mg	1.66	0.94	1.80	0.71	0.72
Ca	0.07	0.91	0.00	0.00	0.00
Zn					
Na	0.00	0.00	0.00	0.00	0.00
Total	4.00	4.00	3.00	3.00	3.00
Activity					

Table 2 (continued) – Mineral compositions

plagioclase zone equilibrated at a temperature of approximately 1000˚C. It is possible sample 11ES25 (Fig. 5c), which has an elevated Ca-in-opx temperature of 1120˚C and was sampled near the edge of the plagioclase zone (Fig. 2), may contain orthopyroxene grains that record a higher temperature event associated with the two tarns harzburgite that did not re-equilibrate at approximately 1000˚C.

Samples from the two tarns harzburgite show more pronounced differences between two-pyroxene and enstatite-in-cpx temperatures compared to single pyroxene Ca-in-opx temperatures (Table 3). Ca-in-opx temperatures are around 1200°C, while Taylor (1998) and Nimis and Taylor (2000) temperatures are around 900°C. This large difference indicates clinopyroxene and orthopyroxene are not currently in equilibrium.

Sample	Lithology	Map Unit	2-px (Brey and Kohler, 1990)	Ca in Opx (Nimis and Grutter, 2010)	2-px (Taylor, 1998)	Enstatite in cpx (Nimis and Taylor, 2000)	Equilibration Pressure (kbar)
11ES15	Plagioclase lherzolite	Plateau complex	980	1020	940	1000	5.4
12RH14a	Plagioclase lherzolite	Plateau complex	1030	1080	990	1040	5.1
RH12ES13	Plagioclase harzburgite	Plateau complex	1030	1050	980	1040	4.8
10ES05	Harzburgite	Plateau complex	990	1080	950	1000	-
RH09_39	Plagioclase lherzolite	Plagioclase zone	1020	920	970	1040	5.3
11ES25	Plagioclase harzburgite	Plagioclase zone	940	1120	910	940	5.1
RH12_23	Plagioclase lherzolite	Plagioclase zone	1020	1000	970	1030	4.4
11ES27	Lherzolite	Ellis Stream complex	1010	1040	980	1040	-
11ES19	Harzburgite	Two tarns harzburgite	910	1240	890	900	> 4 kbar
RH12ES14	Harzburgite	Two tarns harzburgite	920	1190	910	920	> 6 kbar

Table 3 – Geothermobarometry results. Temperatures are in degrees Celsius.

Parts of the interior of at least one large clinopyroxene grain in sample RH12ES14 has been altered to amphibole. This microstructural observation suggests that clinopyroxene composition, in at least one case, was not a closed system at sub-solidus conditions. I interpret the lower Taylor (1998) and Nimis and Taylor (2000) temperatures compared to the higher Ca-in-opx temperatures from samples of the two tarns harzburgite to reflect general re-setting of clinopyroxene during cooling. The higher, 1200°C Ca-in-opx temperatures are likely a better estimate of temperature during formation of the two tarns harzburgite. These temperatures were obtained by analyzing large pyroxene grains.

Geobarometry results

Representative mineral composition data for plagioclase, spinel, olivine, orthopyroxene and clinopyroxene are listed in Table 2. Spinel grains throughout the massif have a significant amount of chromium with chromium numbers (Cr# = Cr/(Cr+Al)) between 0.28 and 0.60. Most spinel grains from across the massif (with the exception of many grains from the Ellis Stream complex) show Al-Cr zoning. In nearly

all cases, rims are enriched in Al and depleted in Cr. However, nearly all grains exhibiting Al-Cr zoning show no significant zoning of Mg or Fe^{2+}. Olivine grains in all map units are unzoned, and only a single grain of plagioclase (sample RH12_23_1b) is zoned. As described above, large pyroxene grains typically contain exsolution lamellae in their cores, that when re-integrated, have mineral chemistries that reflect higher temperature equilibration than their rims.

The choice of whether to use core or rim mineral compositions for activity calculations varied with each phase. Many pyroxene rims have likely been reset by diffusion. Consequently, I consider that the pyroxene cores best reflect the chemistry of the grains during formation of the units and I estimate the pyroxene activities using their re-integrated core compositions. Spinel compositions are more complex; I estimate spinel activities using spinel rim compositions. I suggest that the aluminum-enriched rims found in many of the spinel grains are related to reactions between melt and pre-existing minerals. This interpretation is based, in part, on the argument that the solid state breakdown of spinel to plagioclase would extract aluminum from the spinel and result in chromium-rich rims, and not the Al-rich rims present in our samples.

The activities of mineral end-members, listed in Table 2, were used to determine the pressure-temperature stability of reaction 1 (Fig. 6). Equilibrium pressures in excess of 9 kbar are predicted for pure end-member reaction (1). However, given the compositions of natural phases in samples from the Red Hills, the stability of equilibria 1 must lie at lower pressures. The intersection of the Taylor (1998) two-pyroxene temperature with each sample's respective equilibrium line marks the estimated

equilibrium pressure, also plotted on Figure 6. Results are also listed in Table 3. All samples equilibrated at pressures between 4.4 and 5.4 kbar at temperatures between 900°C and 1000°C.

The uncertainty in maximum deformation temperature, illustrated by moderately higher Ca-in-orthopyroxene temperatures compared to Taylor (1998) temperatures, in most of our samples indicates our calculated pressures listed in Table 3 are low estimates. The slope of the equilibria lines calculated from Red Hills samples in Figure 6 gives an idea of the temperature dependence of our estimated equilibria pressures. An increase of 65°C leads to an increase in pressure of approximately 0.35 kbar. Additionally, the Taylor (1998) two-pyroxene thermometer has a reported uncertainty of ±31°C. This value corresponds to a pressure uncertainty of between 0.19 and 0.25 kbar (19-25 MPa).

Qualitative constraints on the equilibration pressure of the two tarns harzburgite can also be made. The fine-grained matrix in the two tarns harzburgite includes spinel but not plagioclase. As a result, it is likely the development of the fine-grained matrix occurred at pressures exceeding the stability of plagioclase. Using spinel, orthopyroxene, clinopyroxene, and olivine compositions from the two tarns harzburgite to calculate activities - and assuming an activity of 1 for anorthite - I can estimate a minimum P at which the spinel in the two tarns harzburgite would begin to break down. This estimate yields a pressure of 4 kbar for 11ES19 and 6 kbar for 12RHES14. Since spinel has not begun to break down in either sample, P must be larger than those estimated for both samples. Therefore, I conclude that the two tarns harzburgite equilibrated at pressures in

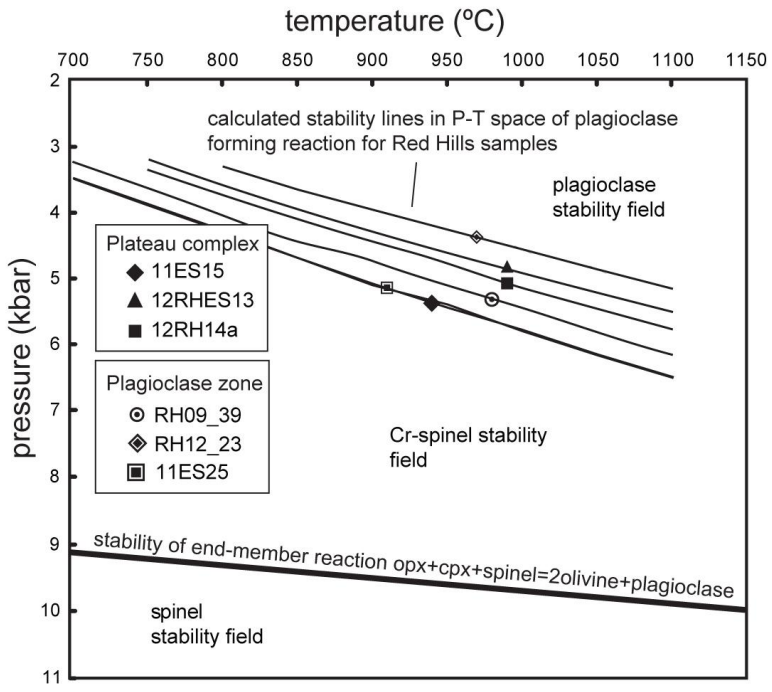

Figure 6 – Constructed equilibria lines in pressure temperature space. The intersection of each equilibria line with the respective Taylor two-pyroxene temperature for each sample is the interpreted equilibrium pressure. For comparison, the equilibria line for the end-member spinel to plagioclase reaction lies at significantly higher pressures than those calculated for the Red Hills.

excess of 6 kbar. This interpretation is consistent with the higher pressure, garnet to spinel stability field melting history reported by Sano and Kimura (2007).

To summarize, the Plateau complex and plagioclase zone equilibrated at pressures of between 4.4 and 5.4 kbar, and temperatures of around 1000°C. It is important to note that within the Plateau complex, pressure-temperature conditions were only calculated on southeast-dipping fabrics. The earlier, north-dipping fabric in the Plateau complex is less well understood due to the likelihood of compositional resetting from the later southeast-dipping event, so its pressure-temperature conditions are unknown. The Ellis Stream complex also records temperatures of approximately

1000°C. The two tarns harzburgite equilibrated at pressures in excess of 6 kbar, consistent with the lack of plagioclase, and a temperature of approximately 1200°C.

DISCUSSION

Evidence for melt migration and melt-involved deformation

In this section I describe the evidence for melt and melt-involved deformation in the two tarns harzburgite, Plateau complex, and plagioclase zone. Evidence for melt reaction or melt refertilization in the units includes: 1) Melt microstructures in the two tarns harzburgite; 2) Dunite bands containing interstitial clinopyroxene and/or plagioclase in the Plateau complex; and 3) Plagioclase in the plagioclase zone and Plateau and Ellis Stream complexes. The goal of this section is to relate the timing of structural fabric development (mineral shape preferred orientations, lineations) to the development of melt-related microstructures and melt-related outcrop observations. I assume that if substantial sub-solidus deformation occurred, melt microstructures would be obliterated. Thus, if mineral lineation and foliation are defined by mineral grains showing melt microstructures, I interpret melt-present deformation in the unit.

Melt microstructures are present in the two tarns harzburgite. Microstructures include large orthopyroxene and clinopyroxene grains that have ragged, partially resorbed edges surrounded by a very fine-grained matrix of olivine, orthopyroxene and spinel (Fig. 5b). The small clinopyroxene grains embedded within olivine in Figure 5b are likely the remnants of incomplete melting and dissolution of the rim of a once larger clinopyroxene grain. Partial dissolution of clinopyroxene during melting is the favored

interpretation to produce the small clinopyroxene grains, in part due to the adjacent larger clinopyroxene grain, and in part due to the elevated geothermometry values calculated for the unit (1200°C), consistent with the presence of melt. Grain mixing from dynamic recrystallization (e.g. Skemer et al., 2010) is possible but not favored due to the spatially restricted zones of small clinopyroxene grains (bottom left of Fig. 5b) and small orthopyroxene grains (central part of Fig. 5b) each embedded in olivine. Small orthopyroxene grains surrounded by olivine and adjacent to larger orthopyroxene grains (Fig. 5b) is a similar microstructure to that reported by Dijkstra et al. (2002) in the Othris ultramafic massif. They interpreted this microstructure resulted from either incomplete incongruent melting of orthopyroxene or from incomplete orthopyroxene dissolution from reaction with a silica undersaturated melt:

$$orthopyroxene + low\ silica\ melt \rightarrow olivine + high\ silica\ melt \quad (3)$$

In either case, the small matrix grains of orthopyroxene surrounded by matrix olivine may reflect portions of orthopyroxene once continuous with the larger orthopyroxene grains. Large olivine grains also have a fine-grained, orthopyroxene bearing matrix surrounding them (Fig. 5a), suggesting olivine may have also become unstable and reacted according to the reverse of reaction (3):

$$olivine + high\ silica\ melt \rightarrow orthopyroxene + low\ silica\ melt \quad (4)$$

Thus I suggest the two tarns harzburgite shows evidence for various melt-related microstructures. I suggest that the consistent lineation found in the unit developed synchronously with the development of the melt microstructures, because sub-solidus deformation would likely have removed the microstructural evidence for reactions (3)

and (4) in the unit. The 1200°C temperatures obtained from large pyroxene grains in this unit likely reflect pyroxene equilibration with melt during melting. It is also noteworthy that the two tarns harzburgite lacks dunite bands, which are typically interpreted to reflect focused melt migration within channels (e.g. Kelemen et al., 1995). Thus, melt may have been relatively homogeneously distributed within the unit, which may explain the homogeneous structural fabric (lineation).

Dunite bands in the Plateau complex also provide evidence for melt migration. Dunite bands are typically thought to represent zones of focused, channelized melt saturated in olivine but undersaturated in pyroxene (Kelemen et al., 1995). Throughout much of the Plateau complex, there is an olivine mineral shape preferred orientation (SPO) in harzburgites parallel to dunite banding, suggesting a relationship between dunite band formation and deformation. Additionally, pyroxenite bands that are oriented sub-parallel to the southeast-dipping dunite bands in the Plateau complex are either planar our boudinaged. In contrast, pyroxenite bands at moderate to high angles to the dunite bands are typically folded. This geometry indicates the bulk orientation of southeast-dipping dunite bands in the Plateau complex is oriented close to the plane containing the maximum and intermediate finite stretch directions (e.g. Tikoff et al., 2010), suggesting a link between dunite bands and deformation. Significant sub-solidus deformation appears unlikely, as most harzburgites in the Plateau complex preserve evidence of melt-related microstructures. For example, orthopyroxene growth with concomitant olivine dissolution is observed (Fig. 5f, 5g), typical of melt-rock reaction (4). Additionally, geothermometry temperatures of approximately 1000°C for rocks in

this unit are consistent with the solidus temperature of basaltic melts at low pressure containing dissolved volatiles (Kushiro et al., 1968; Green, 1972; Mysen, 1973). Significant sub-solidus deformation would be expected to reset geothermometry temperatures to lower values.

Finally, plagioclase infiltration and crystallization is the dominant feature of the plagioclase zone (Fig. 3b), but also occurs locally in the Ellis Stream and Plateau complexes (Fig. 3e). In agreement with Sano and Kimura (2007), I interpret the lenticular-shaped plagioclase grains to reflect fractional crystallization of plagioclase from a percolating and possibly stagnating melt (e.g., Rampone et al., 1997). Olivine grains are typically elongate parallel to the plagioclase foliation. Since melt alignment in peridotites is related to the dynamic conditions in the mantle during melt migration (Daines and Kohlstedt, 1997; Zimmerman et al., 1999; Holtzman et al, 2003), the similarly oriented olivine SPO and plagioclase foliation suggest a link between deformation (olivine SPO) and melt migration (crystallized plagioclase).

To summarize, deformational fabrics measured in the field appear to be related to microstructural or field observations of melt migration in the two tarns harzburgite, Plateau complex, and plagioclase zone. In those three units, I interpret the bulk of deformation to have been more or less synchronous with melt migration. The Ellis Stream complex was not addressed in this section, as it likely contains substantial sub-solidus deformation. It is addressed later in the text.

Relative timing of dunite band formation and plagioclase refertilization

I suggest the timing of dunite band formation and associated deformation in the Plateau complex likely occurred during the same melt migration event as plagioclase and/or clinopyroxene refertilization in the adjacent plagioclase zone and locally within the Plateau complex. Southeast-dipping dunite bands in the Plateau complex commonly contain interstitial clinopyroxene (Fig. 3d), and locally contain plagioclase (Fig. 3e). Dunite bands containing interstitial clinopyroxene and plagioclase likely contain a two-phase melt migration history. This history likely begins with pyroxene undersaturated conditions (forming dunite). Late-stage melts were likely saturated in clinopyroxene and/or plagioclase, perhaps due to continued melt migration under progressively cooler conditions or changing melt compositions. This relation effectively establishes the timing of refertilization to immediately after dunite band creation. Because many of the melt channels in the Plateau complex record refertilization histories, I suggest the southeast-dipping dunite bands of the Plateau complex developed during the same melt migration event as plagioclase and/or clinopyroxene refertilization in the adjacent plagioclase zone. Similar geothermobarometry estimates support this conclusion. Additionally, bulk dunite band orientations south of Porter's Knob (Fig. 2) in the Plateau complex closely parallel adjacent plagioclase foliations in the plagioclase zone, indicating similar dynamic conditions for both. The development of the foliated plagioclase lherzolite (plagioclase zone) concurrently with melt migration in the adjacent unit, banded dunites and harzburgites of the Plateau complex, suggests that melt distribution changed from a diffuse, percolating melt (plagioclase zone) to channelized

melts (dunite bands in the Plateau complex) at the contact. It is also possible, however, that dunite bands in the Plateau complex have been structurally overprinted by the plagioclase zone (Webber et al., 2008; 2010), and thus that the plagioclase zone came later.

A forearc setting for mantle fabrics

I propose that melt-present deformation in the mantle section of the Red Hills took place in a nascent forearc setting at the beginning of a new subduction zone along the Gondwanan margin. Several, regional, petrologic, and field arguments support this model. First, the Red Hills massif is part of the 285-269 Ma Early to Middle Permian DMOB (Kimbrough et al., 1992; Sivell and McCulloch, 2000; Jugum, 2009), which is overlain by Late Permian (260-251 Ma) forearc sediments of the Maitai Group (Coombs et al., 1976; Johnston, 1981; Jugum, 2009). The deposition of forearc sediments immediately after the creation of the ophiolite suggests a genetically related setting for the RHUM. Additionally, arc magmatism resumed along much of the eastern margin of Gondwana in the Late Permian (Caprarelli and Leitch, 1998; Kimbrough et al., 1992), approximately 10-20 million years after the formation of the RHUM. This relatively short delay between arc magmatism and ophiolite creation is consistent with current models for the creation of ophiolites within the forearc of incipient subduction zones (e.g., Shervais, 2000; Stern et al., 2012). Thus, although the RHUM may have occurred in a fore-"arc" setting, it is likely there was no arc present during its formation.

Second, the Plateau complex, plagioclase zone, and the Ellis Stream complex record two-pyroxene geothermometry temperatures of approximately 1000°C, and were affected by a melt refertilization event (Sano and Kimura, 2007). If these geothermometry estimates represent the temperature of the melt, they are too low for an anhydrous mid-ocean ridge melt at 5 kbar, but are permissible for a volatile-rich melt in a subduction zone setting, where the peridotite solidus at 5 kbar is approximately 1000°C (Kushiro et al., 1968; Green, 1972; Mysen, 1973).

Third, plagioclase in the Plateau complex and plagioclase zone is highly calcic (Table 2), varying from An_{89} to An_{96}. Highly calcic plagioclase has been found to be associated with fractional crystallization of hydrous melts (Sisson and Grove, 1993; Koepke et al., 2004; Feig et al., 2006), further suggesting a subduction zone setting.

Finally, rodingite bands both cross-cut and are deformed into the fabric of the Ellis Stream complex (structural block I). These relations indicate deformation must have occurred during emplacement of the bands. These bands contain numerous hydrous phases, which suggest fluids were abundant during deformation in the Ellis Stream complex, which is consistent with a subduction zone setting.

Deformation history during subduction initiation

Using the map patterns, meso-scale structures, geothermometry, and geobarometry, I am able to outline the basic deformational history of the RHUM during the early stages of subduction, and address the role of melt during deformation. I extend the overprinting history of Webber et al. (2008) to the rest of the massif, incorporate the

role of melt during deformation, and break deformation into three stages of deformation based primarily on cross-cutting relations and geothermobarometry. I interpret the three stages of deformation to represent progressive exhumation of the massif within an overall extensional incipient subduction setting. Figures 7 and 8 show the temporal and spatial relationships between map units, deformation, and the development of compositional heterogeneity within each map unit across the three stages of deformation. Below each stage is briefly described.

Stage 1: Linear fabrics in the two tarns harzburgite (1200°C, >6 kbar)

The earliest stage of deformation recorded in the RHUM is the development of highly linear fabric in the two tarns harzburgite (Fig. 7, Fig. 8a). Orthopyroxene bands were also likely emplaced during Stage 1 (Fig. 7). I interpret that the entire massif initially resembled the two tarns harzburgite during Stage 1, but was subsequently overprinted on its western part during Stage 2. This is based on the higher temperature and pressure estimates for the two tarns harzburgite (1200°C, and >6 kbar, respectively), and the lack of overprinting fabrics.

Linear fabrics dominate the entire two tarns harzburgite (Fig. 3a, 4b). Foliations do occur locally, but are weakly developed and not consistent in orientation (Fig. 4a). Such fabric is typical of L-tectonites, which are thought to result from constrictional, three-dimensional finite strain. They cannot result from any homogeneous, two-dimensional plane strain deformation; any plane strain deformation will result in the formation of lineation and foliation (L-S-tectonites) within a ductilely deformed rock.

The development of L-tectonites during Stage 1 provides important constraints

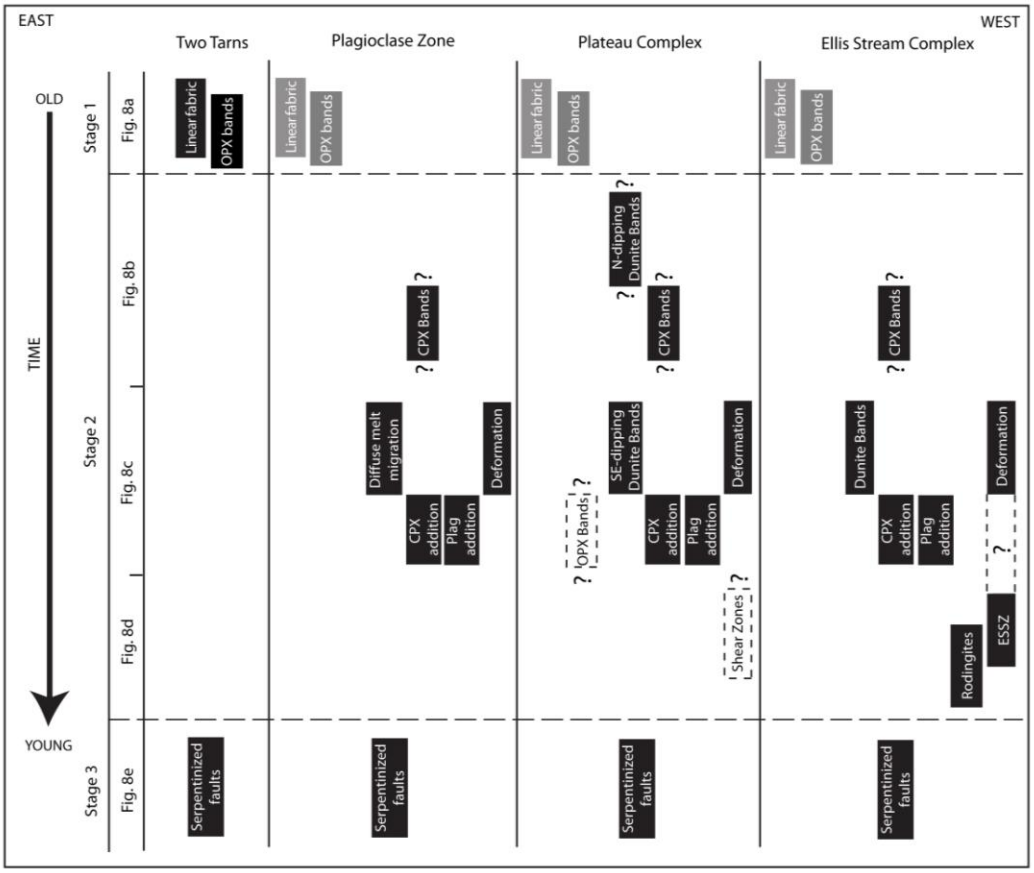

Figure 7 – Development of compositional heterogeneity and overprinting deformations as a function of time. Grey shaded areas are hypothetical, and are presumed to have been overprinted by later deformation. Dashed areas are proposed in Webber et al. (2010). Question marks reflect uncertainty over relative timing.

on the boundary conditions for deformation in the mantle wedge during the early stages of subduction. L-tectonites can result from three-dimensional transtensional deformation (Fossen and Tikoff, 1993; Dewey et al., 1998). Other simple finite strain models for the development of dominantly linear fabrics can be quantified (Fossen and Tikoff, 1998; Tikoff and Fossen, 1999), but these models also typically accommodate oblique divergence but with margin parallel elongation or shortening. Progressive folding and overprinting deformations can also produce L-tectonites (see review by Sullivan, 2013),

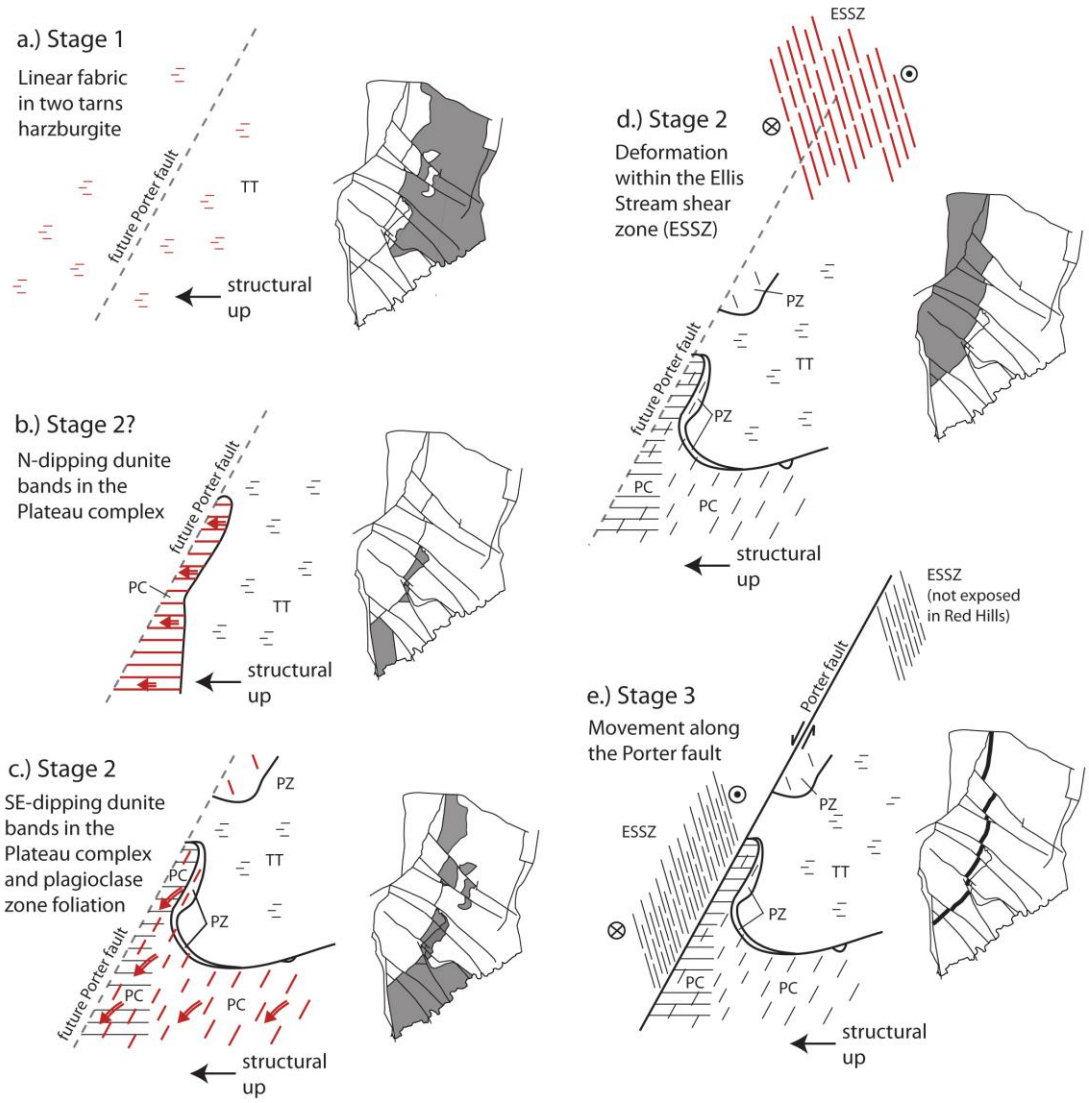

Figure 8 – Overprinting history of the Red Hills. Shaded portions of the accompanying maps show locations within the massif where the depicted fabrics occur today. Red lines and arrows represent zones of active melt migration, black lines represent inactive, former zones of melt migration. Structural up is to the west due to Mesozoic rotation from the Nelson regional syncline. TT=two tarns harzburgite. PC=Plateau complex. PZ=plagioclase zone. ESSZ=Ellis Stream shear zone.

but the two tarns harzburgite shows no evidence of folding or multiple deformation events. Consequently, I attribute the lineated harzburgites to transtensional deformation, which indicates mantle flow during the early stages of subduction initiation is three-dimensional, and includes an important transcurrent component of flow. Transtension is

also predicted to produce seismically fast olivine P-wave propagation and S-wave polarization directions oblique to the tectonic margin (Tommasi et al., 1999), thus modern and ancient examples of subduction initiation settings may often be characterized by margin oblique seismic anisotropy.

Stage 2: L-S shear zones and deformation in the Plateau complex, plagioclase zone, and Ellis Stream complex (1000°C, 5 kbar)

Stage 2 deformation occurred within the Ellis Stream complex, plagioclase zone, and in the southeast-dipping fabric in the Plateau complex. Stage 2 deformation overprinted Stage 1. Deformation was likely synchronous with compositional changes in Stage 2 units, resulting in dunite and clinopyroxene band development and localized, diffuse clinopyroxene and plagioclase refertilization (Fig. 7). Temperatures and pressures of deformation were lower than those of Stage 1, occurring at approximately 1000°C and 5 kbar. The role of each map unit in Stage 2 deformation is highlighted below.

Plateau complex

The Plateau complex contains an early, north-dipping event and a later, southeast-dipping deformation event (Fig. 4e). The timing and conditions for the early, north-dipping dunite and clinopyroxene compositional bands in the Plateau complex remains uncertain. It may have developed synchronously with Stage 1, or may have immediately preceded the rest of Stage 2 melt migration and deformation (Fig.7, 8b). The history of this early, north-dipping compositional layering is dealt with in more detail in Webber et al. (2008; 2010).

Deformation in the Stage 2 Plateau complex represents an important change in the style of deformation in the mantle wedge. A key point is that as the massif was exhumed to shallower depths from Stage 1 to Stage 2, deformation changed from homogeneous to localized. Deformation in the Plateau complex produced L-S fabrics (lineation and foliation) rather than nearly pure linear fabrics. As a result, deformation from plate boundary conditions during Stage 2 was likely accommodated by multiple, discrete L-S deformation zones rather than by homogeneous flow.

Plagioclase zone

I link deformation associated with the second dunite band formation event (dipping southeast) in the Plateau complex to deformation associated with the plagioclase zone (Fig. 7). I suggest that the transition from the plagioclase zone to the Plateau complex represents a transition from a pervasive, percolating melt (plagioclase zone) to channelized melt (Plateau complex). Thus the contrasting lithologies of the two units were caused by contrasting melt migration styles. Linking the kinematic history across the Plateau complex and plagioclase zone ties the deformational history of the massif to its compositional development. Stage 2 melts not only resulted in both localized depletion (dunite bands) and refertilization (plagioclase lherzolite, plagioclase harzburgite, or clinopyroxene and/or plagioclase bearing dunite), but also localized strain into the areas containing interstitial melt.

Ellis Stream complex

Geothermometry in the Ellis Stream complex suggests equilibration at approximately 1000°C, suggesting the Ellis Stream complex was involved in the same

melting/refertilization episode as the Plateau complex and plagioclase zone (Fig. 7, 8d). Unlike the Plateau complex and plagioclase zone, structural block I of the Ellis Stream complex is characterized by systematic changes in foliation orientations across the unit (i.e. Fig. 4g), and therefore likely represents a ductile shear zone. I name this structure the Ellis Stream shear zone. Structural block II of the Ellis Stream complex is characterized by a wider distribution of foliations, and likely represents parts of the Ellis Stream complex either weakly deformed by the shear zone or not deformed at all. A late-stage serpentinized fault brought structural block II in contact with block I (see Plate 1). Deformation in the shear zone may have occurred well below 1000°C, as suggested by the deformed late-stage hydrous rodingite bands (Fig. 3g). Thus the lithologic unit named the Ellis Stream complex likely formed at approximately 1000°C, but shear zone deformation, at temperatures lower than 1000°C and perhaps overlapping in time with Stage 3, overprinted large parts of the unit (Fig. 7).

Stage 3: Serpentinized faulting along the Porter fault (<600°C)

Movement along the Porter fault (Fig. 3h, 8e) and along parts of the bounding mélanges (see Plate 1) occurred at relatively cool temperatures (<600°C), based on the presence of serpentine within those fault zones. The style of deformation at these relatively cool conditions (<600°C) continued the trend of increasingly localized strain with decreasing temperature. The presence of the Porter fault along the eastern boundary of the Ellis Stream complex indicates the Ellis Stream complex is structurally detached from the rest of the massif. As a result, I do not believe the Red Hills contains a

continuous section from refractory harzburgite into the Moho transition zone (Sano and Kimura, 2007). Rather, it is a composite body of several structural blocks.

Role of coupled melt migration and deformation in mantle tectonics

The Red Hills provides an example of deformation coupled to channelized, focused melt migration, as seen at the map scale as the Stage 2 units (Plateau and Ellis Stream complexes and plagioclase zone) and at the outcrop scale as dunite bands. The relative importance of stress-driven melt segregation and channelization (Stevenson, 1989; Zimmerman et al., 1999; Holtzman et al., 2003a) relative to melt segregation caused by a reaction infiltration instability from chemical reactions between ascending melt and solid mantle (Daines and Kohlstedt, 1994; Aharonov et al., 1995; Spiegelman et al., 2001) remains largely unknown. Plateau and Ellis Stream complex dunite band orientations in outcrop (Fig. 3c) closely resemble the anastamozing networks of dunite-rich melt channels observed experimentally in simple shear experiments (Holtzman et al. 2003a, Holtzman et al., 2003b), and do not resemble as closely the predicted series of progressively coalescing channels (visually similar to an overturned tree), that form from reaction infiltration instabilities (e.g. Spiegelman et al., 2001). The close association between deformation and melt migration in the Red Hills supports the idea that focused melt extraction in the mantle is often associated with localized deformation, though reaction infiltration instabilities may also play a role in melt channelization, acting concurrently with deformation.

The multi-stage history of melt migration and deformation in the RHUM also

provides a unique opportunity to examine how melt and deformation change during progressive exhumation. The homogeneous outcrop appearance and relative lack of dunite bands suggests melt in the two tarns harzburgite (Stage 1) was homogeneously distributed at the outcrop and map scale, while melt in the Plateau and Ellis Stream complexes (Stage 2) show evidence of melt localization at two scales: 1) At the outcrop scale as dunite bands; and 2) As broad refertilized domains (e.g. Sano and Kimura, 2007) represented by the Stage 2 map units (Plateau and Ellis Stream complexes, plagioclase zone). During Stage 1 deformation, melt and strain were homogeneously distributed (Fig. 8a). However, by exhumation to approximately 5 kbar and 1000°C, melt and strain became focused into discrete regions, expressed at the map scale by the Plateau and Ellis Stream complexes and the plagioclase zone (Figs. 8c, 8d), and at the outcrop scale by dunite bands and dunite pods. I view the Plateau complex, plagioclase zone, and Ellis Stream complex map units as the remnants of former melt conduits that transported melt upwards, presumably towards a forearc spreading axis.

The geometry of the overprinting contact between the Stage 2 plagioclase zone and Plateau complex with the Stage 1 two tarns harzburgite is also important for understanding how melt becomes focused upward through the mantle wedge, and how strain develops. Both geologic map and cross-section views (Fig. 2, Fig. 8c) suggest the overprinting Stage 2 deformation in the Plateau complex and plagioclase zone was highly non-planar (i.e. not a shear zone). In cross-section, the contact resembles a synform (Fig. 2). However, the curved overprinting contact has nothing to do with folding, as the late-stage, cross-cutting southeast-dipping foliations within the Plateau

complex are reasonably consistent (Fig. 2, Fig. 4e), and lineations in the two tarns harzburgite (Fig. 4b) show no evidence of being folded (i.e. do not rotate about a small circle in the equal area stereographic plot). Rather, I conclude that the geometry of the contact is original, and developed in the mantle. The highly non-planar geometry of the contact suggests melts are focused upwards in complex geometries. Because deformation and melt migration are coupled, it also implies that deformation does not necessarily occur in planar shear zones in the high temperature mantle wedge, but instead also occurs in more complex, non-planar geometries.

The exhumation and melt migration history within a forearc, incipient subduction setting for deformation and melt transport, suggest that at relatively high pressures and temperatures (Stage 1), melt and strain beneath forearc spreading centers are homogeneous (Fig. 8a). Exhumation and cooling to 5 kbar pressure and1000°C (Stage 2) localizes melt and deformation into geometrically complex zones (Fig. 8c) in the shallow mantle wedge beneath the spreading axis. At even cooler temperatures in the serpentine stability field, deformation was accommodated by highly localized serpentinized faults (Stage 3, Fig. 8e).

SUMMARY

The 125 km^2 Red Hills ultramafic massif contains evidence for multiple overprinting fabrics that developed during exhumation in the early stages of subduction initiation. Importantly, the compositional evolution of the massif is linked to three

stages of deformation. I recognize the following compositional members and interpret their tectonic significance as follows:

1. The two tarns harzburgite is a pervasively lineated massive harzburgite, and represents the first stage of deformation in the massif. The unit formed at roughly 1200°C and >6 kbar, and is the oldest and deepest unit preserved in the Red Hills. Melting and deformation are inferred to have initiated in the garnet stability field and continued into the spinel stability field (Sano and Kimura, 2007). The L-tectonites are interpreted to result from transtensional deformation during the early stages of subduction initiation.
2. The plagioclase zone consists of plagioclase lherzolites and plagioclase harzburgites which equilibrated at ~1000°C and 4.4 to 5.1 kbar pressure. The plagioclase zone structurally overprints and petrologically refertilizes the two tarns harzburgite. The plagioclase zone is also part of the second stage of deformation.
3. The Plateau complex is composed of dominantly banded harzburgites and dunites, and equilibrated at ~1000°C and 4.8 to 5.4 kbar pressure. The Plateau complex structurally overprints, locally depletes (dunite bands), and locally refertilizes (lherzolite) the two tarns harzburgite, and is part of the second stage of deformation in the massif.
4. The Ellis Stream complex consists of banded harzburgites and dunites which equilibrated at ~1000°C and within the plagioclase stability field. This unit is structurally distinct from the other units, lying on the west side of Porter

fault. Deformation, expressed as strong foliation and folded and boudinaged pyroxenite bands, likely began synchronous with melt but continued well below the solidus temperature of peridotite. It is also part of the second stage of deformation.

The Porter fault represents the latest episode of exhumation related deformation (Stage 3) in the complex. The fault is a late-stage, left-lateral serpentinized fault that separates the westernmost Ellis Stream complex from the rest of the massif. It is the largest of a series of serpentine faults within the massif.

Using the geology outlined above, I develop a three-stage history for the massif that occurred during the early stages of renewed subduction along the Gondwanan margin. The lineated two tarns harzburgite represents the earliest and deepest fabric in the massif, and it formed in a transtensional setting associated with oblique divergence. Deformation was pervasive and homogeneous, and likely occurred synchronous with melt.

Progressive exhumation to ~5 kbar and cooling to 1000°C led to the localization of melt and deformation into restricted zones, whose fabrics are preserved in the Plateau complex, plagioclase zone, and the Ellis Stream complex. The geometry of the melt transport/deformation zones was complex and non-planar. Continued cooling and exhumation led to the formation of serpentinized faults, such as the Porter fault (Stage 3).

This study emphasizes the progressive changes in deformation style during mantle wedge exhumation. Deformation began homogeneously (Stage 1), but developed

into networks of supra- to sub-solidus deformation zones (5 kbar) (Stage 2), and eventually brittle faults (Stage 3). The transition from homogeneous deformation to shear zone deformation likely coincided with a localization of melt into map-scale (Stage 2 map units) and outcrop scale (dunite bands) conduits. This history provides a rare glimpse of the structures that sequentially develop in the early mantle wedge.

CHAPTER III

THE DEVELOPMENT OF HETEROGENEOUS MANTLE LITHOSPHERE IN A FOREARC ENVIRONMENT: AN EXAMPLE FROM THE RED HILLS ULTRAMAFIC COMPLEX, NEW ZEALAND

SYNOPSIS

This chapter documents the geochemical heterogeneity introduced into mantle lithosphere at the onset of subduction, where an essentially homogeneous mantle asthenosphere is converted into a compositionally heterogeneous mantle lithosphere as a result of increasingly focused melt ascent at shallower levels. Here I report field observations and geochemical results from the Red Hills ultramafic massif, part of the Dun Mountain Ophiolite Belt of New Zealand. In the east, the Red Hills contains geochemically homogeneous harzburgites (two tarns harzburgite). On its western and southern edge, the harzburgites are overprinted by a petrologically zoned sequence of foliated plagioclase lherzolite and plagioclase harzburgite on the periphery (plagioclase zone), and banded harzburgite and dunite (Plateau complex) on the interior. The western edge of the massif also contains banded harzburgite and dunite (Ellis Stream complex), but is separated from the rest of the massif by a major serpentinized fault (Porter fault).

Spinel Cr#-TiO_2 discrimination plots, linearly increasing fO_2 relative to Cr#, and highly anorthic plagioclase are interpreted to reflect a polygenetic multi-stage melting and refertilization model. The two tarns harzburgite is interpreted to record initial melting in a mid-ocean ridge setting in a relatively reduced environment (Stage 1a),

followed by additional melting in a more oxidized subduction zone environment (Stage 1b). The plagioclase-rich contact (plagioclase zone) between the two tarns harzburgite and the Plateau complex is interpreted to represent a refertilization front between the two tarns harzburgite and a petrologically zoned upper mantle melt transport network (Plateau complex - Stage 2), where melts became focused into kilometer-scale conduits. Our results indicate that discrete pulses of melts rise upward and are focused into narrower conduits towards the surface. Because shallow melt migration is localized into narrower zones, a significant percentage of mantle lithosphere in the forearc may be relict from earlier homogeneous mid-ocean ridge melting or deeper forearc melting, as seen in the Red Hills.

INTRODUCTION

Unraveling the history of metasomatism in upper mantle rocks is critical for understanding compositional changes in the mantle lithosphere through time. Metasomatism may alter various geophysical characteristics of the mantle lithosphere (e.g. O'Reilly and Griffin, 2013), such as its density and seismic shear wave velocity (Deen et al., 2006), bulk strength (Lenardic and Moresi, 1999; Poudjom Djomani et al., 2005), as well as its thermal characteristics (O'Reilly and Griffin, 2000).

Chemical reactions are thought to occur between ascending mantle melts and upper mantle peridotite. Percolative fractional crystallization (Harte et al., 1993) and other types of refertilization reactions during melt ascent can alter both the composition of the upper mantle (e.g. Takazawa et al., 1992; Batanova and Sobolev, 2000; Le Roux

et al., 2007; Batanova et al., 2011) and the ascending melt (Macpherson et al., 2006). Refertilization reactions and percolative fractional crystallization can cause changes in the modal mineralogy of the upper mantle (van der Wal and Bodinier, 1996; Le Roux et al., 2007), resulting in compositional heterogeneity. The scale of mantle heterogeneity is related to the scale of the metasomatizing melt transport networks.

Studies on the scale and geometry of the melt transport networks responsible for heterogeneity in the mantle are largely limited to studies of peridotite massifs (van der Wal and Bodinier, 1996; Batanova and Sobolev, 2000). However, even in ophiolites, it is often difficult to relate melt transport observations to fundamental mantle geology problems, such as upper mantle compositional heterogeneity, due to the difficulty in distinguishing the tectonic setting (i.e. mid-ocean ridge or supra-subduction zone) of dunite bands, refertilization fronts, and other fabrics attributed to melt migration.

There are two goals for this chapter: First to show that the Red Hills peridotite body was metasomatized by subduction zone melts; Second, to describe the geometry of a mantle wedge melt transport system and the geochemical and petrologic effects of melt ascent. I divide the chemical and compositional changes in the massif into two stages. The stages reflect early homogeneous melting first in a mid-ocean ridge environment, and continuing in a supra-subduction zone environment (Stage 1), and later focused melt ascent in a subduction zone environment (Stage 2).

GEOLOGICAL BACKGROUND

Dun Mountain ophiolite belt

The Red Hills ultramafic massif (RHUM) is a large, approximately 100 km^2 ultramafic body that is part of the Dun Mountain Ophiolite Belt (Fig. 9a) of the South Island, New Zealand. The crustal section of the Dun Mountain Ophiolite belt formed in a forearc environment (Sano et al., 1997; Sivell and McCulloch, 2000) in the middle Permian (Kimbrough et al., 1992). The ultramafics north of the Red Hills are typically thin (<2 km), heavily serpentinized, and contain small ultramafic blocks enclosed within a mélange. However, within the RHUM, the ultramafic section increases to approximately 8 km in width, and contains abundant, pristine ultramafic rocks unaltered during crustal emplacement.

Red Hills ultramafic massif

The RHUM has been mapped by Walcott (1969), Johnston (1982; 1990) and as part of this dissertation (Fig. 9b, Plate 1). The tectonic setting of the structural and geochemical development of the Red Hills remains debated. The tectonic setting has been interpreted as mid-ocean ridge (Sano and Kimura, 2007; Kimura and Sano, 2012) and as supra-subduction (Chapter II).

Based largely on the geochemical work of Sano and Kimura (2007), the Red Hills can broadly be divided into a refractory mantle domain, in the east, melted in the garnet and spinel stability fields, and a refertilized domain, in the west, with refertilization occurring in the plagioclase stability field (Fig. 9c). Sano and Kimura

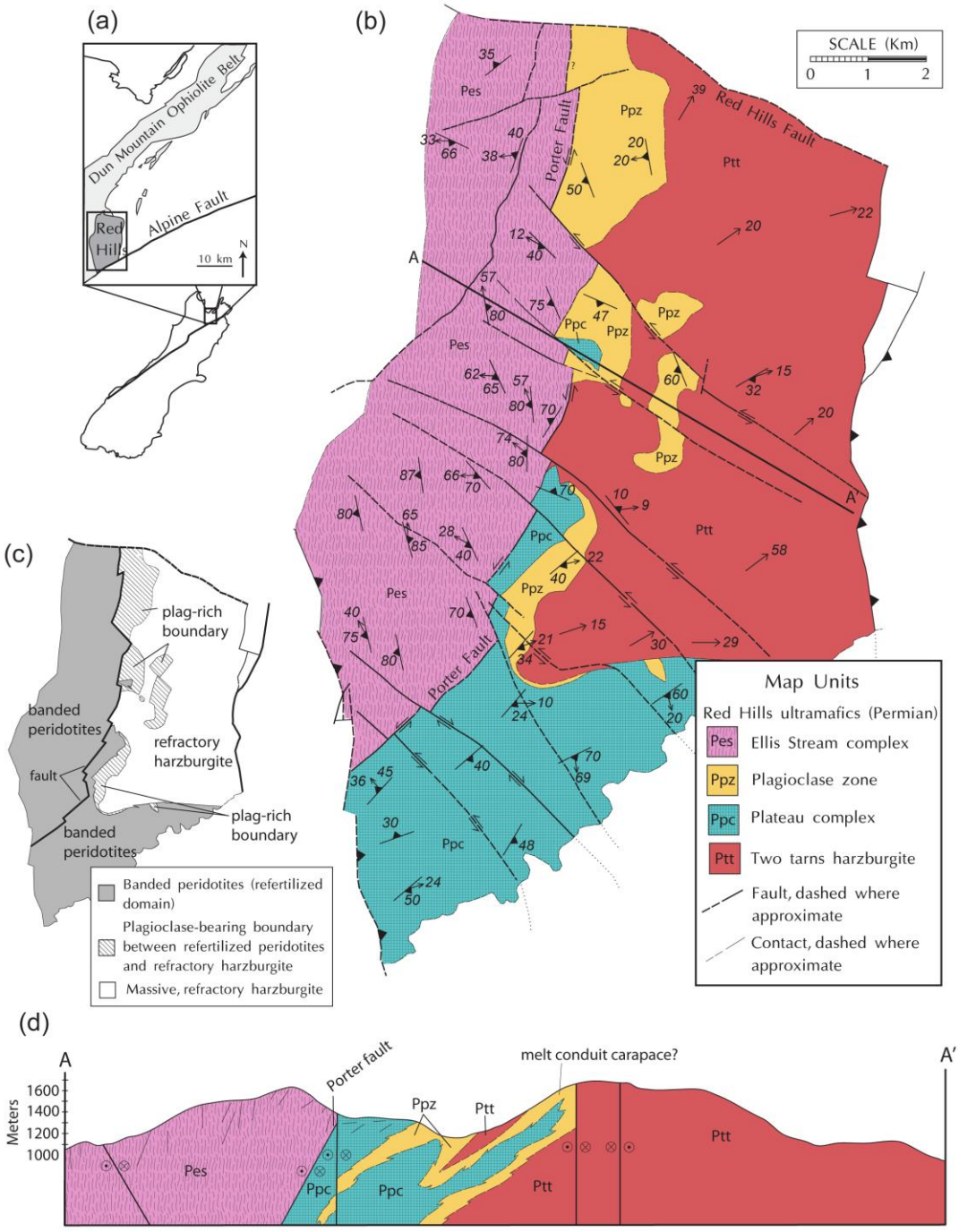

Figure 9 – Simplified geologic maps and cross-section. a.) Location map modified from Webber et al. (2008) for the Red Hills ultramafic complex, northern South Island, New Zealand. b.) Simplified geologic map of the Red Hills ultramafic complex from Plate 1. c.) Domain map of the Red Hills, showing regions of refertilization, regions of refractory mantle, and the plagioclase-bearing boundary. d.) Cross section perpendicular to the strike of the refertilized domain, showing a subsurface solution to the isolated lenses of the Plagioclase zone within the two tarns harzburgite. Note the interpretation of a zoned Plateau complex and plagioclase zone.

(2007) interpreted the western portion of the Red Hills complex to represent the Moho transition zone, and interpreted a continuous mantle section not cut by late-stage faults. However, Sano and Kimura (2007) only worked in the northern Red Hills massif. Mapping of the entire Red Hills (Plate 1) allows the geochemical model presented by Sano and Kimura (2007) to be tested and expanded to the entire massif. Importantly, the new mapping identifies a late-stage serpentinized fault (Porter fault), which suggests the western Red Hills is a separate structural block from the rest of the Red Hills, and is consistent with the earlier mapping of Johnston (1982; 1990). Stretching lineations in ductilely deformed basalt and plagiogranites within the fault zone pitch shallowly to the south, and display left-lateral shear sense indicators. The fault is likely a significant structure, because the steeply west-dipping fabric on the west side of the fault is truncated and does not reappear anywhere to the east of the fault. As a result, the structure has at least several kilometers of left-lateral slip, and indicates the Red Hills is not a continuous mantle section from refractory harzburgite into the Moho transition zone. In this paper I revise the Sano and Kimura (2007) geochemical model and describe the geochemical and petrologic effects of focused melt transport which occurred entirely within the uppermost mantle.

In Chapter II, I divided the massif into four lithologic units, which can be grouped into refractory and refertilized domains. Below, I describe field observations and the existing interpretations for them.

Refractory mantle domain: Two tarns harzburgite

The two tarns harzburgite is a massive, poorly foliated (Fig. 10a), but pervasively

lineated harzburgite that occurs in the eastern half of the massif (Fig. 9b). It is interpreted to represent an L-tectonite, forming in a transtensional environment (see Chapter II). Geothermobarometry (see Chapter II) for the two tarns harzburgite suggest equilibration at temperatures around 1200°C and pressures in excess of 6 kbar. Geochemical modeling of clinopyroxene and whole-rock rare earth elements by Sano and Kimura (2007) and Kimura and Sano (2012) suggest melting may have initiated at higher pressures in the garnet stability field, and continued into the spinel stability field.

The two tarns harzburgite is interpreted to represent refractory mantle (Sano and Kimura, 2007; Chapter II). Evidence for its refractory nature includes extreme depletion in light rare earth elements relative to middle and heavy rare earth elements in clinopyroxene (Sano and Kimura, 2007). Foliated peridotites of the Plateau complex and plagioclase zone overprint the linear fabric of the two tarns harzburgite (Chapter II), indicating the two tarns harzburgite is older than the Plateau complex and plagioclase zone.

Refertilized mantle domain: Plateau complex

The Plateau complex is composed of compositionally banded harzburgite and dunite (Fig. 10b). Plagioclase lherzolite and wehrlite occur sporadically across the unit. Dunite bands are either absent or less common where plagioclase lherzolite occurs. Chromitites occur within dunite bands, and reach approximately 10 cm in width. Clinopyroxenite bands are common, but represent a small fraction of the total rock volume (≤5%). Dunite bands often contain course-grained clinopyroxene elongate

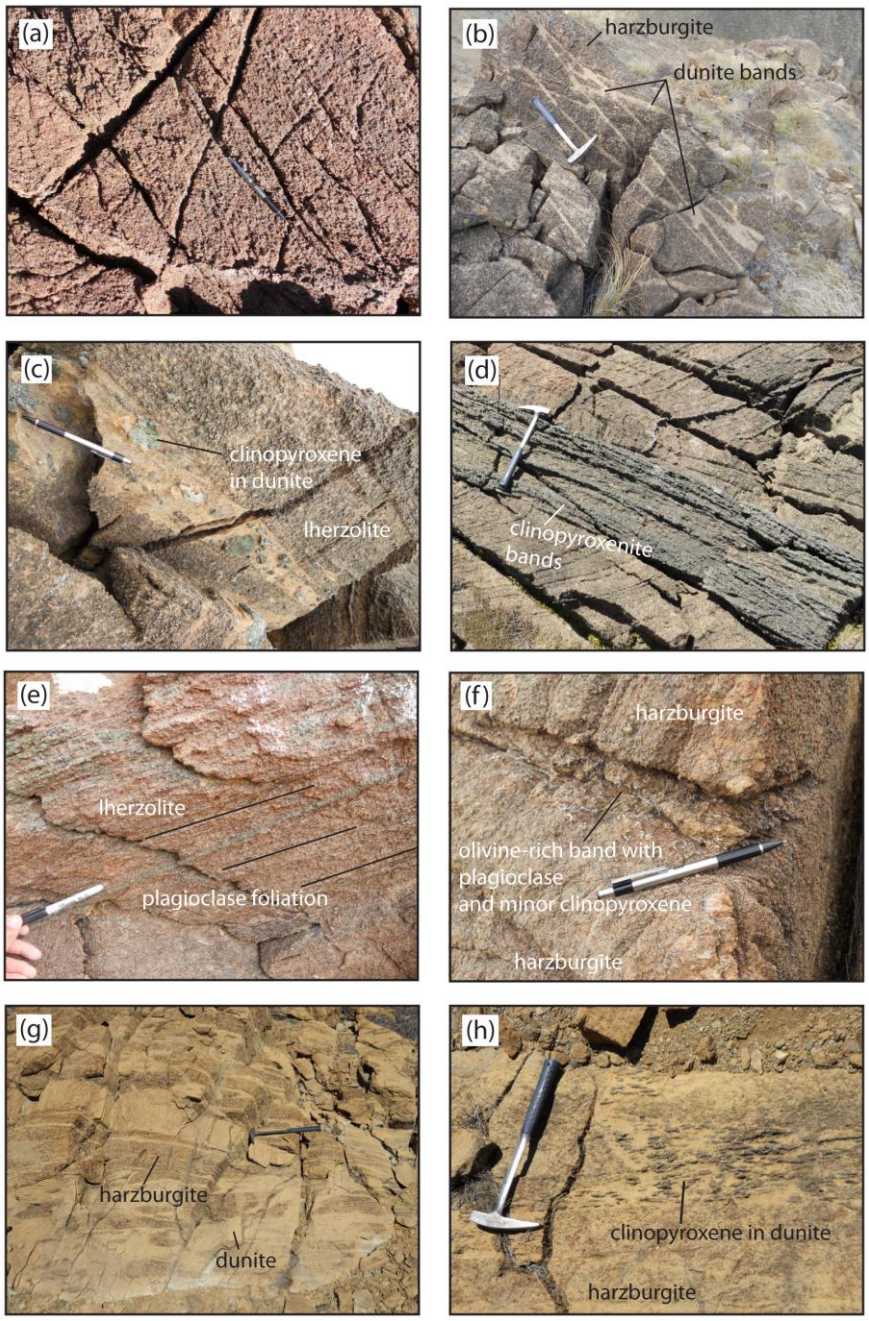

Figure 10 – Representative outcrop photos. a.) Massive, unfoliated two tarns harzburgite. b.) Compositionally banded harzburgite and dunite of the Plateau complex. c.) Large clinopyroxene grains within dunite bands. Note elongate, large clinopyroxene within the surrounding harzburgite, from the Plateau complex. d.) Numerous clinopyroxenite bands cross-cutting an earlier lherzolite and pyroxenite foliation, from the Plateau complex. e.) Wispy lenses of plagioclase within lherzolite defining a plagioclase foliation, from the plagioclase zone f.) Plagioclase and minor clinopyroxene within an olivine-rich band, from the northern plagioclase zone. g.) Banded harzburgite and dunite typical of the Ellis Stream complex. h.) Large clinopyroxene grains enclosed within a dunite band, from the Ellis Stream complex. Note the coalescence of clinopyroxene grains into small bands on the right-side of the photo.

parallel to the dunite bands (Fig. 10c), and less commonly plagioclase within dunite bands. Within dunite bands, a continuum from no clinopyroxene, to isolated, diffuse clinopyroxene (e.g. Fig. 10c) to nearly pure clinopyroxenite (Fig. 10d) occurs. The Plateau complex outcrops along the central and southern RHUM (Fig. 9b).

Geothermobarometry from Chapter II found the unit equilibrated at approximately 5 kbar and 1000°C. I linked the formation of dunite bands to the same melt migration event that resulted in plagioclase refertilization. On the basis of the similarity in geothermobarometry estimates, I interpreted the Plateau complex, the plagioclase zone and Ellis Stream complex as mantle infiltrated by percolating melts in the plagioclase stability field (part of the refertilized domain, Fig. 9c).

Refertilized mantle domain: Plagioclase zone

The plagioclase zone (Fig. 9b), the boundary between the two tarns harzburgite and the Plateau complex, is characterized by discontinuous lenses and sills of foliated plagioclase-lherzolite and plagioclase-harzburgite (Fig. 10e). Plagioclase-bearing peridotite is far more common in the plagioclase zone than in the interior of the Plateau complex and Ellis Stream complex. In the northern RHUM, the plagioclase zone is aerially more abundant than in the south (Fig. 9b), contains more abundant plagioclase harzburgite than in the southern plagioclase zone, and also contains large areas of massive harzburgite (without plagioclase) between plagioclase-bearing outcrops.

Sano and Kimura (2007) and Chapter II of this dissertation considered this unit to represent initially refractory mantle peridotite (i.e., two tarns harzburgite) that was refertilized by percolating melts in the plagioclase stability field. In Chapter II, I

calculated equilibration temperatures of approximately 1000°C and pressures of 5 kbar, identical to results derived from the Plateau complex. I also interpreted melt-rock reaction microstructures, and interpreted deformation synchronous with melt ascent. These results differ from work by Webber et al. (2008) who calculated lower temperatures (~850°C) from rocks they mapped as the Eastern Domain (which I include in the plagioclase zone).

Refertilized mantle domain: Ellis Stream complex

The Ellis Stream complex is composed of compositionally banded harzburgite and dunite (Fig. 10g) with minor lherzolite, and is located in the western part of the RHUM. The Ellis Stream complex contains more dunite and less lherzolite than the Plateau complex. Similar to the Plateau complex, cm-scale clinopyroxene grains commonly occur within dunite bands (Fig. 10h). The clinopyroxene grains are often elongate parallel to the boundaries of the dunite bands. The complex contains common clinopyroxenite bands and less common orthopyroxenite bands; together the pyroxene bands represent less than 5% of the volume of the rock. Less common, the Ellis Stream complex contains interstitial plagioclase within dunite bands (Sano and Kimura, 2007).

The Ellis Stream complex is structurally detached from the rest of the massif. Johnston (1982; 1990) and mapping as part of this dissertation (Plate 1) recognized the Porter fault, which lies along the eastern contact of the unit. In Chapter II, I interpreted the Ellis Stream complex as post-dating the creation of the two tarns harzburgite, and concurrent with the low pressure (plagioclase stability field) deformation and melt ascent event that formed the Plateau complex and plagioclase zone. Sano and Kimura (2007),

who did not incorporate the presence of the Porter fault into their model, interpreted this unit to represent the Moho transition zone. They further linked the development of channelized melts and the creation of dunite bands in the unit to melting of the massive harzburgites of the eastern massif (two tarns harzburgite).

WHOLE-ROCK COMPOSITION AND MAJOR AND TRACE ELEMENT GEOCHEMISTRY

Methods

Whole-rock mineral modes and major and trace element compositions were determined from across the massif to test for a supra-subduction zone history for the rocks from the Red Hills, and to elucidate possible lithologic and major and trace element geochemical trends. I sampled rocks in the refractory and refertilized domains (Fig. 9c). Most samples were taken from the central and southern RHUM, south of where Sano and Kimura (2007) and Kimura and Sano (2012) sampled. Modal compositions were based on >500 points per thin section. Sample locations and point count results are provided in Appendix B.

Major and trace element abundances were analyzed at the Washington State University Geoanalytical Lab. All samples were cut large enough to be representative of bulk composition, and weathering rinds were removed. Major elements were analyzed by x-ray fluorescence (XRF). Samples were powdered in a high purity tungsten carbide swing mill, mixed at a 1:2 ratio with dilithium tetraborate, and fused in graphite crucibles at 1000°C. Samples were then reground and refused a second time. Full

operating procedures for the XRF are given in Johnson et al (1999). Heating for loss on ignition (LOI) values was done at 900°C in quartz crucibles, which can cause some oxidation of the sample, thus some LOI values are negative.

Trace elements were analyzed by inductively coupled plasma mass spectrometry (ICP-MS). All analyzed samples were completely dissolved through a mixed fusion-dissolution method. Full sample preparation and analytical procedures are found in Knaack et al. (1994). Detection limits for analyzed elements are included in Appendix B. Analysis by these methods yields generally good precision, even at sub-chondritic values. I gauge overall precision on our samples by calculating relative percent difference (RPD) on duplicate analyses of sample RH12_23_3. All rare earth elements show good agreement, and are within 10% RPD (Table 5). Large ion lithophile and high field strength elements generally show less precision (Table 5). Niobium shows a 40% RPD, in part due to its extremely low values close to detection limit. The accuracy of the method at near primitive mantle trace element levels, as gauged by RPD values for international standards FK-N (K-feldspar) and BIR-1 (basalt) is generally good (Knaack, unpublished data), and overall tracks the precision of the method. Light rare earth element accuracy is typically within 20% RPD, while middle and heavy rare earth elements at primitive mantle levels are between 40 and 60% (Knaack, unpublished data). Niobium shows more variability, yielding RPD values of 52% and -13% for the two standards (Knaack, unpublished data).

Results

Modal compositions of each map unit plotted on an Ol-Opx-Cpx ternary diagram illustrate the lithologic differences between the different units, and show the internal variability within each unit (Fig. 11a). I also plot modal abundances calculated by Sano and Kimura (2007), who extensively sampled the northern RHUM. Samples from the two tarns harzburgite plot within a narrow range in the harzburgite field (isolated occurrences of dunite also occur in the unit). Figure 11b-d highlight the differences between the two tarns harzburgite and the Plateau complex, plagioclase zone, Ellis Stream complex, respectively. The Plateau complex, plagioclase zone, and Ellis Stream complex have significantly more variability than the two tarns harzburgite, plotting within the dunite, lherzolite, and harzburgite fields.

Whole-rock major element results are shown in Table 4, and select oxides are plotted on Figure 12. Al_2O_3 values vary from highly refractory (0.18 wt%) to moderately fertile (3.3 wt%) across the massif. Plots of CaO vs. Al_2O_3 show strong positive correlation regardless of lithologic map unit, though several samples deviate from the main trend. A plot of CaO wt.% versus MgO wt.% shows an overall negative correlation, but higher CaO values result in progressively reduced changes in MgO, producing an apparent non-linear relationship between CaO and MgO. Within the overall trends described above, samples from the two tarns harzburgite plot within a relatively narrow range in major elements. Samples from the other three units show more variability ranging from significantly more depleted values (higher MgO, lower SiO_2), to significantly more enriched values (higher Al_2O_3, CaO).

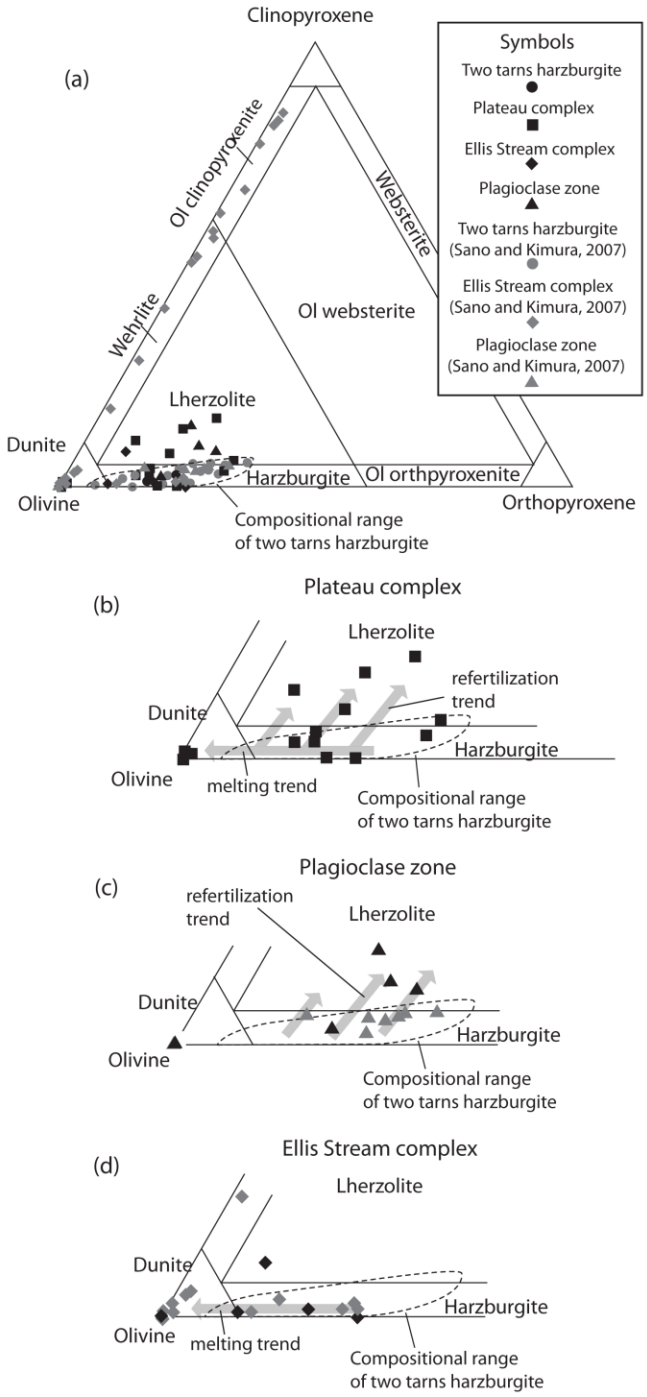

Figure 11 – Ternary ultramafic composition diagrams (modified from Sano and Kimura, 2007). Samples from Sano and Kimura (2007) were re-plotted onto the map units defined in Chapter II. Dashed lines in 11b, 11c, and 11d represent the range in composition for samples from the two tarns harzburgite. Arrows approximate the melting and refertilization trends which altered the composition of the two tarns harzburgite, and produced the range in compositions seen in the Plateau complex, plagioclase zone, and Ellis stream complex.

Sample	Map Unit	SiO2	TiO2	Al2O3	FeO	MnO	MgO	CaO	Na2O	K2O	P2O5	Sum	LOI (%)
RH12ES01	**ES**	39.5	0.01	1.46	11.04	0.17	46.49	0.50	0.05	0.00	0.01	99.3	0.00
RH12ES02	**ES**	39.0	0.00	0.19	8.76	0.13	48.76	0.16	0.00	0.00	0.00	97.1	2.14
RH12ES12	**PC**	41.8	0.03	1.70	8.59	0.13	43.16	2.96	0.05	0.00	0.00	98.4	0.62
RH12ES13	**PC**	43.6	0.01	1.54	8.52	0.13	44.76	1.01	0.02	0.00	0.00	99.6	-0.27
RH12ES14	**TT**	44.5	0.01	1.38	8.22	0.13	43.88	1.45	0.00	0.00	0.00	99.6	-0.21
12RH7	**PC**	43.7	0.01	0.81	9.03	0.14	45.06	0.97	0.00	0.00	0.00	99.7	-0.14
12RH10	**PC**	44.4	0.01	1.47	8.14	0.13	42.62	2.09	0.00	0.00	0.00	98.9	-0.02
12RH14A	**PC**	41.5	0.03	2.46	9.02	0.14	42.48	2.62	0.09	0.00	0.00	98.3	0.77
12RH14B	**PC**	40.1	0.01	0.61	10.0	0.15	47.77	0.37	0.00	0.00	0.00	99.0	-0.05
12RH22	**TT**	43.6	0.01	0.66	8.55	0.14	45.41	0.83	0.00	0.00	0.00	99.2	-0.16
12RH23	**PZ**	40.0	0.00	0.18	8.93	0.13	48.77	0.12	0.00	0.00	0.00	98.1	0.49
12RH24	**PZ**	47.3	0.04	3.32	7.37	0.13	38.33	2.65	0.07	0.00	0.00	99.3	0.06
12RH25	**PZ**	45.1	0.02	1.64	8.17	0.13	42.59	2.21	0.00	0.00	0.00	99.8	-0.12
12RH27	**ES**	42.4	0.01	0.82	8.50	0.13	44.55	0.79	0.02	0.00	0.00	97.2	1.85
12RH28	**PC**	44.8	0.01	1.43	8.12	0.13	42.57	1.91	0.00	0.00	0.00	99.0	0.33
12RH33	**PC**	42.8	0.00	0.42	8.74	0.14	46.33	0.45	0.00	0.00	0.00	98.8	0.50
11ES05	**TT**	44.5	0.00	0.40	8.64	0.14	44.91	0.54	0.00	0.00	0.00	99.1	0.27
11ES06	**TT**	40.2	0.00	0.34	8.43	0.12	48.78	0.20	0.00	0.00	0.00	98.1	0.58
11ES12	**ES**	42.8	0.01	0.75	7.96	0.13	44.86	0.52	0.00	0.00	0.00	97.0	1.81
11ES19	**TT**	44.1	0.01	0.75	8.21	0.13	45.12	0.82	0.00	0.00	0.00	99.2	-0.24
11ES24	**TT**	43.5	0.01	0.68	8.24	0.13	45.14	0.56	0.00	0.00	0.00	98.3	0.95
11ES26	**PC**	45.5	0.01	1.20	7.34	0.12	43.34	0.95	0.00	0.00	0.00	98.5	0.44
RH12-14A	**PZ**	43.7	0.01	0.82	8.71	0.14	44.81	1.00	0.00	0.00	0.00	99.2	0.29
RH12-18-2	**ES**	44.5	0.01	1.31	8.15	0.13	43.10	1.47	0.02	0.03	0.00	98.7	0.59
RH12-22-3	**ES**	42.9	0.05	2.02	9.12	0.14	42.89	1.90	0.09	0.00	0.00	99.1	-0.16
RH12-23-1	**PZ**	43.3	0.03	0.94	8.55	0.13	45.37	0.88	0.00	0.00	0.00	99.2	-0.23
RH12-23-2	**PZ**	44.7	0.01	1.18	8.41	0.13	43.82	1.32	0.00	0.00	0.00	99.6	-0.22

Table 4 – Whole-rock major element compositions. ES=Ellis Stream complex, PC=Plateau complex, TT=two tarns harzburgite, PZ=plagioclase zone, LOI=loss on ignition.

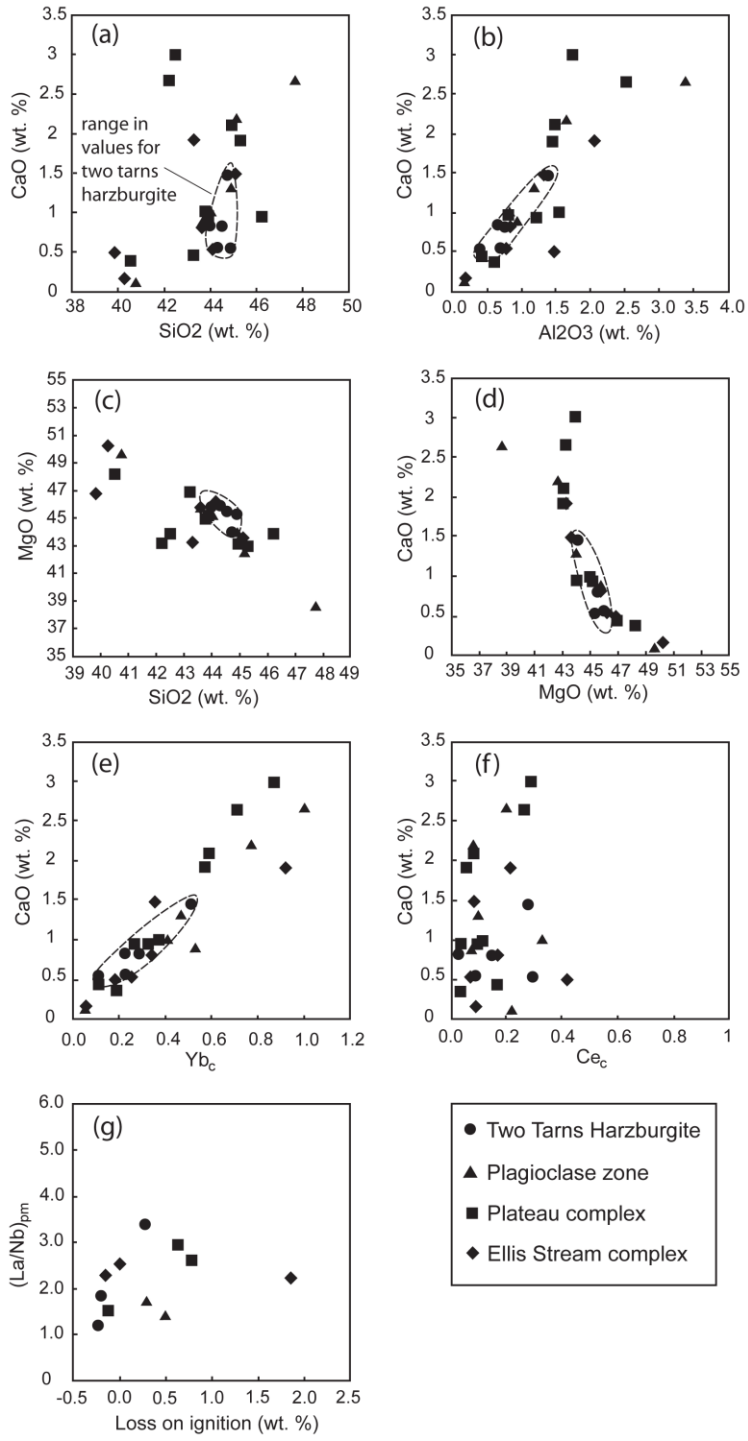

Figure 12 – Whole-rock major and select trace elements. Dashed lines outline the range in values for the two tarns harzburgite for comparison to the other units. Black circles are samples from the two tarns harzburgite, triangles are plagioclase zone, squares are Plateau complex, and diamonds are Ellis Stream complex.

Trace element abundances are given in Table 5, and select elements are plotted on Figures 12-14. Many elements had extremely low concentrations, and some trace element analyses were below detection limit for the ICP-MS. These analyses are not plotted on the figures. Several notable trace element trends are evident in Figures 12 and 13. Chondrite normalized abundance of Yb plotted relative to CaO wt. % shows strong positive correlation (Fig. 12e), while the light rare earth element (LREE) chondrite normalized abundance of Ce relative to CaO shows no correlation (Fig. 12f). Chondrite normalized rare earth element plots from each of the four lithologic units are given in Figure 13. Notably, relative to middle rare earth elements (MREE), all samples from the two tarns harzburgite show LREE enrichment. Heavy rare earth element (HREE) values are moderately depleted, and middle rare earth element values typically fall below detection limit. Lherzolites and harzburgites from the Plateau complex and plagioclase zone typically have less pronounced LREE enrichment relative to the MREE, and have overall higher middle and heavy rare earth element values compared to the harzburgites of the two tarns harzburgite. Dunites from the Plateau and Ellis Stream complexes have REE values that are generally below detection limit, precluding comparisons to other samples. Results from these dunites are included in Table 5, but are not plotted on Figure 13. Harzburgites from the Ellis Stream complex show minor LREE enrichment relative to middle rare earth elements.

Primitive mantle normalized incompatible element plots show consistent enrichment in highly incompatible elements in all lithologic units (Fig. 14). Most samples display negative Ba anomalies, which was likely caused by late-stage

	RH12 ES01	RH12 ES02	RH12 ES12	RH12 ES13	RH12 ES14	12RH 7	12RH 10	12RH 14a	12RH 14b	12RH 22	12RH 23	12RH 24	12RH 25
Map Unit *	ES	ES	PC	PC	TT	PC	PC	PC	PC	TT	PZ	PZ	PZ
La	0.105	0.023	0.074	0.030	0.079	0.028	0.021	0.083	0.015	0.008	0.065	0.052	0.017
Ce	0.257	0.057	0.178	0.070	0.171	0.062	0.051	0.163	0.023	0.020	0.135	0.122	0.052
Pr	0.030	DL	0.021	DL	0.023	DL	DL	0.020	DL	DL	0.018	DL	DL
Nd	0.130	DL	0.101	DL	0.069	DL	DL	0.106	DL	DL	0.056	DL	DL
Sm	0.035	DL	0.061	DL	0.018	DL	DL	0.055	DL	DL	DL	0.025	0.022
Eu	0.015	DL	0.024	DL	DL	DL	DL	0.025	DL	DL	DL	0.014	DL
Gd	0.026	DL	0.133	DL	0.035	DL	0.026	0.099	DL	DL	DL	0.082	0.064
Tb	DL	DL	0.030	DL	DL	DL	0.009	0.025	DL	DL	DL	0.021	0.016
Dy	0.030	DL	0.230	0.040	0.065	0.035	0.077	0.175	DL	DL	DL	0.183	0.128
Ho	0.007	DL	0.053	0.012	0.018	0.008	0.024	0.040	DL	DL	DL	0.046	0.035
Er	0.023	DL	0.151	0.047	0.071	0.033	0.084	0.117	DL	0.025	DL	0.141	0.113
Tm	DL	DL	0.024	0.008	0.012	0.006	0.014	0.018	DL	DL	DL	0.026	0.018
Yb	0.031	DL	0.147	0.063	0.087	0.045	0.099	0.120	0.031	0.037	DL	0.170	0.131
Lu	0.007	DL	0.028	0.014	0.017	0.010	0.020	0.019	0.007	0.009	DL	0.032	0.022
Ba	1.635	DL	0.360	0.337	1.521	DL	DL	2.214	DL	0.092	1.185	0.580	0.430
Th	0.038	0.015	0.043	0.016	0.033	0.012	0.013	0.046	DL	DL	0.012	0.009	0.011
Nb	0.043	DL	0.026	DL	0.044	0.019	DL	0.033	DL	DL	0.047	DL	DL
Y	0.167	0.034	1.363	0.314	0.487	0.235	0.603	1.017	0.109	0.170	0.065	1.184	0.863
Hf	DL	DL	0.037	DL	DL	DL	DL	DL	DL	DL	DL	DL	DL
Ta	DL	0.016	DL	DL	DL	DL	DL	DL	DL	DL	DL	DL	DL
U	DL	DL	0.015	DL	DL	DL	DL	DL	DL	DL	DL	DL	DL
Pb	DL	DL	DL	DL	DL	DL	DL	DL	DL	DL	DL	DL	DL
Rb	0.109	DL	0.083	DL	0.131	DL	DL	0.357	DL	DL	0.177	DL	DL
Cs	0.036	DL	0.031	0.026	0.028	0.018	0.022	0.035	0.023	0.023	0.036	DL	0.022
Sr	5.511	0.422	1.975	1.073	0.958	0.602	0.487	5.243	0.338	0.171	1.792	1.522	0.431
Zr	0.895	0.293	1.023	0.345	0.783	0.521	0.330	0.625	0.187	0.211	0.450	0.339	0.350

Table 5 – Whole-rock ICP-MS trace element results. All results are reported in parts per million.
*ES=Ellis Stream complex, PC=Plateau complex, TT=two tarns harzburgite, PZ is plagioclase zone.
**Relative percent difference between RH12-22-3 and duplicate analysis.

	12RH27	12RH28	12RH33	11ES05	11ES12	11ES19	11ES24	11ES26	RH12-14a	RH12-18-2	RH12-22-3	RH12-23-1	RH12-23-2	
Map Unit *	ES	PC	PC	TT	ES	TT	TT	PC	PZ	ES	ES	PZ	PZ	RPD **
La	0.041	0.014	0.054	0.09	0.018	0.042	0.025	0.007	0.095	0.022	0.060	0.019	0.027	7%
Ce	0.105	0.036	0.102	0.18	0.047	0.093	0.057	0.023	0.204	0.053	0.133	0.048	0.062	9%
Pr	0.011	DL	DL	0.02	DL	DL	DL	DL	0.027	DL	0.019	DL	DL	10%
Nd	DL	DL	DL	0.06	DL	DL	DL	DL	0.110	DL	0.127	DL	DL	11%
Sm	0.021	DL	DL	DL	DL	DL	DL	DL	0.029	DL	0.062	0.020	DL	8%
Eu	DL	DL	DL	DL	DL	DL	DL	DL	DL	DL	0.039	DL	DL	2%
Gd	DL	DL	DL	DL	DL	DL	DL	DL	0.033	DL	0.139	0.044	DL	2%
Tb	DL	0.009	DL	DL	DL	DL	DL	DL	DL	DL	0.029	0.011	DL	3%
Dy	0.045	0.077	DL	DL	0.036	0.030	DL	0.040	0.050	0.041	0.212	0.096	0.055	1%
Ho	0.012	0.019	DL	DL	0.010	0.009	0.007	0.010	0.014	0.012	0.051	0.023	0.016	7%
Er	0.041	0.080	DL	DL	0.030	0.032	0.025	0.035	0.047	0.039	0.144	0.077	0.056	3%
Tm	0.008	0.012	DL	DL	DL	DL	DL	0.007	0.009	0.008	0.023	0.012	0.010	2%
Yb	0.058	0.097	DL	DL	0.043	0.048	0.038	0.055	0.069	0.060	0.156	0.090	0.079	3%
Lu	0.011	0.018	DL	DL	0.011	0.011	0.010	0.008	0.013	0.012	0.025	0.016	0.016	2%
Ba	0.830	DL	DL	2.51	DL	0.711	DL	DL	2.361	0.319	1.407	DL	0.443	39%
Th	0.014	0.011	0.009	0.05	0.011	0.010	0.015	DL	0.027	0.012	0.055	0.010	0.015	62%
Nb	0.019	DL	DL	0.03	DL	0.036	DL	DL	0.057	DL	0.027	DL	DL	40%
Y	0.308	0.523	0.071	0.09	0.215	0.243	0.160	0.262	0.368	0.295	1.211	0.570	0.402	2%
Hf	DL	DL	DL	DL	DL	DL	DL	DL	DL	DL	0.034	DL	DL	17%
Ta	DL	0.018	0.033	0.03	0.025	0.028	0.029	0.022	0.034	0.027	0.032	0.032	0.032	11%
U	DL	DL	DL	DL	DL	DL	DL	DL	DL	DL	DL	DL	DL	-
Pb	DL	DL	DL	DL	DL	DL	DL	DL	DL	DL	DL	DL	DL	-
Rb	0.100	DL	DL	0.42	DL	0.128	DL	DL	0.183	0.062	0.487	DL	DL	109%
Cs	0.024	0.025	0.029	0.03	0.016	0.014	0.019	0.027	0.023	0.021	0.035	DL	DL	-
Sr	1.033	0.285	0.158	1.43	0.326	1.139	0.196	0.185	1.276	0.389	7.518	0.288	0.303	16%
Zr	0.467	0.273	0.218	0.58	0.302	0.326	0.278	0.268	0.748	0.305	0.780	0.504	0.354	38%

Table 5 (continued)

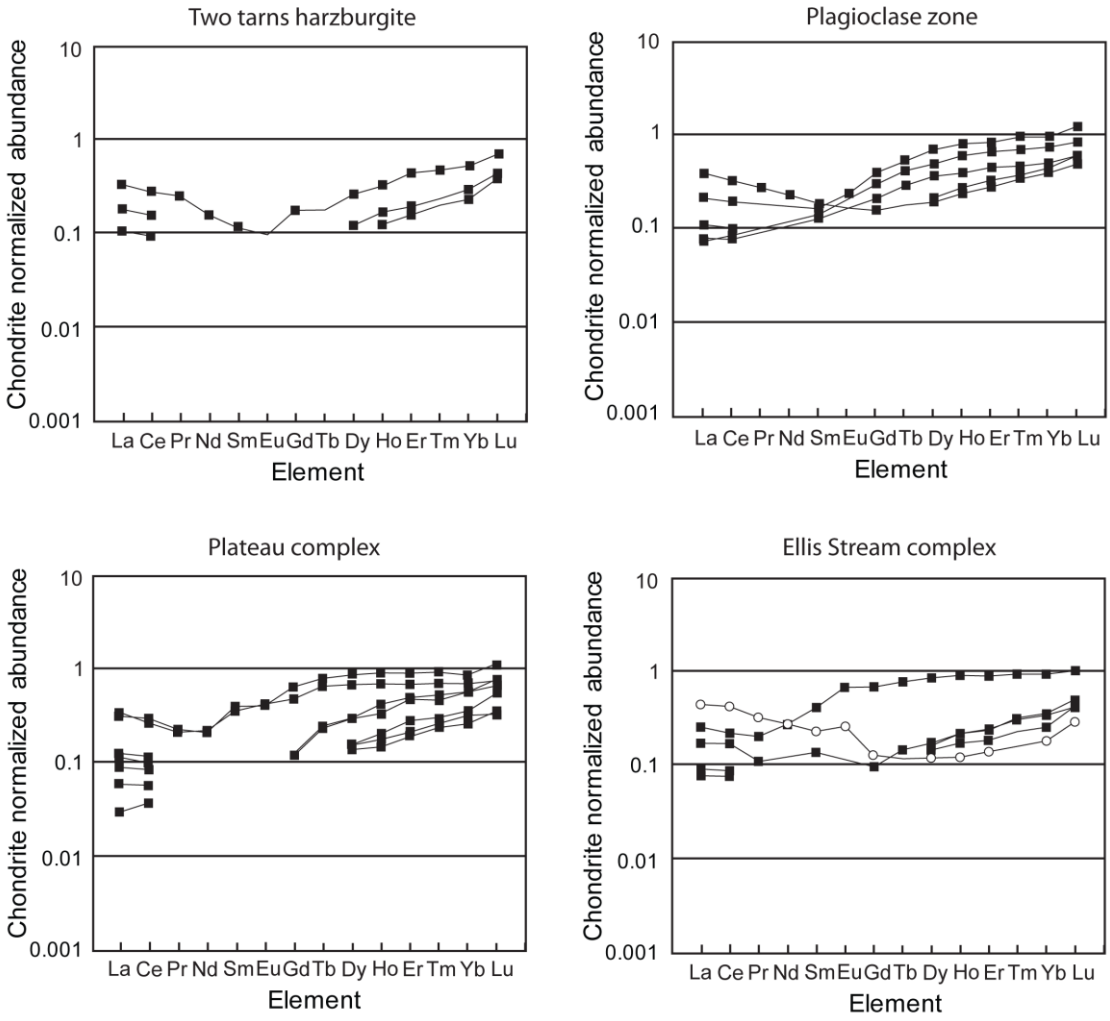

Figure 13 – Chondrite normalized rare earth element plots. Solid squares represent harzburgites and lherzolites. Open circles represent dunites. Chondrite rare earth element values come from Sun and McDonough (1989).

remobilization. Significantly, all samples regardless of lithologic unit also show negative Nb anomalies relative to elements of similar compatibility, such as La. La/Nb ratios for each sample plotted against their loss on ignition value (a guide to the amount of water in the sample) shows no correlation (Fig. 12g). Kimura and Sano (2012) found chondrite normalized positive Nb values relative to elements of similar compatibility for whole

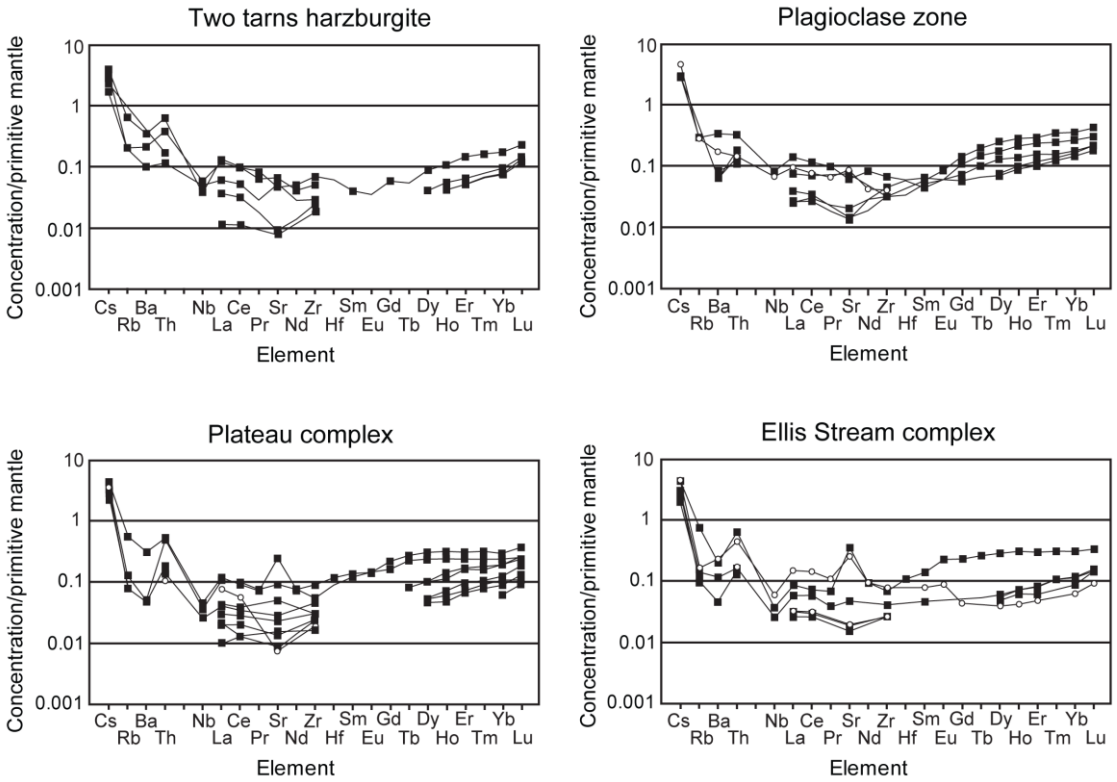

Figure 14 – Primitive mantle normalized incompatible element plots. Solid squares represent harzburgites and lherzolites. Open circles represent dunites. Note all units show negative Nb anomalies. Primitive mantle values come from Sun and McDonough (1989).

rock samples from the northern massif. Elevated Nb values often occur from contamination in low-purity tungsten carbide mills (e.g. Johnson et al., 1999). Although Kimura and Sano (2012) tested for Nb contamination and argued against it, our consistent negative Nb values suggest either: 1) The prior analyses were contaminated during milling; 2) Poor precision or accuracy in our analyses have produced unreliable results. Concerning the latter, the methods used in this study yielded results for international standards that show no systematic errors in accuracy for Nb (calculated results are both above and below reported values for international standards with primitive mantle-levels of Nb). Precision is also unlikely to be the cause of the anomaly.

Figure 12h is a histogram showing the distribution of $(La/Nb)_{PM}$ normalized values. Importantly, all values are above one. Using RPD values from sample RH12_23_3 as uncertainties, 8 of 11 samples retain $(La/Nb)_{PM}$ ratios over 1. Using the higher RPD values derived from standard analyses (50% for Nb, 20% La) as uncertainties, 6 of 11 samples retain $(La/Nb)_{PM}$ ratios over 1. Though this approach is clearly at the limits of the analytical method, I believe there is a reasonable probability that the negative Nb anomaly is real.

OXYBAROMETRY

In this section, I calculate oxygen fugacity (fO_2), or the chemical potential of oxygen, for a variety of samples from the Red Hills complex. fO_2 varies as a function of tectonic setting, and is generally higher in supra-subduction zones than mid-ocean ridges and sub-continental mantle (e.g., Wood et al., 1990; Ballhaus et al., 1991; Frost and McCammon, 2008; Dare et al., 2009). The cause of elevated fO_2 values in supra-subduction zone settings is not well understood, but may be related to elevated amounts of Fe_2O_3 released from the subducting plate either from partial melting or from released fluids (Lecuyer and Ricard, 1999). Subducting oceanic crust may contain relatively high amounts of Fe_2O_3 due to the abundance of magnetite, a byproduct of serpentinization reactions near the seafloor (e.g. Bach et al., 2004). Water is not thought to be an oxidizing agent in the upper mantle, as it is stable at upper mantle conditions (Frost and McCammon, 2008).

Oxidation of the mantle wedge may result from reaction with oxidized melts

during melt ascent. Studies of dredged forearc peridotites and mid-ocean ridge peridotites have found a relationship between increasing fO_2 and increasing spinel Cr# (Cr/Cr+Al) (Parkinson and Pearce, 1998; Pearce et al., 2000; Dare et al., 2009). Chromium number is directly related to the degree of melt depletion in peridotites (Hellebrand et al., 2001). Because subduction zone melts tend to be more oxidized than mid-ocean ridge melts, reaction with residual harzburgites and dunites tends to leave supra-subduction zone mantle with higher fO_2 than mid-ocean ridge mantle (Dare et al., 2009). However, where peridotites have undergone melting or melt reaction first in a mid-ocean ridge environment, and later in a supra-subduction zone environment (polygenetic melting history), the tectonic setting of melting can be difficult to pinpoint due to overlapping values (Dare et al., 2009). This is particularly prevalent in harzburgites with an early history of mid-ocean ridge melting but only a modest amount of supra-subduction zone melting; in these cases, fO_2 and Cr# values typically suggest only a mid-ocean ridge environment in tectonic discrimination diagrams. For this reason, fO_2 and Cr# for the most depleted harzburgites and dunites provide better examples of the oxidation state of the reacting melt.

Methods

Several empirically calibrated relations have been developed to calculate fO_2 in natural peridotite samples from electron microprobe data (Ballhaus et al. 1991; Wood, 1990; O'Neill and Wall, 1987). Both the Nell-Wood (Wood, 1990) and Ballhaus et al. (1991) methods calculate oxygen fugacity from the oxygen buffering reaction:

$$6Fe_2SiO_4(fayalite) + O_2(fluid) =$$

$$3Fe_2Si_2O_6(ferrosillite) + 2Fe_3O_4(magnetite) \quad (5)$$

I calculate the activities of the fayalite, ferrosillite, and magnetite components of natural olivine, orthopyroxene, and spinel, respectively, in the manner described by Wood (1990) for the Nell-Wood method and by Ballhaus et al. (1991) for the Ballhaus method. I applied two different temperatures to the fO_2 calculations. When using the Nell-Wood method, I calculate fO_2 at temperatures reported in Chapter II using the Taylor (1998) two-pyroxene thermometer. The Taylor (1998) two-pyroxene thermometer was found to provide the most accurate temperatures in a recent review of two-pyroxene thermometers (Nimis and Gruter, 2010). Several samples do not have Taylor (1998) two-pyroxene temperatures reported because clinopyroxene grain sizes were small, with the texture consistent with resetting or alteration during cooling, and the compositions of these grains resulted in unrealistically low temperature estimates. For these, I calculate fO_2 at the temperature calculated using the Ca-in-opx thermometer of Brey and Kohler (1990) as revised by Nimis and Gruter (2010). Values of fO_2 are strongly dependent on temperature, so values are reported relative to the fayalite-magnetite-quartz (FMQ) buffer of O'Neill and Wall (1987) calculated at the same temperature as the oxygen fugacity. For the Ballhaus method, I use the olivine-spinel thermometer of Ballhaus et al. (1991). This thermometer records the closure of Fe^{2+}-Mg exchange between olivine and spinel, and typically produces much lower temperatures than the Taylor (1998) two-pyroxene thermometer for the same sample. The appropriate thermometer to use depends principally on the temperature at which equation (5) closes. The two

thermometers I use to calculate fO_2 provide a reasonable bracket for the actual fO_2 of the sample at closure (e.g. Parkinson and Pearce, 1998).

Mineral chemistry data were obtained using a Cameca SX50 electron microprobe equipped with four wavelength dispersive spectrometers, located at Texas A&M University. Mineral chemistry results from several samples are included in Chapter II, but were used only for thermobarometry calculations. I re-report results from these samples and supplement them with additional analyses. Olivine, spinel, and orthopyroxene were analyzed using a 15 kV accelerating voltage and a 20 nA beam current. Olivine and spinel grains were analyzed with a 1 micron diameter beam, while orthopyroxene grains were analyzed with either a 1 micron or 20 micron diameter beam. Orthopyroxene compositions were estimated by re-integrating clinopyroxene lamellae with the orthopyroxene host following the methods of Chapter II.

Mineral analyses were normalized to cations as follows: Orthopyroxene to four cations, spinel and olivine to three cations. Fe^{3+} versus Fe^{2+} was calculated for pyroxene and spinel based on charge balance, although this method involves significant uncertainty (Canil and O'Neil, 1996; Wood and Virgo, 1989). In particular, random uncertainties preclude the use of conventional probe analyses to determine values of $Fe^{3+}/\Sigma Fe$ in pyroxenes via charge balance (Canil and O'Neill, 1996). However, determining values of $Fe^{3+}/\Sigma Fe$ are not limited by random uncertainties, but by systematic uncertainties in the compositions of standards and/or matrix corrections (Canil and O'Neil, 1996; Wood and Virgo, 1989). I have, therefore, analyzed spinel standards with known $Fe^{3+}/\Sigma Fe$ ratios (provided by B. Wood) during each microprobe

session. The value of $Fe^{3+}/\Sigma Fe$ ratio, as originally determined from charge balance, was then adjusted based on the analyses of these spinel standards by applying the method of Wood and Virgo (1989).

Mineral composition and fO_2 results

Olivine, orthopyroxene, and spinel composition data are listed in Table 6. Olivine grains are compositionally homogeneous within each sample, and show no internal zoning. Olivine forsterite content varies from 0.88 to 0.92 across the massif. Spinel grain morphology varies from highly irregular and interlobate (Fig. 15a), to subhedral (Fig. 15b). Interlobate grains vary from under a millimeter to several millimeters in length, while subhedral grains are typically less than a millimeter. Spinel grains of both morphologies typically show Al-Cr zoning, with rims slightly enriched in Al, but show no Mg-Fe^{2+} zoning. Fe^{3+} is either not zoned or has slight enrichment of Fe^{3+} on the rim. Sample 12RH14a is a good example of a sample with subhedral grain morphology, and is associated with spinel with higher than normal TiO_2 values at 0.26 weight percent (Table 6). Figure 16 plots the forsterite content in olivine relative to the average core Cr# from each sample. Results closely mirror the results of Sano and Kimura (2007) from the northern portion of the massif, with samples from the Plateau complex, plagioclase zone, and Ellis Stream complex typically lying along the margin of the mantle array of Arai (1994). Several samples have olivine forsterite contents lower (more Fe-rich) than is typical of the mantle array, also consistent with the results of Sano and Kimura (2007). A plot of core Cr# vs. Mg# for spinel grains shows samples from the

	Plateau complex - 12RH14a:				Plateau complex - RH12ES13:				Plateau complex - 11ES15:				Plateau complex - 10ES05:			
Phase	Plag Lherzolite opx	ol	sp (core)	sp (rim)	Plag Harzburgite opx	ol	sp (core)	sp (rim)	Plag Lherzolite opx	ol	sp (core)	sp (rim)	Harzburgite opx	ol	sp (core)	sp (rim)
Wt% oxides																
SiO2	55.45	40.74	0.00	0.01	55.21	40.95	0.00	0.00	55.70	40.95	0.01	0.01	56.42	41.36	0.00	0.00
TiO2	0.12		0.26	0.29	0.04		0.08	0.06	0.05		0.09	0.08	0.02		0.05	0.04
Al2O3	2.67	0.01	29.81	31.06	3.22	0.01	35.68	37.00	2.46	0.00	33.07	34.06	2.30	0.00	27.78	28.36
Cr2O3	0.66		36.45	34.30	0.71		31.72	29.90	0.58		33.22	32.32	0.64		39.64	38.69
V2O3			0.28	0.28			0.17	0.18			0.25	0.19			0.18	0.18
Fe2O3																
FeO	6.44	10.21	19.74	19.55	5.98	9.41	17.09	17.16	6.19	9.80	18.68	18.21	5.79	8.87	19.01	19.30
MnO	0.14	0.15	0.61	0.56	0.12	0.13	0.48	0.47	0.14	0.14	0.45	0.44	0.14	0.13	0.19	0.24
MgO	32.84	48.92	12.97	13.38	33.13	49.88	14.97	15.25	33.30	49.60	14.38	14.73	33.44	49.78	13.33	13.41
CaO	1.34	0.02	0.01	0.00	1.24		0.01	0.02	1.07	0.02	0.00	0.03	1.37	0.02	0.01	0.00
NiO	0.08	0.33	0.11	0.08	0.08	0.01	0.15	0.10	0.07	0.40	0.19	0.14	0.10	0.42	0.09	0.14
Na2O	0.02				0.01	0.40			0.02	0.00			0.01	0.01		
Total	99.76	100.38	100.22	99.50	99.74	100.80	100.36	100.14	99.58	100.91	100.34	100.20	100.23	100.58	100.29	100.36
Atomic units																
Si	1.93	1.00	0.00	0.00	1.91	0.99	0.00	0.00	1.93	0.99	0.00	0.00	1.94	1.00	0.00	0.00
AlIV	0.07	0.00	1.05	1.09	0.09	0.00	1.21	1.25	0.07		1.14	1.16	0.06		0.98	1.00
AlVI	0.03	0.00	0.00	0.00	0.04	0.00	0.00	0.00	0.03	0.00			0.04	0.00	0.00	0.00
Ti	0.00	0.00	0.01	0.01	0.00	0.00	0.00	0.00	0.00		0.00	0.00	0.00		0.00	0.00
Cr	0.02	0.00	0.86	0.81	0.02	0.00	0.72	0.68	0.02		0.77	0.74	0.02		0.94	0.91
FeIII	0.02	0.00	0.05	0.06	0.02	0.00	0.04	0.05	0.02		0.07	0.06	0.00		0.05	0.06
FeII	0.17	0.21	0.44	0.42	0.15	0.19	0.37	0.36	0.16	0.20	0.39	0.38	0.17	0.18	0.42	0.42
Mn	0.00	0.00	0.02	0.01	0.00	0.00	0.01	0.01	0.00	0.00	0.01	0.01	0.00	0.00	0.00	0.01
Ni	0.00	0.01	0.00	0.00	0.00	0.01	0.00	0.00	0.00	0.01	0.00	0.00	0.00	0.01	0.00	0.00
Mg	1.70	1.78	0.58	0.59	1.71	1.80	0.64	0.65	1.72	1.80	0.62	0.64	1.72	1.80	0.60	0.60
Ca	0.05	0.00	0.00	0.00	0.05	0.00	0.00	0.00	0.04	0.00	0.00	0.00	0.05	0.00	0.00	0.00
Na	0.00	0.00	0.00	0.00	0.00	0.00	0.00	0.00	0.00		0.00	0.00	0.00	0.00	0.00	0.00
Total	4.00	3.00	3.00	3.00	4.00	3.00	3.00	3.00	4.00	3.00	3.00	3.00	4.00	3.00	3.00	3.00

Table 6 – Electron microprobe mineral composition results.

	Plagioclase zone - RH09_39:				Plagioclase zone - 11ES25:				Plagioclase zone - RH12_23:				Ellis Stream complex - 11ES27:			
Phase	Plag Lherzolite opx	ol	sp (core)	sp (rim)	Plag Harzburgite opx	ol	sp (core)	sp (rim)	Plag Lherzolite opx	ol	sp (core)	sp (rim)	Lherzolite opx	ol	sp (core)	sp (rim)
Wt% oxides																
SiO2	55.50	40.86	0.00	0.01	54.81	41.02	0.08	0.09	55.20	41.10	0.02	0.03	55.71	40.68	0.02	0.01
TiO2	0.04		0.05	0.05	0.06		0.12	0.13	0.12		0.24	0.19	0.03		0.05	0.06
Al2O3	2.86	0.04	40.46	41.78	3.06	0.00	34.29	36.40	2.61	0.01	30.72	30.77	2.52	0.00	33.92	34.84
Cr2O3	0.52		26.98	26.04	0.76		32.98	30.73	0.65		35.04	34.39	0.60		32.93	31.40
V2O3			0.19	0.26			0.26	0.17			0.18	0.24			0.18	0.15
Fe2O3																
FeO	6.44	10.55	16.38	16.40	5.94	9.26	17.45	17.10	6.05	9.21	19.42	20.61	7.09	11.06	18.85	19.41
MnO	0.14	0.15	0.36	0.37	0.14	0.14	0.44	0.41	0.15	0.13	0.51	0.47	0.17	0.17	0.44	0.43
MgO	33.52	49.46	16.17	16.30	32.59	49.55	14.65	15.04	33.31	49.78	13.79	13.61	32.93	48.30	14.21	14.33
CaO	0.78	0.02	0.00	0.01	1.53	0.02	0.01	0.02	1.04	0.01	0.00	0.00	1.17	0.03	0.01	0.03
NiO	0.08		0.18	0.17	0.09		0.15	0.19	0.09	0.40	0.10	0.18	0.08	0.34	0.17	0.18
Na2O	0.01				0.01				0.01	0.00			0.01	0.00		
Total	99.89	101.08	100.76	101.38	98.99	99.98	100.42	100.27	99.23	100.65	100.02	100.49	100.31	100.58	100.78	100.83
Atomic units																
Si	1.92	0.99	0.00	0.00	1.92	1.00	0.00	0.00	1.92	1.00	0.00	0.00	1.93	1.00	0.00	0.00
AlIV	0.08		1.33	1.36	0.08		1.17	1.23	0.08		1.07	1.07	0.07		1.16	1.18
AlVI	0.04	0.00			0.04	0.00	0.00	0.00	0.03	0.00	0.00	0.00	0.03	0.00	0.00	0.00
Ti	0.00		0.00	0.00	0.00		0.00	0.00	0.00		0.01	0.00	0.00		0.00	0.00
Cr	0.01		0.60	0.57	0.02		0.76	0.70	0.02		0.82	0.80	0.02		0.75	0.72
FeIII	0.03		0.04	0.04	0.02		0.05	0.05	0.03		0.08	0.10	0.03		0.07	0.08
FeII	0.16	0.21	0.34	0.34	0.15	0.19	0.37	0.36	0.15	0.19	0.40	0.41	0.18	0.23	0.39	0.39
Mn	0.00	0.00	0.01	0.01	0.00	0.00	0.01	0.01	0.00	0.00	0.01	0.01	0.00	0.00	0.01	0.01
Ni	0.00	0.01	0.00	0.00	0.00	0.01	0.00	0.00	0.00	0.01	0.00	0.00	0.00	0.01	0.00	0.00
Mg	1.73	1.79	0.67	0.67	1.70	1.80	0.63	0.64	1.73	1.80	0.61	0.60	1.70	1.76	0.61	0.62
Ca	0.03	0.00	0.00	0.00	0.06	0.00	0.00	0.00	0.04	0.00	0.00	0.00	0.04	0.00	0.00	0.00
Na	0.00	0.00	0.00	0.00	0.00	0.00	0.00	0.00	0.00	0.00	0.00	0.00	0.00	0.00	0.00	0.00
Total	4.00	3.00	3.00	3.00	4.00	3.00	3.00	3.00	4.00	3.00	3.00	3.00	4.00	3.00	3.00	3.00

Table 6 (continued) – Electron microprobe mineral composition results.

	Ellis Stream complex - 12RH27:				Ellis Stream complex - 12RH26:				Two tarns harzburgite - 11ES19:				Two tarns harzburgite - RH12ES14:			
Phase	Harzburgite opx	ol	sp (core)	sp (rim)	Harzburgite opx	ol	sp (core)	sp (rim)	Harzburgite opx	ol	sp (core)	sp (rim)	Harzburgite opx	ol	sp (core)	sp (rim)
Wt% oxides																
SiO2	55.74	40.98	0.00	0.00	56.61	41.02	0.00	0.00	56.31	41.07	0.00	0.00	55.14	41.28	0.02	0.01
TiO2	0.03		0.07	0.06	0.04		0.15	0.13	0.03		0.08	0.09	0.03		0.03	0.04
Al2O3	3.08	0.00	34.40	34.88	1.55	0.00	20.87	21.37	2.39	0.00	26.04	26.69	4.09	0.00	42.66	43.57
Cr2O3	0.69		32.76	31.33	0.46		45.61	44.25	0.79		41.67	40.86	0.84		25.81	25.50
V2O3			0.20	0.15			0.16	0.24			0.20	0.22			0.17	0.14
Fe2O3																
FeO	6.18	9.81	18.01	19.18	5.35	8.32	20.48	21.35	5.63	9.06	18.68	18.54	5.76	9.18	14.70	14.29
MnO	0.15	0.14	0.45	0.47	0.13	0.13	0.69	0.61	0.14	0.13	0.22	0.27	0.14	0.13	0.15	0.13
MgO	32.90	50.05	14.61	14.31	34.39	50.49	12.21	12.02	32.84	49.81	13.36	13.31	32.16	49.47	16.90	17.24
CaO	1.22	0.01	0.00	0.01	0.72	0.05	0.01	0.03	2.18	0.03	0.00	0.01	1.83	0.03	0.00	0.01
NiO	0.10	0.68	0.15	0.09	0.07	0.40	0.07	0.16	0.10	0.39	0.10	0.07	0.10	0.41	0.22	0.26
Na2O	0.02				0.01	0.00			0.02	0.00			0.01	0.01		
Total	100.10	101.68	100.64	100.46	99.32	100.40	100.24	100.16	100.42	100.48	100.36	100.05	100.10	100.53	100.65	101.18
Atomic units																
Si	1.93	0.99	0.00	0.00	1.96	0.99	0.00	0.00	1.94	1.00	0.00	0.00	1.91	1.01	0.00	0.00
AlIV	0.07		1.17	1.19	0.04		0.76	0.78	0.06		0.93	0.95	0.09		1.39	1.41
AlVI	0.05	0.00			0.02	0.00	0.00	0.00	0.04	0.00	0.00	0.00	0.07	0.00	0.00	0.00
Ti	0.00		0.00	0.00	0.00		0.00	0.00	0.00		0.00	0.00	0.00		0.00	0.00
Cr	0.02		0.75	0.72	0.01		1.12	1.09	0.02		0.99	0.97	0.02		0.56	0.55
FeIII	0.00		0.05	0.06	0.00		0.09	0.11	0.00		0.05	0.05	-0.01		0.02	0.02
FeII	0.18	0.20	0.39	0.40	0.15	0.17	0.44	0.45	0.16	0.18	0.42	0.42	0.17	0.19	0.32	0.31
Mn	0.00	0.00	0.01	0.01	0.00	0.00	0.02	0.02	0.00	0.00	0.01	0.01	0.00	0.00	0.00	0.00
Ni	0.00	0.01	0.00	0.00	0.00	0.01	0.00	0.00	0.00	0.01	0.00	0.00	0.00	0.01	0.00	0.01
Mg	1.70	1.80	0.63	0.62	1.78	1.83	0.56	0.56	1.69	1.81	0.60	0.60	1.66	1.80	0.70	0.70
Ca	0.05	0.00	0.00	0.00	0.03	0.00	0.00	0.00	0.08	0.00	0.00	0.00	0.07	0.00	0.00	0.00
Na	0.00		0.00	0.00	0.00	0.00	0.00	0.00	0.00	0.00	0.00	0.00	0.00	0.00	0.00	0.00
Total	4.00	3.00	3.00	3.00	4.00	3.00	3.00	3.00	4.00	3.00	3.00	3.00	4.00	3.00	3.00	3.00

Table 6 (continued) – Electron microprobe mineral composition results.

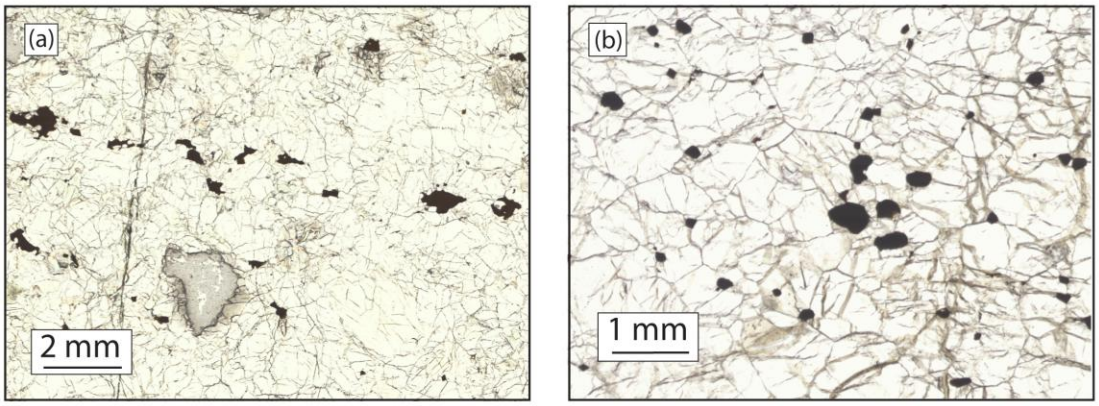

Figure 15 – Spinel morphology, plane polarized light. (a) Spinel with highly irregular, interlobate grain boundaries. (b) Subhedral grain boundaries.

Red Hills typically have lower Mg# than samples from an abyssal peridotite population, for a given Cr# (Fig. 17). Figure 18 plots spinel Cr# versus spinel TiO_2 weight percent. I include the extensive spinel data set from Sano and Kimura (2007). In general, spinels in harzburgites and dunites from the two tarns harzburgite are extremely depleted in TiO_2 (Figure 18a), while spinels in plagioclase-bearing peridotites from the Plateau complex, plagioclase zone, and Ellis Stream complex have variable, but typically higher TiO_2 values (Figure 18b). Spinel in non-plagioclase-bearing harzburgite and dunite from the Plateau complex, plagioclase zone, and Ellis Stream complex also have generally higher TiO_2 than harzburgite and dunite from the two tarns harzburgite (Figure 18c).

Temperature based on the compositions of co-existing olivine and spinel was estimated using the Fabries (1979) and Ballhaus et al. (1991) thermometers. These temperatures are low relative to those estimated using pyroxene thermometers, with values typically falling between 700 and 800°C (Table 7). Oxygen fugacity results for both spinel cores and spinel rims are calculated using the Ballhaus and Nell-Wood

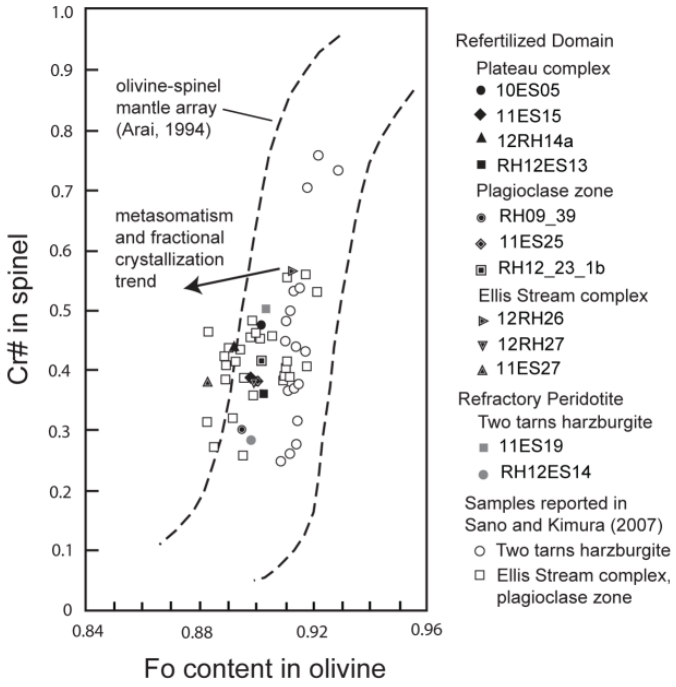

Figure 16 – Cr# in spinel versus forsterite content in olivine. Also plotted are samples from Sano and Kimura (2007), re-plotted using the map units described in Chapter II. The mantle array is from Arai (1994).

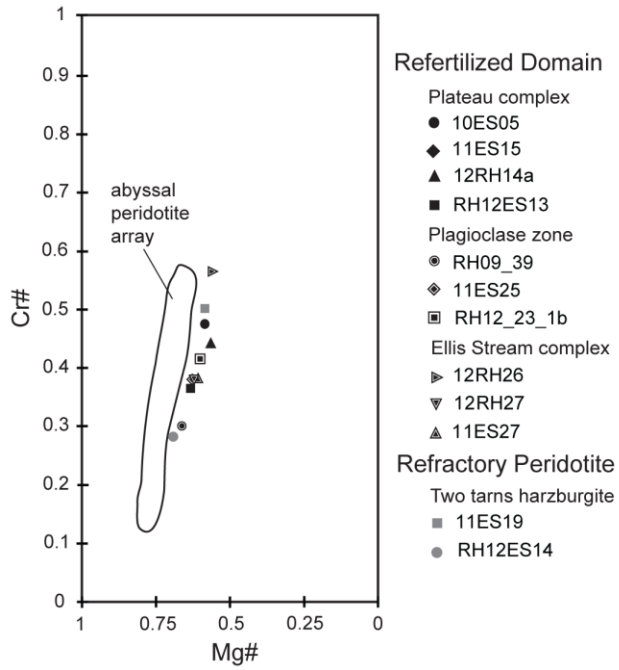

Figure 17 – Cr# in spinel versus Mg# in spinel. Samples are plotted relative to the abyssal peridotite array of Dick and Bullen (1984).

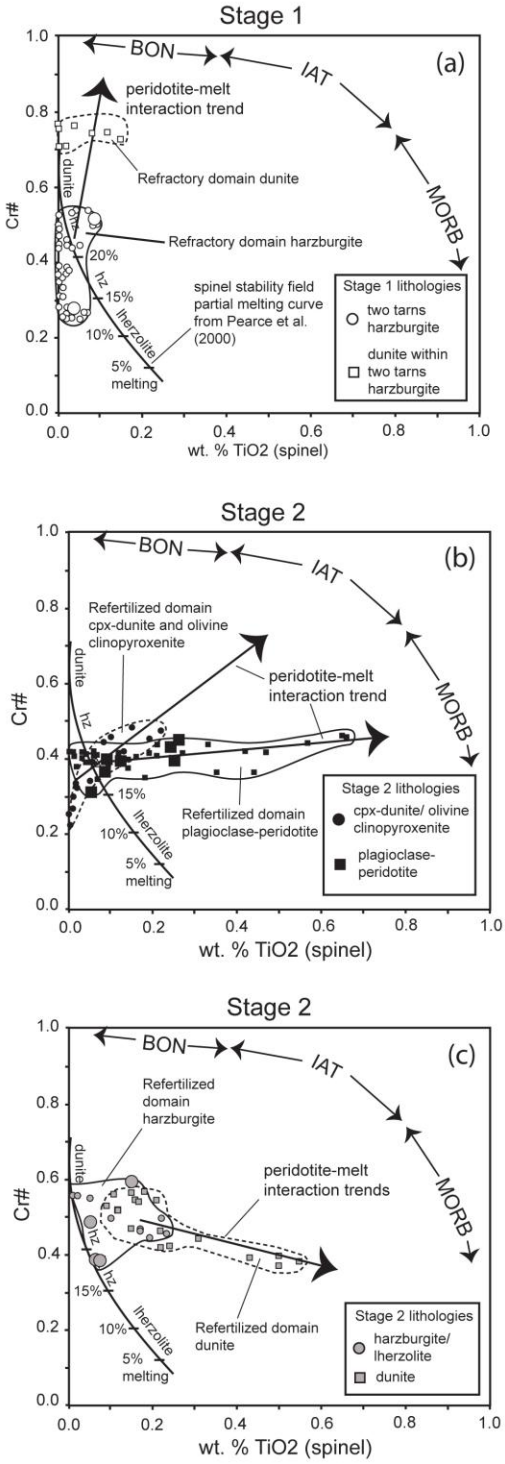

Figure 18 – Cr# in spinel versus TiO_2 weight percent in spinel. Figure modified from Pearce et al. (2000). Samples are divided into lithologies within the refractory and refertilized domains. Large symbols are results from this chapter, small symbols are from Sano and Kimura (2007).

methods and are listed on Table 7. Results using the Ballhaus method are plotted on Figure 19. Spinel cores show a general positive correlation between Cr# and fO_2 for all samples from the Red Hills, regardless of lithologic unit. Core fO_2 values vary from -1.49 to +0.63 relative to the FMQ buffer - a range of slightly more than 2 log units. Spinel rims show a similar trend, with a slightly higher range of values. With the exception of sample RH12ES14 from the two tarns harzburgite, most rims have similar to slightly higher fO_2 values relative to their cores (Table 7).

I tested the robustness of the fO_2 calculations by considering the possibility of Mg-Fe^{2+} resetting in spinel during cooling. Some resetting is likely, as spinel grains commonly have rims enriched in aluminum, but do not show Mg-Fe^{2+} zoning. Olivine-spinel thermometry (Fabries, 1979; Ballhaus et al., 1991) also yields temperatures approximately 100°C to 200°C lower when compared to two-pyroxene temperatures (Table 7). Following the methods outlined in Woodland et al. (1996), I compensated for possible resetting in spinel by adjusting the Mg-Fe^{2+} ratio in spinel until the Fabries (1979) thermometer yielded temperatures equivalent to Taylor (1998) two-pyroxene temperatures (Table 7, Chapter II). I fixed the composition of olivine, assuming its large modal percent precludes significant modification, and I also fixed the values of the trivalent cations (Al, Cr, Fe^{3+}) in spinel. This back-calculated spinel composition yielded logfO_2 (ΔFMQ) values that were typically around 0.1 log units more reduced than those calculated using measured spinel compositions. Such a nominal change indicates possible late-stage, Mg-Fe^{2+} resetting did not significantly alter the computed fO_2 in our samples.

Rock type	Map unit	Sample	Cr# core	Cr# rim	Fe^{3+}/Σ Fe sp core	Fe^{3+}/Σ Fe sp rim	T(°C) B91 sp core	T(°C) F79 sp core	T(°C) B91 sp rim	T(°C) F79 sp rim	T(°C) T98*	T(°C) BK90	logfO_2 (ΔFMQ) sp core$^{\$}$	logfO_2 (ΔFMQ) sp rim$^{\$}$	logfO_2 (ΔFMQ) sp core$^{\#}$	logfO_2 (ΔFMQ) sp rim$^{\#}$
Plag Lherz	Plateau complex	12RH14a	0.45	0.43	0.10	0.13	700	750	720	757	990‡	1080‡	-0.86	-0.44	-0.45	-0.03
Plag Harz	Plateau complex	RH12ES13	0.37	0.35	0.10	0.12	700	740	700	745	980‡	1050‡	-1.00	-0.58	-0.57	-0.14
Plag Lherz	Plateau complex	11ES15	0.40	0.39	0.14	0.15	730	770	730	777	940‡	1010‡	-0.16	-0.19	0.13	0.10
Harz	Plateau complex	10ES05	0.49	0.48	0.11	0.13	700	750	700	750	950‡	1080‡	-0.12	0.22	-0.23	0.13
Plag Lherz	Plagioclase zone	RH09_39	0.31	0.30	0.11	0.09	740	780	720	759	970‡	920‡	-1.16	-1.37	-0.59	-0.77
Plag Harz	Plagioclase zone	11ES25	0.39	0.36	0.11	0.11	710	750	700	741	910‡	1120‡	-0.56	-0.55	-0.28	-0.24
Plag Lherz	Plagioclase zone	RH1223	0.43	0.43	0.17	0.19	720	760	710	751	970‡	1000‡	0.11	0.45	0.52	0.91
Lherz	Ellis stream complex	11ES27	0.39	0.38	0.15	0.17	770	810	760	811	980‡	1040‡	-0.56	-0.23	-0.11	0.25
Harz	Ellis stream complex	12RH27	0.39	0.38	0.11	0.14	710	750	680	730		1050	-0.52	0.03	-0.39	0.22
Harz	Ellis stream complex	12RH26	0.60	0.58	0.17	0.19	730	780	720	771		900	0.76	1.06	0.63	0.98
Harz	Two tarns harzburgite	11ES19	0.52	0.51	0.11	0.10	740	780	730	768	890‡	1240‡	-0.31	-0.48	-0.40	-0.56
Harz	Two tarns harzburgite	RH12ES14	0.29	0.28	0.06	0.05	700	740	710	742	910‡	1190‡	-1.38	-1.84	-1.49	-1.96

Table 7 – Geothermometry and fO_2 results. Two tarns harzburgite samples calculated at 6 kbar pressure, all others at 5 kbar pressure. B91 is the Ballhaus et al. (1991) olivine-spinel thermometer, F79 is the Fabries (1979) olivine-spinel thermometer, T98 is the Taylor (1998) two-pyroxene thermometer, and BK90 is the Brey and Kohler (1990) Ca-in-opx thermometer as modified by Nimis and Gruter (2010). $^{\$}$ logfO_2 relative to the FMQ buffer calculated with the Nell-Wood method and the Taylor (1998) two-pyroxene temperature. Where no Taylor (1998) temperature calculated, I use the Brey and Kohler (1990) Ca-in-opx thermometer. $^{\#}$ logfO_2 relative to the FMQ buffer calculated with the Ballhaus method and the Ballhaus (1991) olivine-spinel thermometer. ‡ Values reported in Chapter II.

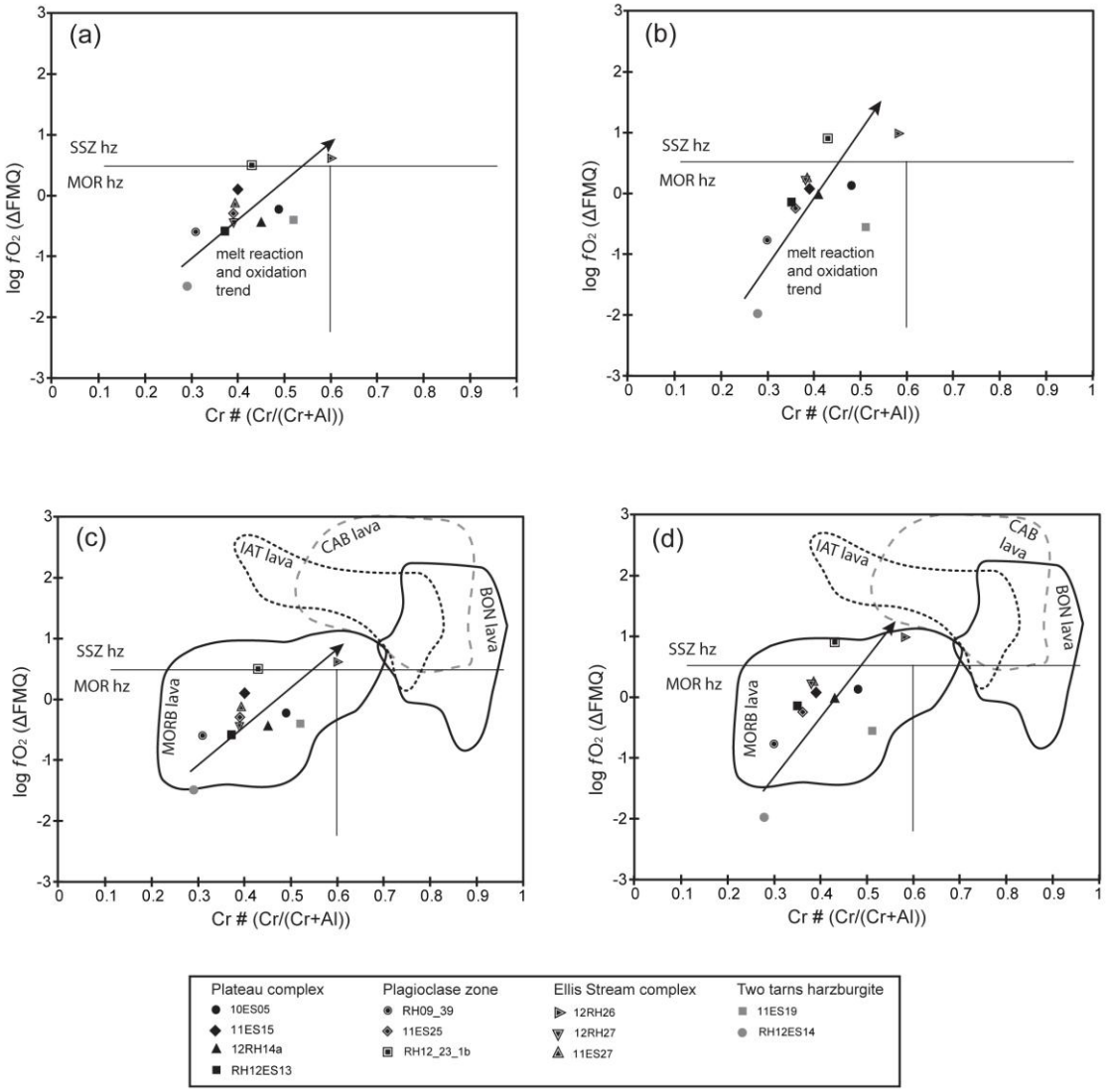

Figure 19 – Cr# in spinel versus oxygen fugacity. a.) Calculated using spinel cores. fO_2 calculated using the Ballhaus method with the Ballhaus (1991) olivine-spinel thermometer. Supra-subduction zone (SSZ) and mid-ocean ridge (MOR) fields for harzburgite defined by Dare et al. (2009). b.) Spinel rims relative to SSZ and MOR fields. Values calculated as in a.). c.) Spinel core and d.) spinel rim values compared to lava fields defined by Dare et al. (2009) for mid-ocean ridge basalt (MORB), island arc tholeiite (IAT), calc-alkaline basalt (CAB), and boninite (BON).

DISCUSSION

Based on geochemical trends and petrologic overprinting relations, I divide the petrologic history of the massif into two stages: 1) Early, melting across the entire massif

that produced the refractory two tarns harzburgite (Stage 1); 2) Later focused melt ascent that both reacted with harzburgite to produce dunite bands and locally refertilized the western massif (Stage 2). I use the term refertilization to refer to the bulk addition of CaO and Al_2O_3 into the rock due to crystallization of either clinopyroxene or plagioclase. Evidence for focused melt migration and local refertilization includes the creation of dunite bands, dunite bands with interstitial clinopyroxene and/or plagioclase, and plagioclase lherzolite. An assumption of this model is that the entire RHUM had the composition of the two tarns harzburgite after it was affected by Stage 1 melting. This is supported by the observation that plagioclase-peridotites in the northern plagioclase zone are found in relatively restricted zones, and much of the unit resembles the two tarns harzburgite. Hence it is likely that Stage 2 melts progressively overprinted peridotites in the western massif, and the western massif was once similar to the two tarns harzburgite. The timing of Stages 1 and 2 described here are identical to the first two stages of deformation described in Chapter II. In this Chapter, however, I focus on the petrologic and geochemical effects of melting and refertilization rather than the deformation history.

Stage 1: Changes in fO_2 and modal composition due to melting

Early melting in the massif produced the refractory two tarns harzburgite, characterized by a relatively small range of modal compositions (Fig. 19a) and small ranges in major element chemistry (dashed lines in Fig. 12a-e). Evidence for melting includes the refractory whole rock chemistry of the two tarns harzburgite (high whole

rock MgO weight %, low Al_2O_3 and CaO weight %), as well as clinopyroxene with extreme depletion in LREE (Sano and Kimura, 2007). Stage 1 melting includes an early period of melting in the garnet stability field, and later melting in the spinel stability field (e.g. Sano and Kimura, 2007).

Despite the relatively narrow range in whole rock composition, the linear relationship between Cr# and fO_2 in Figure 19 suggests Stage 1 melting may have been more complicated, and occurred diachronously at two different oxidation states. The correlation between increasing fO_2 and increasing Cr# throughout both the refertilized and refractory domains suggests that increased levels of melt depletion (resulting in higher Cr#) in a relatively oxidized setting progressively reset and increased fO_2 values. Progressive alteration and the development of positive linear trends of Cr# relative to fO_2 occurs when spinels progressively react to approach equilibrium with migrating melts, which in this case, likely had elevated fO_2. Importantly, this implies that all peridotites initially had low fO_2 and low Cr#, likely in the vicinity of sample RH12ES14 on Figure 19a. However, the original range in fO_2 and Cr# prior to the development of the linear trend is ultimately unknown.

I tentatively sub-divide Stage 1 into two parts: Stage 1a and Stage 1b. Stage 1a reflects early melting to produce a harzburgite with $\log fO_2(\Delta FMQ)$ of approximately -1.5 or lower (i.e. that of RH12ES14). This may correlate to early garnet stability field melting proposed by Sano and Kimura (2007). Stage 1b reflects later melting in a more oxidized setting, and is responsible for the linear relationship between fO_2 and Cr#. This later melting may correlate to the spinel stability field melting proposed by Sano and

Kimura (2007). Additional depletion, as described below, produced dunite bands during Stage 2. Thus, an unknown amount of Stage 2 depletion and/or refertilization may have also contributed to the overall positive linear trend in Figure 19a. I note, however, that Stage 2 is characterized by focused and channelized melt flow (dunite bands), and no dunites were analyzed, so the bulk of the linear trend may represent Stage 1. Some modification of spinel composition clearly occurred during Stage 2 (compare Fig. 18a to b, c), and resulted in an increase in the TiO_2 concentration in many Stage 2 spinels, especially in plagioclase-bearing peridotites (Fig. 18b). However, the slope of increasing TiO_2 values is shallow, particularly for plagioclase-peridotites (Fig. 18b), so despite increasing amounts of TiO_2 in Stage 2 spinels, Cr# did not change significantly. If fO_2 is indeed a function of Cr# as Figure 19 suggests, then it is likely the fO_2 primarily reflects Stage 1 melting and not later Stage 2 metasomatism. One possibility is that some of the scatter in Figure 19a and b may reflect minor increase in fO_2 at constant Cr# (particularly near Cr# 0.4), resulting from Stage 2 metasomatism.

Stage 2: Channelized melt transport in the plagioclase stability field

The plagioclase zone and Plateau and Ellis Stream complexes are thought to represent mantle peridotite metasomatized in the plagioclase stability field from reactive melt transport (e.g. Sano and Kimura, 2007; Kimura and Sano, 2012) at approximately 1000°C and 5 kbar (Webber et al., 2008; Chapter II). I classify those map units as part of Stage 2 depletion and refertilization. The timing of dunite band creation in the Plateau and Ellis Stream complexes relative to plagioclase infiltration is debated (Sano and

Kimura, 2007; Kimura and Sano, 2012; Chapter II). Therefore, in this section I first interpret the timing of dunite band creation. I link the creation of dunite bands in the Plateau and Ellis Stream complexes to the same melt migration event as refertilization in the plagioclase stability field. Then I describe the geochemical effects of Stage 2 melt migration.

Timing of dunite band creation in the refertilized domain

Dunite bands in the Plateau and Ellis Stream complexes likely formed from the same melt migration event as Stage 2 clinopyroxene and plagioclase refertilization. The dunite bands are likely the result of channelized melt that was saturated in olivine but undersaturated in both pyroxenes (e.g., Kelemen et al., 1995). However, a sub-set of dunite bands also show evidence of refertilization reactions resulting in the crystallization of clinopyroxene (Fig. 10c, h), and less commonly plagioclase. A continuum exists between diffuse, large clinopyroxene grains within dunite bands (Fig. 10c, h) to continuous clinopyroxenite bands (Fig. 10d). As a result, clinopyroxenite and olivine websterite bands throughout the massif (Fig. 10d, e) are interpreted to be the fossil remnants of focused melt flow at clinopyroxene saturation, and to form from the coalescence of growing, interstitial clinopyroxene (see right side of figure 10h for interstitial clinopyroxene nearly coalesced into a band). Largely because many melt channels in the Plateau and Ellis Stream complexes contain a history of melting (dunite) and refertilization (clinopyroxene and/or plagioclase in dunite), I link the melt migration episode that created dunite bands to the same melt migration episode that lead to refertilization. I further note that bulk dunite band orientations closely parallel adjacent

plagioclase foliations, suggesting dynamic conditions were similar during both the creation of dunite bands and plagioclase infiltration (Chapter II). Thus I conclude both occurred during the same melt migration event, and post-dated the development of the two tarns harzburgite (i.e. Stage 1).

Figure 18a and c provide additional evidence indicating dunite bands in the Plateau and Ellis Stream complex developed during Stage 2. Spinels from Stage 1 dunite bands (Fig. 18a) are characterized by very high Cr#, and low TiO_2. Spinel in Stage 2 dunite bands are characterized by much lower Cr# and a wide range of TiO_2 (Figure 18c). More importantly, spinels in Stage 2 dunites have an interaction trend that does not intersect the composition of spinels from the Stage 1 dunite bands (Figure 18c). An interaction trend illustrates the progressive changes in TiO_2 relative to Cr# for any melt reaction or melt impregnation event (e.g. Pearce et al., 2000), thus the spinels with the lowest TiO_2 values provide a glimpse of the composition of Stage 2 spinel that were altered the least. As a result, it is apparent that the Stage 2 dunite bands developed from progressive melting or reaction with Stage 1 harzburgite.

Petrologic effects of Stage 2 melt ascent: Mineralogy and whole-rock major elements

The petrologic effects of Stage 2 melt migration in the Plateau complex and plagioclase zone can be easily seen in modal composition space (Figure 11b, c). Samples from the Plateau complex are characterized by two divergent trends from an assumed original composition approximated by the two tarns harzburgite (see arrows on ternary plot of Fig. 11b). The Plateau complex contains harzburgite, dunite, and sporadic lherzolite. The dunite likely formed from focused or channelized melt transport, causing

the peritectic dissolution of orthopyroxene and crystallization of olivine (e.g. Keleman et al., 1995). Lherzolite, often found in conjunction with plagioclase, likely formed from percolative fractional crystallization of clinopyroxene (± plagioclase and olivine). The plagioclase zone differs from the Plateau complex in that plagioclase is far more common, and dunite bands are rare. The plagioclase zone contains both plagioclase lherzolite and plagioclase harzburgite (Fig. 10e, f). Plagioclase lherzolites likely formed from crystallization of both plagioclase and clinopyroxene (± olivine, ± orthopyroxene) from an interstitial basaltic melt ascending within a harzburgite protolith resembling the two tarns harzburgite (see arrows on Fig. 11c). Plagioclase harzburgites also have higher average clinopyroxene values when compared to the two tarns harzburgite (Fig. 11c), and so likely also crystallized out minor clinopyroxene.

Whole-rock major element geochemistry also shows the geochemical effects of Stage 2 melt migration. Stage 2 units show both melting trends and refertilization trends moving in opposite directions away from the compositional range of the two tarns harzburgite, resulting in significantly more geochemical heterogeneity in Stage 2 units. Melting of refractory harzburgite, which produced the dunite bands in the Plateau complex, resulted in decreased values of CaO (Fig. 12a, b, d, e), Al_2O_3 (Fig. 12b), HREE (Fig. 12e), and SiO_2 (Fig. 12a, c), but increased the percentage of MgO (Fig. 12c, d). Refertilization from percolative fractional crystallization of clinopyroxene ± plagioclase (Plateau complex) and clinopyroxene and plagioclase (plagioclase zone) from ascending Stage 2 melt changed the major element composition of the Stage 1 refractory harzburgites, resulting in increased values of CaO (Fig. 12a, b, d, e) Al_2O_3 (Fig. 12b),

and HREE (Fig. 12e). I attribute the scatter in the samples with relatively high CaO (Fig. 12a, b, d, and e) to result from different percentages of modal addition of clinopyroxene and plagioclase.

Petrologic effects of Stage 2 melt ascent: Whole-rock trace elements

The effects of melt-reaction and refertilization on whole rock trace element abundances are more complicated. Across the massif, HREE (e.g., Yb) show a strong positive relationship to CaO (Fig. 12e), likely reflecting the amount of clinopyroxene in host samples. Within individual units, harzburgite samples from the two tarns harzburgite generally have lower heavy and middle rare earth element abundances compared to harzburgite and lherzolite samples from the plagioclase zone and Plateau complex. LREE values show significant differences compared to HREE. Across the massif, there is no correlation between LREE (i.e. Ce) and CaO (Fig. 12f). In the refractory two tarns harzburgite, LREE values are similar to harzburgite and lherzolite samples from the plagioclase zone and Plateau complex (Fig. 13), despite having much lower middle and somewhat lower heavy rare earth element values. Enrichment in LREE in refractory peridotites, such as the two tarns harzburgite, is typically thought to be the result of chromatographic effects from very small melt fractions that are extremely enriched in LREE reacting with a depleted host rock (Navon and Stolper, 1987; Ozawa and Shimizu, 1995; Vernieres et al., 1997). Extreme LREE enrichment can occur during a metasomatising episode from melts derived from much greater depths, or in situ during the melting episode itself from reaction between host rock and small amounts of trapped melt (i.e. Ozawa and Shimizu, 1995). The more subdued LREE enrichment seen in the

harzburgite and lherzolite samples from the Plateau complex and plagioclase zone (Fig. 13), as well as higher overall middle rare earth values, may reflect larger time-integrated melt fractions and closer equilibrium with migrating melts. As a result of likely differences in the time-integrated melt fractions, LREE values are decoupled from clinopyroxene and CaO abundance in the samples.

Petrologic effects of Stage 2 melt ascent: Crypto-crystalline metasomatism

Crypto-crystalline metasomatism, or changes in mineral composition, is also widespread in the massif. A change is observed in the relative depletion of the forsterite component in olivine relative to spinel Cr# (Fig. 16). Arai (1994) notes that this trend is typical of peridotites experiencing metasomatism and fractional crystallization. Sano and Kimura (2007) also interpreted this trend in samples from the northern Red Hills massif to be the result of metasomatism. I interpret the aluminum-rich rims in spinel grains and enrichment in the fayalite component of olivine as most consistent with the metasomatizing agent being a melt. It is not consistent with late-stage Fe^{2+}-Mg exchange between olivine and spinel, as this exchange would result in a lower fayalite component in olivine, as opposed to the higher fayalite component that is observed. Metasomatism resulting in Fe enrichment was reported at Lherz (Bodinier et al., 1990; Woodland et al., 1996), and is a likely scenario for the Red Hills.

Petrologic zonation from Stage 2 melt ascent

The plagioclase zone is discontinuously located along the periphery of the Plateau complex. This indicates the Plateau complex-plagioclase zone is a petrologically zoned sequence that developed from Stage 2 melt ascent. Saturation in both

clinopyroxene and plagioclase (and presumably olivine) during melt ascent within the plagioclase zone may indicate melt along the periphery of the Stage 2 melt system became trapped and slowly cooled and crystallized. The lack of dunite bands in the plagioclase zone suggests lower melt fluxes along the periphery, which would encourage melt stagnation.

To summarize, the modal mineralogy and bulk rock chemistry of the refertilized western RHUM changed considerably due to Stage 2 focused melting and percolative fractional crystallization of ascending melt within an upper mantle melt transport network. I describe a melt transport system (Stage 2), located entirely within the mantle, that both depleted and enriched the geochemistry and petrology of the host peridotite. The abundance of dunite bands in the interior suggests higher melt fluxes in the interior than the periphery, which may have led to melt stagnation on the periphery and the development of a compositionally zoned peridotite body (plagioclase-rich periphery, banded dunite-harzburgite interior). Stage 2 melt migration described here may reflect the conversion of a lithologically homogeneous depleted mantle asthenosphere (i.e. refractory two tarns harzburgite, Stage 1) into a compositionally zoned and geochemically heterogeneous mantle lithosphere.

Tectonic setting for the development of the Red Hills peridotite

Several lines of evidence suggest a polygenetic tectonic melting history in the Red Hills, perhaps beginning in a mid-ocean ridge environment and ending in supra-subduction zone environment. I describe the evidence for the tectonic setting of each

stage in the development of the Red Hills massif. Additionally, I use our new mapping to integrate the new melting and refertilization model presented here with the extensive geochemical data sets presented by Sano and Kimura (2007).

Stage 1a: Initiation of melting in a mid-ocean ridge environment

The earliest episode of melting, labeled Stage 1a, is the most difficult to characterize and subject to the most uncertainty. It may have occurred under relatively reducing conditions of around logfO_2(ΔFMQ) of approximately -1.5 or lower based on the lowest fO_2 value in Figure 19. These relatively low fO_2 values are most consistent with melting in a mid-ocean ridge environment, and may correspond to the early episode of garnet stability field melting determined through clinopyroxene rare earth element modeling (Sano and Kimura, 2007).

Stage 1b: Continued melting in a supra-subduction zone environment

Continued melting during Stage 1b likely occurred under more oxidizing conditions, likely in a supra-subduction zone environment. Melting progressively reset spinel compositions to higher fO_2 and higher Cr#, presumably approaching equilibrium with the reacting melt. The slope of the linear trend in Figure 19a and b and the location of the most oxidized samples provide constraints on the composition of the reacting melt. Though harzburgite fO_2 typically falls within the range expected for mid-ocean ridge harzburgite (Fig. 19a, b), the upper bound for fO_2 from spinel cores of the two most oxidized samples marginally exceed the mid-ocean ridge peridotite range, and their corresponding rims are well within the field of supra-subduction zone harzburgites. Figure 19c and d compare samples from the Red Hills to the fO_2 vs. Cr# fields for mid-

ocean ridge basalt (MORB) lavas, island arc tholeiite (IAT) lavas, calc-alkaline basalt (CAB) lavas, and boninite (BON) lavas (fields from Dare et al., 2009). Each lava field represents a possible range in fO_2 and Cr# for the reacting end-member for Red Hills peridotites. The arrows in the plot estimate the oxidation reaction trend for Red Hills peridotites during progressive reaction, as the peridotite composition moved towards equilibrium with the melt. The arrows point in the direction of reasonable melt compositions that could produce the linear array of data points. The realm of conceivable reacting end-member melts does not completely exclude peridotite reaction with MORB-type melts, but would require reaction with a MORB-type compositional extreme with very high fO_2. However, IAT, and CAB-type magmas could easily produce both the core and rim values observed in the Red Hills. This combined with the harzburgite rims that exceed fO_2 values typical of mid-ocean ridge harzburgites, suggests Stage 1b melting occurred in a supra-subduction zone environment, but this interpretation is not conclusive.

Additionally, whole-rock incompatible element plots from the Stage 1 two tarns harzburgite show highly incompatible element enrichment (Fig. 14) but systematic negative Nb anomalies. This suggests a metasomatizing agent, relatively depleted in Nb relative to other incompatible elements, reacted and enriched the peridotite. Nb, as well as other high field strength elements such as Zr and Hf, are known to be less water soluable than similarly incompatible elements, such as La and Th. Thus, negative Nb anomalies in primitive mantle normalized plots (Fig. 14) suggest H_2O-bearing fluids/melts were responsible for the overall incompatible element enrichment. In this

case, late-stage hydrous alteration is unlikely to be responsible for the Nb anomalies due to: 1) The abundance of fresh unaltered peridotites with few hydrous phases present; 2) The lack of correspondence between La/Nb ratios and loss on ignitions values (Fig. 12g). I tentatively interpret water-rich melts, typical of subduction zones, as the likely source of the Nb anomalies, acknowledging the uncertainty in the measurements.

The structural geology of the two tarns harzburgite also helps constrain its tectonic setting. The unit is characterized by a highly constrictional, or linear fabric. Foliations are poorly developed, and variably oriented while lineations are consistent across the unit. It has been interpreted as an L-tectonite that formed under homogeneous strain conditions during melting (see Chapter II). This is important because L-tectonites are difficult to create during homogeneous, steady-state strain, in part because fabric geometry is a function of not only the three-dimensional boundary conditions of deformation but also of finite strain (Fossen and Tikoff, 1993; Fossen and Tikoff, 1998; Teyssier and Tikoff, 1999; Dewey, 2002). Most three-dimensional boundary conditions capable of producing pure L-tectonites require highly oblique transtension under monoclinic symmetry conditions (i.e. where simple shearing is dominant and is parallel to one of the principal coaxial stretch directions). Highly oblique transtension is a reasonable setting for subduction zones, especially during their initiation, because many subduction zones initiate along former oceanic transform faults (e.g. Casey and Dewey, 1984; Stern and Bloomer, 1992; Choi et al., 2008; Stern et al., 2012). Mid-ocean ridges do not have dominant strike-slip components of motion along the ridge axis, and thus are not able to produce L-tectonites. Only along mid-ocean ridge transform faults does

strike-slip motion dominate. Isolated zones of highly oblique transtension could occur at releasing bends along these structures, but such zones are not likely to be common, and the preservation potential of such structures is low compared to widespread highly oblique transtension that is likely produced during the early stages of subduction.

Finally, Figure 18, which is largely based on data from Sano and Kimura (2007), provides additional evidence suggesting a supra-subduction zone environment for Stage 1. Figure 18 is divided into three plots, and I address the tectonic significance of Stage 1 spinels here. Following the approach of Pearce et al. (2000), Figure 18a shows spinel Cr# plotted against spinel TiO_2 weight percent. Harzburgites have very low values of TiO_2, typically less than predicted for progressive melting in the spinel stability field alone (Figure 18a). This provides additional evidence for prior melting in the garnet stability field (Stage 1a), consistent with the work of Sano and Kimura (2007). Dunites are uncommon in the two tarns harzburgite, but do occur locally. Dunites have considerably higher Cr# relative to harzburgites, and show a peridotite-melt interaction trend heading in the direction of boninite-type melts. Such trends result from relatively TiO_2 enriched melts interacting with extremely TiO_2 depleted peridotities. Boninites, sourced from extremely depleted peridotites, have the lowest TiO_2 values while MORB-type melts have higher TiO_2 values. As interaction increases, the spinel composition in the peridotites begins to approach equilibrium with the melt. Thus the direction of the interaction trend provides evidence for the composition of the interacting melt. Interaction could involve either melt-rock reactions or melt impregnation (e.g. Pearce et al., 2000), but either way the trend of the peridotite-melt interaction in Figure 18a for

Stage 1 melts suggest the interacting melt was extremely depleted in TiO_2, consistent with a boninitic-type, subduction zone melt.

Stage 2: Focused melt ascent in a supra-subduction zone environment

Several lines of evidence also suggest Stage 2 occurred in a supra-subduction zone environment. First, plagioclase is all three Stage 2 units (plagioclase zone, Plateau complex, Ellis Stream complex) is highly anorthitic. In Chapter II, anorthtite percentages of between 89% and 96% are reported, with most around 94%. Such high anorthite values are typical of hydrated melts in subduction zone settings, which have been found to dramatically increase anorthite values in plagioclase feldspars (Sisson and Grove, 1993; Koepke et al., 2004; Feig et al., 2006).

Second, two-pyroxene temperatures from all three Stage 2 units suggest equilibration at around 1000°C (Chapter II). These pyroxenes contain melt microstructures. If the 2-pyroxene temperatures reflect equilibration with melt, such temperatures are incompatible with a MORB-type, anhydrous melt at low pressure, but are compatible with low pressure, hydrous melts from subduction zone settings (Kushiro et al., 1968; Green, 1972; Mysen, 1973).

Third, the broad petrologic zoning in Stage 2 units implies early crystallization of clinopyroxene in the interior and later crystallization of plagioclase on the periphery. A fractional crystallization sequence of olivine→clinopyroxene→plagioclase is typical of hydrous melts in subduction zone settings, but is different from the typical MORB fractional crystallization sequence of olivine→plagioclase→clinopyroxene (e.g. Shervais, 2000). The Plateau complex, an interior Stage 2 unit, is dominated by the

addition of clinopyroxene (Fig. 10c, d, 11b) rather than plagioclase, though both occur. The plagioclase zone occurs along the margin of the Plateau complex (Fig. 9b), and is characterized by both clinopyroxene and plagioclase addition (Fig. 10e, f). The marginal zones of migrating melts (i.e. plagioclase zone) will likely have either lower melt fluxes, encouraging stagnation, or potentially lower temperatures if the contact represents a thermal boundary layer. Either will encourage higher amounts of fractional crystallization within migrating melt, potentially leading to multiple phases reaching saturation, and explain the abundance of plagioclase along the periphery of Stage 2 units.

I further note that spinels from Stage 2 units show interesting trends that support early crystallization of clinopyroxene and later crystallization of plagioclase. Figure 18b, also derived largely from Sano and Kimura (2007), shows two different trends for clinopyroxene-dunites/olivine clinopyroxenites, and plagioclase-bearing peridotites. Spinels from clinopyroxene-dunites/olivine clinopyroxenites have an interaction trend that is positive, which produced higher Cr# and indicates aluminous spinel was undersaturated in the melt. The interaction trend suggests reaction with a melt with an IAT-type composition, consistent with a subduction zone setting. However, spinels from plagioclase-bearing peridotites evolve along a much lower slope, and appear to interact with a MORB-type melt. It is tempting to apply a MORB-type melt to the evolution of spinels from plagioclase-bearing peridotites, but it is inconsistent with their extremely high anorthite contents, which require abundant water for their formation (Sisson and Grove 1993; Koepke et al., 2004; Feig et al., 2006). The presence of plagioclase in plagioclase-bearing samples also indicates plagioclase was the stable aluminous phase,

which indicates melt-peridotite interaction in those samples did not evolve as a function of Cr#, and explains why the interaction slope is approximately zero. Instead, it is more likely that olivine and clinopyroxene were the first phases to fractionally crystallize from an IAT-type melt. Olivine and clinopyroxene crystallization was coincident with undersaturation in the aluminous phase, causing the positive interaction trend for clinopyroxene-bearing samples. This fractional crystallization caused the melt to evolve along the typical tholeiitic series trend. Early tholeiitic fractional crystallization typically increases Fe and Ti in the melt (e.g. Gill, 1981). A somewhat evolved IAT melt that is fractionally crystallizing plagioclase may have higher TiO_2 values than a typical IAT lava, and may resemble MORB lava levels of TiO_2. Relatively high TiO_2 melt reacting with spinel could lead to the very elevated TiO_2 values found in spinels from plagioclase-bearing samples (Fig. 18b). This could also explain the relative enrichment in Fe for olivine grains from Stage 2 units (Figure 16).

Like the two tarns harzburgite, all three Stage 2 units show enrichment in highly incompatible elements, with systematic negative Nb anomalies (Fig. 12h, Fig. 14). The enrichment pattern provides a likely fingerprint for the reacting melts, and is most consistent with a hydrous, supra-subduction zone melt. As described for the two tarns harzburgite, these analyses are at the limits of the detection method, but do suggest some degree of subduction zone component.

Finally, podiform chromitites from several centimeters to roughly 10 centimeters thickness occur locally within the Plateau and Ellis Stream complexes. These structures are known to form during subduction initiation (Rollinson and Adetunji, 2015), and are

not thought to occur in mid-ocean ridge settings (Rollinson and Adetunji, 2013).

Three-dimensional geometry of melt transport networks

In this section, I interpret the subsurface geometry of the Stage 2 melt transport column in the mantle wedge. Using the Plateau complex as a proxy for the interior portion of the melt transport system, and the plagioclase zone as the periphery, the three-dimensional geometry of the Stage 2 melt extraction system can be estimated using geologic mapping (Fig. 9b; Plate 1) and the construction of cross sections (Fig. 9d). I use the Plateau complex and plagioclase zone as a proxy for studying melt migration because the Ellis Stream complex is fault bounded. However, I assume the Ellis Stream complex would have similar zoning characteristics if its margins were preserved. Several interesting features are notable in cross section and on the map. First, as melts rise they create compositionally zoned conduits (Fig. 9d). These conduits pervasively alter the chemistries of the peridotites they ascend through. Second, in the north, the plagioclase zone (Fig. 9b) may represent a melt carapace, or cap to a subsurface melt conduit (Fig. 9d). These melt caps produce refertilization fronts at the extreme upper edge of percolating and fractionally crystallizing melts that froze during ascent. The refertilization fronts in the northern Red Hills may be analogous, though in a different tectonic setting, to the well studied refertilization front in the Ronda massif (van der Wal and Bodinier, 1996; Garrido and Bodinier, 1999; Lenoir et al., 2001).Other peridotite massifs show evidence for melts generated at depth rising upward and reacting with structurally overlying mantle peridotites. At the Lanzo peridotite massif, melts generated

in the asthenosphere both refertilized and depleted portions of the pre-existing continental lithospheric mantle (Piccardo et al., 2007). Refertilization from migrating melts has also been documented in the Lherz massif (Le Roux et al., 2007).

In the southern massif, where the Plateau complex widens to several kilometers, there is less evidence for melt crystallizing in place. As a result, melt ascending within the Plateau complex was likely transported to higher structural levels than is preserved in the northern Red Hills. A "successful" melt conduit may eventually feed melt into dike systems that move melt into crustal magma chambers or surface volcanoes.

The development of compositionally heterogeneous lithosphere in the forearc

In Chapter II, I examined mantle flow fabrics in the Red Hills ultramafic massif, and interpreted an incipient mantle forearc setting for deformation and melt migration. Results from this chapter support such a model, though also suggest an earlier mid-ocean ridge stage (Stage 1a) of melting. The early, incipient stages of subduction may be particularly important to the compositional development of mantle lithosphere in the forearc. Rapid slab rollback is predicted during the early stages of subduction, producing widespread extension, mantle upwelling, and in many cases the development of forearc spreading centers (Stern and Bloomer, 1992; Stern et al., 2012). Thus new lithosphere is often generated in such a setting. These forearc spreading centers are only active at the beginning of new subduction systems. Within approximately 10 Ma., the following sequence of events is thought to occur: 1) Cooling of the forearc; 2) Extension in the forearc diminishing; and 3) Magmatism migrating away from the trench and forearc,

forming a traditional volcanic arc complex (e.g., Stern et al., 2012 and references therein).

Using an incipient forearc tectonic setting, I can apply the results of this study to understand the creation and early history (Stages 1b and 2) of mantle lithosphere in the forearc. Figure 20 contains two schematic block diagrams illustrating the incipient subduction environment representative of the evolution of the Red Hills ultramafic massif. Figure 20a and 20b represent two time stages (t_1 and t_2) in the early evolution of an oceanic subduction zone system. As the slab rolls back and steepens from t_1 to t_2, space opens up above the descending plate. Mantle flows into the space created in an overall extensional environment, and rising melts are erupted in a forearc spreading center (Figure 20a, b). Decompression melting and volatiles both may contribute to the production of melts (e.g. Shervais, 2001). Location A in Figure 20a is an approximate location for Stage 1b melting of the Red Hills ultramafic massif. At these pressures (>6 kbar), melting and melt transport is relatively homogeneous and pervasive. At shallower depths closer to the spreading center during t_1, melt is no longer homogeneously distributed, but becomes focused into narrower conduits (location B).

Due to mantle upwelling from slab rollback, the Red Hills ultramafic massif begins to rise to shallower depths from t_1 to t_2. At time t_2, it is located at position C, and represents the development of Stage 2 melting and refertilization which overprints Stage 1 within the Plateau complex and plagioclase zone (Figure 20b). At such shallow depths, melt is no longer homogeneously distributed, but becomes focused into narrower conduits. Presumably, homogeneous melting continues at depth (position D) beneath the

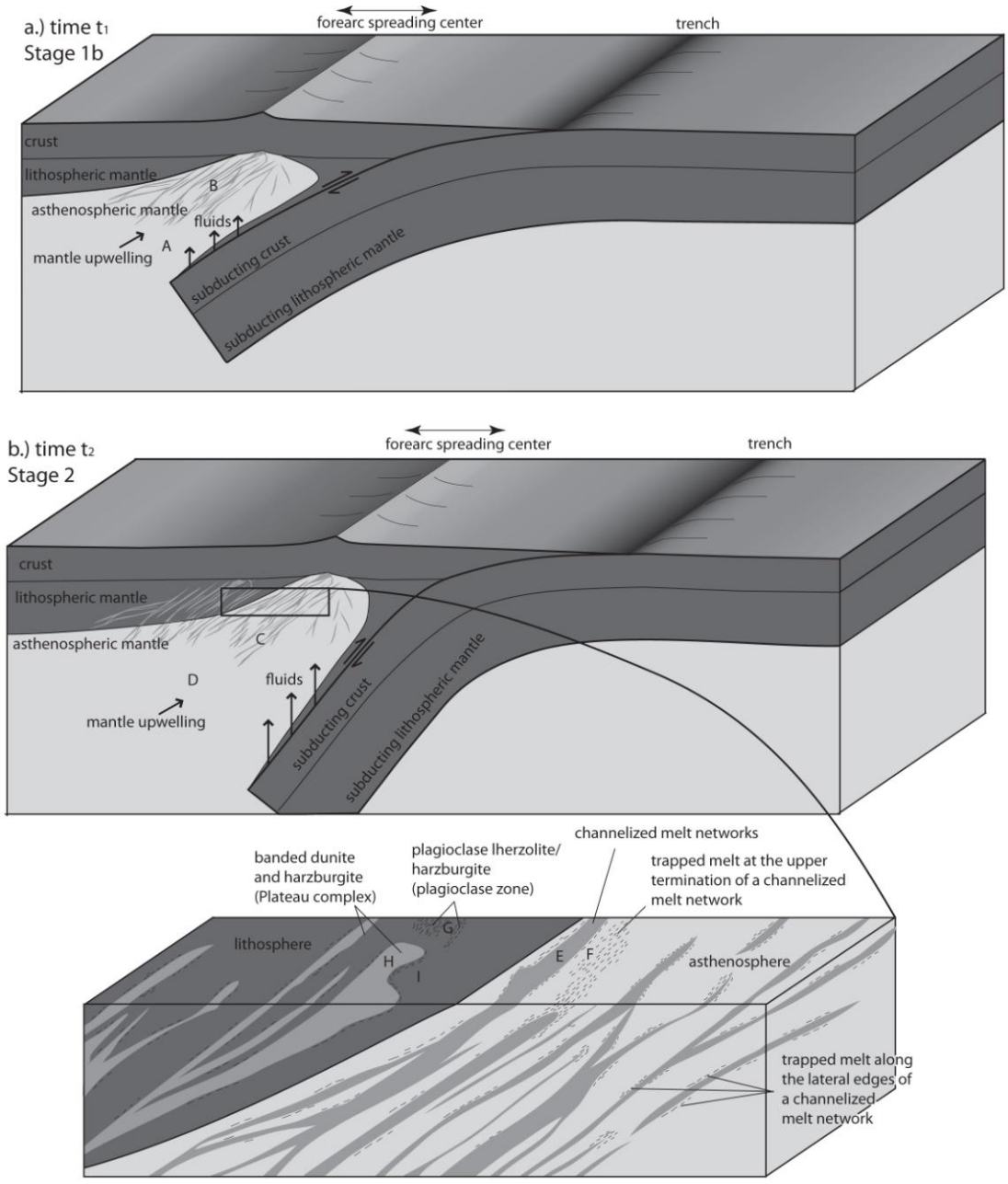

Fig. 20 – Schematic block diagrams illustrating two time stages (t_1 and t_2) in the initiation of a new subduction zone. See text for details on labeled locations. a.) Early stage in the development of a new subduction zone. Mantle upwelling and melt ascent in the nascent mantle wedge b.) Continued subsidence of the descending plate increases the dip of the slab relative to t_1, opening space in the mantle wedge, and causing widespread extension. The inset shows the transition from asthenospheric melting and upwelling to the cooler, solidified lithosphere. Melt networks in the asthenosphere solidify into compositionally banded dunite and harzburgite in the lithosphere, and trapped melt along the margins of asthenospheric melt networks solidify into plagioclase lherzolite and plagioclase harzburgite in the lithosphere. Black dashes on the inset figure represent trapped melt in the asthenosphere, and plagioclase-peridotites in the lithosphere.

Red Hills ultramafic massif, and supplies the melt transported through Stage 2 melt channels.

The inset diagram in Figure 20b illustrates in greater detail the compositional heterogeneity that results from Stage 2 melting and refertilization, and how this leads to a lithologically heterogeneous lithosphere. Location E represents a zone of focused (Stage 2) melt transport. Internally within the focused zone, melt flux is heterogeneous at the meter scale, containing both zones of high melt flux (melt channels), and zones of low melt flux (harzburgite and lherzolite matrix). Location F represents a zone of trapped and stagnating melt, occurring along the upper termination of a zone of focused melt transport. Stagnating melts also discontinuously occur along the lateral edges of the zones. As forearc spreading continues, through time the mantle cools, melts reach saturation in clinopyroxene and later plagioclase, and ultimately solid lithosphere forms. At any given time, melt is not being actively transported in every dunitic band, thus only active melt channels begin to crystallize clinopyroxene (Figure 10c, d, h) and plagioclase (Figure 10f). Non-active melt channels, where melt was being transported prior to reaching saturation in clinopyroxene and plagioclase, retain their dunite composition within harzburgite (Figure 10b, g). Thus zones of focused melt transport (Location E) cool into kilometer-scale bodies of compositionally banded dunites and harzburgites with minor lherzolite as they turn into lithosphere (Location H). Location H is analogous to the Plateau complex in the Red Hills ultramafic massif. Trapped and stagnating melts (Location F) crystallize during cooling, transforming harzburgite with a small melt fraction into plagioclase lherzolites and plagioclase harzburgites (Figure 10e). Location

G is analogous to the plagioclase zone, occurring as the byproduct of cooled, stagnated melts at the upper termination of focused melt transport zones and along the lateral edges of such zones. Importantly, the focused nature of melt extraction at shallow levels preserves evidence of early, pervasive melting (Stage 1a and 1b). Location I is analogous to the two tarns harzburgite, and represents early Stage 1a and 1b melting that did not become overprinted due to the focused nature of melt extraction at shallow levels.

Our results indicate residual peridotites (location I), such the two tarns harzburgite, preserve evidence for much earlier mid-ocean ridge melting, even in forearc tectonic settings. Studies of modern forearc peridotites have identified examples of residual mid-ocean ridge and back-arc basin peridotites that reacted with but did not re-equilibrate with subduction zone melts (Parkinson and Pearce, 1998; Pearce et al., 2000). The Red Hills ultramafic massif preserves the melt conduits that focus melt at shallow levels, allowing this preservation to occur. Together, our results and studies of modern forearc peridotites (e.g. Parkinson and Pearce, 1998; Pearce et al., 2000) suggest a model of increasingly focused melt extraction at shallower levels may be fairly common in forearc environments.

SUMMARY

The Red Hills ultramafic massif records an early widespread melting event (Stage 1a and 1b) and later focused melt transport event (Stage 2 melt reaction and refertilization) that produced a compositionally heterogeneous forearc mantle. Stage 1 melting, represented by the two tarns harzburgite, produced whole rock major element

and modal compositions with small variability (harzburgites). Chondrite normalized LREE are strongly enriched, while heavy and middle REE are strongly depleted. Changes in fO_2 in the massif appear to be largely related to the degree of melting or melt reaction, rather than to refertilization. Relative to the FMQ buffer, the massif is characterized by slightly more than 2 log units of variability in fO_2. Stage 2, represented by the Plateau and Ellis Stream complexes and the plagioclase zone, produced both more depleted compositions (dunites) and more fertile compositions from refertilization (lherzolites). Stage 2 produced map-scale compositional zoning, characterized by the modal addition of plagioclase and clinopyroxene (± orthopyroxene ± olivine) on the periphery and the development of compositionally banded dunite and harzburgite and local zones of plagioclase lherzolite in the core. LREE enrichment is more subdued in Stage 2 units, and HREE are typically more enriched, likely due to the host peridotite reacting with larger time integrated melt fractions within the melt networks. Melting (Stage 1) and subsequent focused melt ascent (Stage 2) during subduction initiation produced a compositionally heterogeneous lithosphere. Melt focusing helps preserve evidence of much earlier, residual mid-ocean ridge melting, even in subduction zone environments.

CHAPTER IV

CONSTRICTIONAL, TRENCH-PARALLEL MANTLE FLOW DURING SUBDUCTION INITIATION

SYNOPSIS

The Red Hills ultramafic massif in the South Island, New Zealand, contains a two-stage history of high temperature mantle flow during subduction initiation along the Gondwanan margin. Initial deformation was homogeneous and strongly constrictional, and the rocks can be approximated as L-tectonites. Kilometer-scale deformation zones, part of the second stage of deformation, overprinted the early homogeneous fabric throughout the western portion of the massif. Timing of all high-temperature mantle deformation in the Red Hills was between 285 and 274 Ma during subduction initiation based on the earliest ages of igneous activity in adjacent volcanic rocks, and a new U-Pb zircon age of 274.55±0.43 Ma from a cross-cutting dike. I present a kinematic model to explain the occurrence of the L-tectonites during subduction initiation, and find that the three-dimensional boundary conditions for deformation in the incipient mantle wedge must have been transtensional, nearly monoclinic, with a dominant trench-parallel component of motion. Such a scenario indicates subduction likely initiated along an active oceanic transform fault. I test this model by kinematically restoring the Red Hills ultramafics to their Permian orientation, and find the L-tectonites were oriented nearly parallel to the trench, and the Stage 2 deformation zones were variably oriented, but all accommodated normal motion. These results support a model where the incipient mantle

wedge was undergoing highly oblique transtension, and the lack of evidence for contraction suggests the onset of subduction along the Permian margin of New Zealand occurred along a transform fault due to spontaneous, density driven processes.

INTRODUCTION

Subduction initiation is an essential, but enigmatic, part of plate tectonics. Many subduction zones, such as the Izu-Bonin-Mariana system, are thought to have initiated along old fracture zones or oceanic transform faults (e.g., Casey and Dewey, 1984; Gurnis et al., 2004; Stern, 2004; Choi et al., 2008). Initiation may result from spontaneous subsidence due to density-driven differences (Stern and Bloomer, 1992; Dymkova and Gerya, 2013) or due to shortening and underthrusting from an externally imposed change in plate motion (Casey and Dewey 1984; Hall et al., 2003; Gurnis et al., 2004). The question is: How can we determine between these models?

Many, if not most, supra-subduction ophiolite sequences are generated in forearc settings at the onset of subduction (Shervais, 2001; Stern et al., 2012). Thus, the empirical observations from exposed mantle rocks in ophiolites can potentially be used to elucidate the three-dimensional nature of mantle flow during subduction initiation.

I present structural data from the Red Hills ultramafic massif, which was actively deforming during subduction initiation. The presence of L-tectonites in the massif provides key constraints on flow conditions in the mantle during subduction initiation. I utilize the L-tectonites to find subduction initiation occurred along an active transform

fault, and was driven by density differences rather than shortening due to a plate motion reorganization.

GEOLOGIC SETTING

The Red Hills ultramafic massif is part of the Dun Mountain Ophiolite Belt (DMOB) of the South Island, New Zealand (Fig. 21). The DMOB was created at the onset of subduction (Sivell and McCulloch, 2000) in a forearc setting in the Middle Permian (285-269 Ma) (Kimbrough et al., 1992; Sivell and McCulloch, 2000), and it likely formed immediately prior to the establishment of a magmatic arc along the New Zealand (ca. 265 Ma; Kimbrough et al., 1992) and Australian (ca. 255 Ma; Caprarelli and Leitch, 1998) portions of the Gondwanan margin. The DMOB and parts of several other tectonostratigraphic packages were folded approximately 80° in the Mesozoic into the Nelson Regional Syncline (Walcott, 1969; Coombs et al., 1976).

Chapter II established four compositional units in the Red Hills ultramafic massif (RHUM). From E to W (Fig. 21b), they include massive, lineated harzburgites (two tarns harzburgite), plagioclase lherzolites and plagioclase harzburgites (plagioclase zone), compositionally banded dunite and harzburgite (Plateau complex), and dunite-rich compositionally banded dunite and harzburgite (Ellis Stream complex) affected by a sub-solidus shear zone (Ellis Stream shear zone) (see Chapter II).

The two tarns harzburgite is characterized by a strongly linear fabric, and is interpreted to be an L-tectonite (Fig. 21c); the unit locally contains a weak foliation but its orientation is inconsistent across the unit. The unit equilibrated at approximately

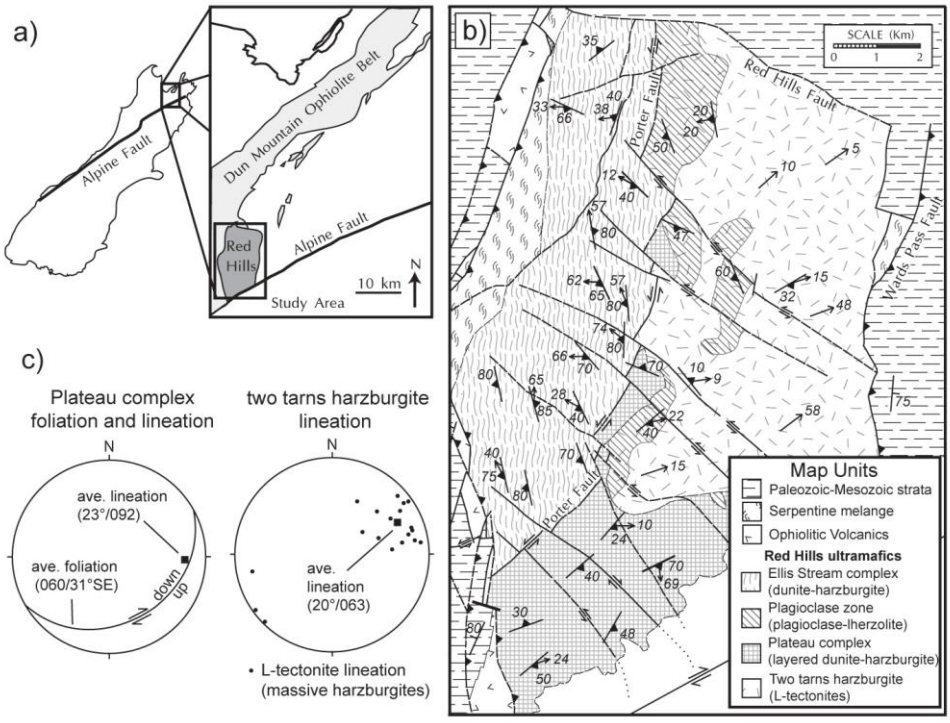

Figure 21 – Location map, geologic map and stereographic plots of the Red Hills. a.) Location map of massif, modified from Webber et al (2008). b.) Geological map of the Red Hills massif. c.) Equal area stereographic plots showing current fabric orientation in the massive harzburgites and Plateau complex.

1200°C in a subduction zone environment (see Chapter II, III). Units in the western half of the massif (plagioclase zone, Plateau complex, Ellis Stream complex) overprint the L-tectonites exposed in the eastern massif. Deformation is interpreted to have also been in a subduction zone environment, and been synchronous with focused melt migration at temperatures of approximately 1000°C and at pressures of around 5 kbar (see Chapter II). Overall, the massif can be divided into two main stages of high temperature deformation, both occurring in a subduction zone environment: Stage 1 - Development of homogeneous strongly constrictional strain in the two tarns harzburgite (L-tectonites); Stage 2 – Overprinting heterogeneous strain in the plagioclase zone, Plateau complex, and Ellis Stream complex in the western massif. Regional arguments suggested both

stages of deformation occurred during the onset of a new subduction zone (see Chapter II). I test for a subduction initiation setting with new chemical abrasion isotope dilution thermal ionization mass spectrometry (CA-ID TIMS) geochronology below.

CA-ID-TIMS GEOCHRONOLOGY METHODS AND RESULTS

To constrain the age of deformation, I dated a plagiogranite dike that cross-cuts the foliation in the Ellis Stream complex. Most of the Ellis Stream complex is affected by the Ellis Stream shear zone. Given that this unit is the only one affected by pervasive sub-solidus deformation, the cross-cutting dike effectively dates the cessation of deformation in the Red Hills. Heavy minerals were separated from a crushed and ground sample, and individual zircons were handpicked for quality. Grains were annealed and chemically abraded to reduce the effect of Pb-loss following the methods of Mattinson (2005). After chemical abrasion, complete dissolution and equilibration with a mixed ^{205}Pb-^{233}U-^{236}U spike were achieved using hydrofluoric acid in a pressure-dissolution vessel. Uranium and Lead were separated and isotope ratios were measured in a Thermo Scientific Triton thermal ionization mass spectrometer (TIMS) at Texas A&M University. More details on the analytical methods used can be found in Hughes et al. (2013). Due to extremely low measured U and Pb levels, several multi-grain samples were run in addition to single grain analyses. Both single and multi-grain samples yielded concordant results, and produced a weighed mean age of 274.55±0.43 Ma (Fig. 22, see Appendix C).

The 274.55±0.43 Ma cross-cutting plagiogranite dike marks the youngest

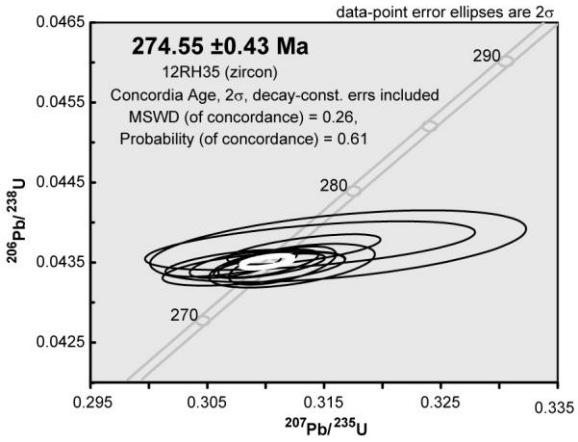

Figure 22 - Concordia plot. Age of zircon from a plagiogranite dike that cross-cuts the Ellis Stream fabric.

possible age for melt-present Stage 2 deformation. Thus, all high temperature mantle deformation in the RHUM (Stages 1 and 2) occurred prior to ca. 274 Ma. The earliest subduction-related magmatic age associated with the dismembered and fault-bounded crustal blocks of the DMOB is 285 Ma (Kimbrough et al., 1992). Consequently, all melt-present deformation in the ultramafic section occurred in ~10 m.y. (285-274.55±0.43 Ma), during the earliest stages of renewed subduction along the Gondwanan margin (Caprarelli and Leitch, 1998). Thus, I conclude Stage 1 and Stage 2 deformation in the RHUM occurred in a subduction initiation setting.

KINEMATIC MODEL FOR L-TECTONITE DEVELOPMENT

In this section, I utilize the presence of L-tectonites in the two tarns harzburgite to constrain the three-dimensional boundary conditions for mantle flow in the incipient mantle wedge. This is possible because pure linear fabrics require very specific boundary conditions to form under homogeneous, steady-state strain conditions. L-

tectonites can also form from overprinting deformations, locally in fold hinges, and from restraining or releasing bends in shear zones (e.g. Sullivan, 2013), but these are considered unlikely for the Red Hills due to the homogenous nature of the two tarns harzburgite.

During homogeneous, steady-state strain, pure linear fabrics, as well as highly linear fabrics in general, are predicted to form in strongly oblique divergent settings in monoclinic, transtensional deformation (Fossen and Tikoff, 1993; Fossen and Tikoff, 1998; Teyssier and Tikoff, 1999; Dewey, 2002). Divergence angles of 15-20 degrees under reasonable strains are predicted to form L-tectonites if there is no lateral (pure shear) extrusion (Teyssier and Tikoff, 1999; Dewey, 2002). Adding lateral extrusion parallel to simple shearing in monoclinic transtension reduces the divergence angle (i.e. less than 20 degrees, or more margin-parallel dominated) required for pure linear fabrics to form (Fossen and Tikoff, 1998). Thus the presence of highly linear rocks in the Red Hills suggests they formed under approximately monoclinic, transtensional conditions, though it is uncertain whether there was lateral extrusion or not. Besides transtension, monoclinic transpressional deformations with strike-slip parallel, lateral extrusion and vertical shortening (i.e. type E transpression of Fossen and Tikoff, 1998) are also predicted to form highly linear fabrics. However, margin normal shortening is unlikely in the highly extensional incipient forearc environment present in the Red Hills during L-tectonite development. Therefore, a key point is that under any reasonable flow conditions, the linear fabric in the two tarns harzburgite must have been dominated by margin parallel flow in an overall transtensional setting.

Transtensional (and transpressional) deformation does not necessarily have to develop under monoclinic symmetry. However, introducing an obliquity between the simple shear direction and the principal coaxial stretches under transtensional conditions (i.e. triclinic transtension) prevents pure linear fabrics from forming (Lin et al., 1998). Yet as the triclinic obliquity decreases and approaches a monoclinic state, finite strain ellipsoid shapes can approach pure constriction (Lin et al., 1998). In practice, highly constrictional rock fabrics are difficult to differentiate from pure constriction, and for this reason a weakly triclinic system in the Red Hills is possible, and perhaps likely.

I propose a simple monoclinic, transtensional kinematic model for the development of L-tectonites in the Red Hills (Fig. 23). I acknowledge some small degree of triclinic symmetry is possible and perhaps likely. Because the boundary conditions of deformation in the mantle wedge during subduction initiation are linked to the dipping slab, our system is analogous to an inclined version of transtension. I model the maximum coaxial stretch direction up the shallowly dipping slab (Fig. 23a), rather than horizontal in traditional transtension. Simple shearing is horizontal and parallel to the intermediate coaxial stretch direction. However, the simple shear plane is inclined (see cross-section in Fig. 23a) due to the dip of the descending slab. The minimum coaxial stretch direction is normal to the plane of the sinking slab (Fig. 23a), and normal to the maximum coaxial stretch direction and the simple shear direction. For strike-slip dominated systems with low divergence angles, such a model will produce strongly linear rocks with a lineation oriented at a relatively small angle to the plate margin, assuming at least moderate strain.

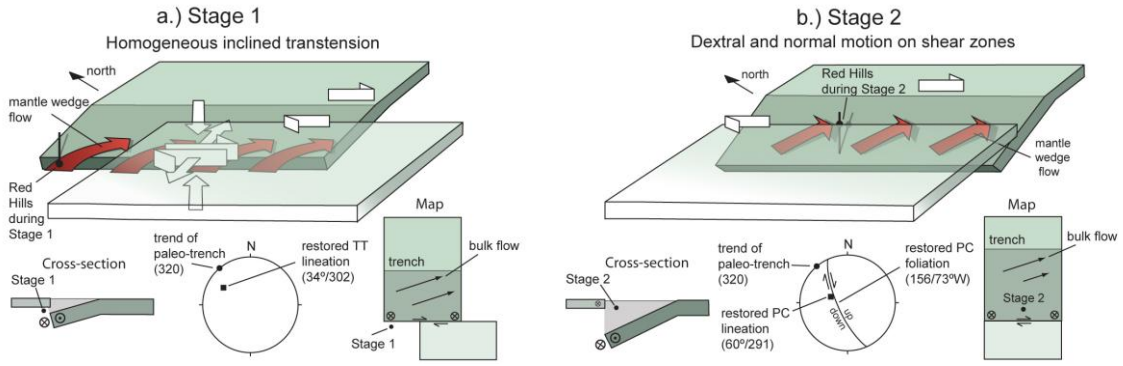

Figure 23 - Map, cross-section, three-dimensional conceptual diagram, and equal area stereographic plots. The figure illustrates the progressive exhumation of the ultramafic rocks in the Red Hills within an overall transtensional regime. a.) Stage 1 represents the formation of L-tectonites during pervasive, distributed deformation at >6 kb pressure. Red arrows represent mantle flow. White arrows represent kinematic boundary conditions imposed by relative motion between the plates. b.) Stage 2 represents the localization of melt and deformation into shear zones at shallower depths (5 kbar pressure).

PERMIAN RESTORATION

To test our kinematic model, I restored the average L-tectonite orientation from its current orientation to its Permian orientation and compared it to an estimate of the orientation of the Permian plate boundary. My model predicts the L-tectonite lineation should be oriented at a small angle relative to the trench, assuming modest strains. The orientation of the Permian trench can be estimated if I assume the trench was parallel to the Late Permian Brook Street volcanic arc, which parallels the DMOB to the west, and is currently oriented 030. I first rotate all current orientations counterclockwise 70° about a vertical axis to account for distributed crustal deformation associated with movement along the Alpine fault (e.g. Sutherland, 1999). Second, I account for Mesozoic rotation of the Permian Maitai Group sediments that overly the ophiolite. The Mesozoic rotation axis was oriented parallel to the trend of the trench, so no change occurs in the orientation of the Permian trench. Mesozoic rotation was 80 degrees, with sedimentary

rocks younging to the west (Walcott, 1969). These rotations indicate the Permian trench had a trend of approximately 320 (i.e. northwestward, Fig. 23), while the average L-tectonite lineation rotates from its current orientation of 20° at 063 (Fig. 21c) to 34° at 302 in the Permian (Fig. 23a). Thus the restored lineation trend in the L-tectonites shows an 18° obliquity to the trend of the Permian trench when restored (Fig. 23a). Uncertainty in such a calculation is likely significant, around 20°. I view this result as a first order estimate, and note that I assume there was not any significant fault-normal rotation along the bounding faults of the massif.

Despite the uncertainty in the calculation, this restored L-tectonite orientation is remarkably consistent with our modeled predictions. First, during progressive steady-state strain in transtension, lineations rapidly approach the direction of oblique divergence (Fossen et al., 1994). An 18° obliquity relative to the paleo-trench is consistent with either moderate to high strain during monoclinic transtension with no lateral extrusion, since pure linear fabrics only occur if the angle of divergence is ~15-20°. Alternatively, it is also consistent with lower strains in a system with lateral extrusion, where the angle of oblique divergence is less than 15°. Hence the low degree of obliquity is consistent with our kinematic model predicting dominantly margin parallel flow. Second, the direction of obliquity after restoration implies a dextral component of deformation, which is consistent with plate motion reconstructions for the Permian Gondwana margin (Adams et al., 2007). Finally, the shallow restored L-tectonite plunge to the northwest is consistent with simple shearing on an inclined shear plane (cross-section Fig. 23a).

MODEL FOR MANTLE FLOW DURING SUBDUCTION INITIATION

Building on two-dimensional conceptualizations of mantle flow during subduction initiation (e.g. Stern and Bloomer, 1992; Hall et al., 2003), I have incorporated the observed three-dimensional fabrics from the Red Hills into a three-dimensional model for plate boundary movement and associated mantle flow (Fig. 23). In the model, I have restored both Stage 1 L-tectonites and Stage 2 overprinting deformation zones in the RHUM to their pre-emplacement Permian position, as described above.

Figure 23a and b track the progressive oblique exhumation of mantle rocks from the Red Hills during subduction initiation. I infer that subduction initiated along an oceanic transform fault due to the requirement of strike-slip dominated transtension from our kinematic model. The two time steps in Figure 23a and b correlate to the two stages of deformation: 1) Lineated fabric in the two tarns harzburgite; 2) Deformation zone development in the western half of the massif. Importantly, the restored fabrics from each time stage require a significant trench-parallel component of deformation.

During the time of formation of the lineated harzburgite (Stage 1), I infer transtensional deformation at >6 kbar pressure in the mantle wedge (see Chapter II). Transtensional strain was a consequence of boundary conditions imposed on the mantle wedge from subduction initiation along an active transform fault. Extrusion in the nascent mantle wedge up the dip of the slab (and slab normal shortening) results from extensional flow filling the space above the subsiding lithosphere (Fig. 23a). The strike-slip component results from the relative motion of the two adjacent plates. Hence, deeper

mantle rocks obliquely flow into the mantle wedge at a very low angle (18°) to the trench.

The second phase of deformation (Stage 2) is best represented by the Plateau complex from the central and southern RHUM (Fig. 21b, 23b). Stage 2 developed at approximately 1000°C and 5 kbar pressure (Webber et al., 2008; Chapter II). At these shallower conditions in the mantle wedge, melt and deformation are focused into narrower conduits and shear zones (Chapter II). Consequently, it is the kinematics of motion on the shear zones that constrain plate-margin deformation, rather than homogeneous strain. Trench-normal extension and trench-parallel shearing continue as a result of ongoing trench retreat and concurrent strike-slip motion (Fig. 23b; Stage 2).

DISCUSSION

To date, mantle flow during subduction initiation has been largely explored through numerical modeling. In intra-oceanic settings, numerical models have shown that both spontaneous, density driven differences across transform faults or oceanic fractures (Dymkova and Gerya, 2013) and shortening across transform faults (Hall et al., 2003; Gurnis et al., 2004) can drive the initiation of new subduction zones. Our results test these models empirically, and are most consistent with initiation along an active transform fault. Due to the lack of shortening structures in the massif, it is more likely spontaneous subsidence due to density differences drove the initiation of subduction.

Numerical models have also predicted a component of margin parallel flow both in the mantle and in accreting sediments from curved subduction boundaries (Malatesta

et al., 2013; Marques et al., 2014). Some of the margin parallel flow I invoke could result from curvature of the initial subduction trench. However, the strongly oblique divergence angle (≤20°) required to form L-tectonites is difficult to explain solely through plate margin curvature, as curved margins decrease vertical density contrasts, making subduction nucleation more difficult (Marques et al., 2014).

These results highlight the important role of three-dimensional boundary conditions in determining mantle wedge flow. Homogeneous flow in the mantle is a function of not just relative plate motions but also absolute trench motion. This study predicts dominantly trench-parallel, constrictional mantle flow in forearc environments may be a common phenomena in incipient subduction settings if subduction zones often nucleate along active transform margins.

SUMMARY

Fabric studies on the Red Hills ultramafic complex provides direct observational constraints on deformation in the nascent mantle wedge. Two stages of deformation, first homogeneous transtensional strain and second, narrower overprinting deformation zones, occurred during exhumation of the incipient mantle wedge. CA-ID-TIMS geochronology on a cross-cutting plagiogranite dike requires both stages of deformation in the ultramafic section to have occurred within the first 10 m.y. of subduction initiation along the Gondwanan margin (285-274.55±0.43 Ma). Strongly oblique inclined transtension, caused by subduction initiation along an active transform margin, is the favored setting for the development of deformation in the Red Hills ultramafic massif.

CHAPTER V

CONCLUSION

The Red Hills ultramafic massif contains a multi-stage melting and deformation history. Initial melting (Stage 1) produced the two tarns harzburgite, characterized by homogeneous, depleted major element geochemical characteristics. Oxygen fugacity values from across the massif largely reflect Stage 1 melting, varying linearly as a function of spinel Cr# from logfO_2(ΔFMQ) -1.5 to +0.6. The linear trend in fO2 relative to spinel Cr# indicates Stage 1 can be further divided into an initial episode of melting in a relatively reduced, mid-ocean ridge environment (Stage 1a) around logfO_2(ΔFMQ) -1.5, that was followed by additional melting in a more oxidized, supra-subduction zone environment (Stage 1b). Homogeneous melting during Stage 1b was coincident with the development of homogeneous constrictional strain in the two tarns harzburgite. Strain can be approximated as an L-tectonite, and occurred at a temperature of approximately 1200°C and pressures in excess of 6 kbar.

At lower pressures of around 5 kbar, and temperatures of 1000°C, a second stage of melt migrated through the western massif (Stage 2), creating the Plateau and Ellis Stream complexes and plagioclase zone. The Plateau complex represents the core of a kilometer-scale melt transport system, while the plagioclase zone represents the periphery of the system. In the core, Stage 2 melts were typically channelized, and were undersaturated in orthopyroxene, creating dunite bands. In the periphery, melts were not channelized, and as they cooled, percolative fractional crystallization resulted in the

addition of clinopyroxene and plagioclase to the previously depleted peridotites. Stage 2 melts cryptically metasomatized all Stage 2 units, resulting in Fe-enrichment in olivine and TiO_2 enrichment in spinel. TiO_2 enrichment trends in spinel suggest early crystallization of clinopyroxene and later crystallization of plagioclase, consistent with the crystallization sequence found in hydrated subduction zone melts. Additionally, plagioclase in Stage 2 units is highly anorthitic, also characteristic of subduction zone hydrous melts. Based in part on these characteristics, Stage 2 also developed in a subduction zone environment. Deformation during Stage 2 mirrored the petrologic history by also becoming focused into narrower zones at shallower depths. Deformation during Stage 2 is interpreted to be synchronous with melt migration, and was restricted to units with migrating Stage 2 melts. Deformation produced lineated and foliated fabrics that overprinted early constrictional Stage 1 fabrics. CA-ID-TIMS analysis of zircon from a plagiogranite dike that cross-cuts the Stage 2 fabric indicates Stage 2 occurred prior to 274.55±0.43 Ma. The earliest subduction-related magmatism in New Zealand began around 285 Ma, suggesting both Stage 1b and Stage 2 occurred during the first 10 million years of an incipient subduction zone.

The geologic history outlined above is utilized in this dissertation to understand upper mantle wedge processes during subduction initiation. First, the highly constrictional fabrics that characterize the Stage 1 two tarns harzburgite is interpreted to record highly oblique transtension during subduction initiation. This suggests Middle Permian subduction along the New Zealand portion of the Gondwanan margin initiated along a transform fault. Flow resulting from transtension was dominantly trench-parallel.

Fabric stability was directly related to the three-dimensional boundary conditions imposed on the early mantle wedge by relative plate motion and by subsidence of the down-going plate. Second, this dissertation documents how strain changes from homogeneous at high pressures (>6 kbar), high temperature (1200°C), to localized at lower pressures (5 kbar), lower temperature (1000°C). Because deformation appears to be coupled to melt migration, it is likely the distribution of melt in the mantle wedge is a first-order control on strain localization. Finally, the multi-stage melt history of the Red Hills in a supra-subduction zone environment significantly increased the compositional heterogeneity of depleted mid-ocean ridge peridotite. Rising subduction-related melts became focused at shallower levels, and some melts stagnated and cooled in place. The focusing of melts at shallower levels suggests large portions of modern forearc mantle may contain residual mid-ocean ridge peridotites from earlier tectonic events.

REFERENCES

Adams, C. J., Campbell, H. J., and Griffin, W. L., 2007, Provenance comparisons of Permian to Jurassic tectonostratigraphic terranes in New Zealand: perspectives from detrital zircon age patterns: Geological Magazine, v. 144, no. 04, p. 701.

Aharonov, E., Whitehead, J. A., Spiegelman, M., and Kelemen, P., 1995, Channeling instability of upwelling melt in the mantle: Journal of Geophysical Research, v. 102, p. 14821-14833.

Arai, S., 1994, Characterization of spinel peridotites by olivine-spinel compositional relationships: review and interpretation: Chemical geology, v. 113, no. 3, p. 191-204.

Asimow, P. D., and Ghiorso, M. S., 1998, Algorithmic modifications extending MELTS to calculate subsolidus phase relations: American Mineralogist, v. 83, p. 1127-1132.

Bach, W., Garrido, C. J., Paulick, H., Harvey, J., and Rosner, M., 2004, Seawater-peridotite interactions: First insights from ODP Leg 209, MAR 15°N: Geochemistry, Geophysics, Geosystems, v. 5, no. 9, p. n/a-n/a.

Ballhaus, C., Berry, R., and Green, D., 1991, High pressure experimental calibration of the olivine-orthopyroxene-spinel oxygen geobarometer: implications for the oxidation state of the upper mantle: Contributions to Mineralogy and Petrology, v. 107, no. 1, p. 27-40.

Batanova, V., Belousov, I., Savelieva, G., and Sobolev, A., 2011, Consequences of channelized and diffuse melt transport in supra-subduction zone mantle: evidence from the Voykar Ophiolite (Polar Urals): Journal of Petrology, v. 52, no. 12, p. 2483-2521.

Batanova, V. G., and Sobolev, A. V., 2000, Compositional heterogeneity in subduction-related mantle peridotites, Troodos massif, Cyprus: Geology, v. 28, no. 1, p. 55-58.

Bodinier, J., Vasseur, G., Vernieres, J., Dupuy, C., and Fabries, J., 1990, Mechanisms of mantle metasomatism: geochemical evidence from the Lherz orogenic peridotite: Journal of Petrology, v. 31, no. 3, p. 597-628.

Brey, G. P., and Kohler, T., 1990, Geothermobarometry in 4-phase lherzolites II. New thermobarometers, and practical assessment of existing thermobarometers: Journal of Petrology, v. 31, no. 6, p. 1353-1378.

Burov, E., and Cloetingh, S., 2010, Plume-like upper mantle instabilities drive subduction initiation: Geophysical Research Letters, v. 37.

Canil, D., and O'Neill, H. S. C., 1996, Distribution of Ferric Iron in some Upper-Mantle Assemblages: Journal of Petrology, v. 37, no. 3, p. 609-635.

Caprarelli, G., and Leitch, E. C., 1998, Magmatic changes during the stabilisation of a cordilleran fold belt: the Late Carboniferous-Triassic igneous history of eastern New South Wales, Australia: Lithos, v. 45, p. 413-430.

Casey, J. F., and Dewey, J. F., 1984, Initiation of subduction zones along transform and accreting plate boundaries, triple-junction evolution, and forearc spreading centres—implications for ophiolitic geology and obduction Geological Society, London, Special Publications, v. 13, p. 269-290.

Choi, S. H., Mukasa, S. B., and Shervais, J. W., 2008, Initiation of Franciscan subduction along a large-offset fracture zone: Evidence from mantle peridotites, Stonyford, California: Geology, v. 36, no. 8, p. 595.

Coombs, D. S., Landis, C. A., Norris, R. J., Sinton, J. M., Borns, D. J., and Craw, D., 1976, The Dun Mountain Ophiolite Belt, New Zealand, its Tectonic Setting, Constitution, and Origin, with Special Reference to the Southern Portion: American Journal of Science, v. 276, p. 561-603.

Daines, M. J., and Kohlstedt, D. L., 1994, The transition from porous to channelized flow due to melt/rock reaction during melt migration: Geophysical Research Letters, v. 21, p. 145-148.

Daines, M. J., and Kohlstedt, D. L., 1997, Influence of deformation on melt topology in peridotites: Journal of Geophysical Research, v. 102, no. B5, p. 10257.

Dare, S. A. S., Pearce, J. A., McDonald, I., and Styles, M. T., 2009, Tectonic discrimination of peridotites using fO2–Cr# and Ga–Ti–FeIII systematics in chrome–spinel: Chemical geology, v. 261, no. 3-4, p. 199-216.

Deen, T. J., Griffin, W., Begg, G., O'Reilly, S. Y., Natapov, L., and Hronsky, J., 2006, Thermal and compositional structure of the subcontinental lithospheric mantle: Derivation from shear wave seismic tomography: Geochemistry, Geophysics, Geosystems, v. 7, no. 7.

Dewey, J. F., 2002, Transtension in Arcs and Orogens: International Geology Review, v. 44, no. 5, p. 402-439.

Dewey, J. F., Holdsworth, R. E., and Strachan, R. A., 1998, Transpression and transtension zones: Geological Society, London, Special Publications, v. 135, p. 1-14.

Dick, H. J. B., and Bullen, T., 1984, Chromian spinel as a petrogenetic indicator in abyssal and alpine-type peridotites and spatially associated lavas: Contributions to Mineralogy and Petrology, v. 86, p. 54-76.

Dijkstra, A. H., Drury, M. R., Vissers, R. L. M., and Newman, J., 2002, On the role of melt-rock reaction in mantle shear zone formation in the Othris Peridotite Massif (Greece): Journal of Structural Geology, v. 24, p. 1431-1450.

Dilek, Y., and Thy, P., 2009, Island arc tholeiite to boninitic melt evolution of the Cretaceous Kizildag (Turkey) ophiolite: Model for multi-stage early arc-forearc magmatism in Tethyan subduction factories: Lithos, v. 113, p. 68-87.

Dymkova, D., and Gerya, T., 2013, Porous fluid flow enables oceanic subduction initiation on Earth: Geophysical Research Letters, v. 40, no. 21, p. 5671-5676.

Fabriès, J., 1979, Spinel-olivine geothermometry in peridotites from ultramafic complexes: Contributions to Mineralogy and Petrology, v. 69, no. 4, p. 329-336.

Feig, S. T., Koepke, J., and Snow, J. E., 2006, Effect of water on tholeiitic basalt phase equilibria: an experimental study under oxidizing conditions: Contributions to Mineralogy and Petrology, v. 152, p. 611-638.

Fossen, H., and Tikoff, B., 1993, The deformation matrix for simultaneous simple shearing, pure shearing and volume change, and its application to transpression-transtension tectonics: Journal of Structural Geology, v. 15, no. 3-5, p. 413-422.

Fossen, H., and Tikoff, B., 1998, Extended models of transpression and transtension, and application to tectonic settings, in Holdsworth, R. E., Strachan, R. A., and Dewey, J. F., eds., Continental Transpressional and Transtensional Tectonics, Volume 135, Geological Society, London, Special Publications, p. 15-33.

Fossen, H., Tikoff, B., and Teyssier, C., 1994, Strain modeling of transpressional and transtensional deformation: Norsk Geologisk Tidsskrift, v. 74, p. 134-145.

Frost, D. J., and McCammon, C. A., 2008, The redox state of Earth's mantle: Annu. Rev. Earth Planet. Sci., v. 36, p. 389-420.

Garrido, C. J., and Bodinier, J.-L., 1999, Diversity of mafic rocks in the Ronda peridotite: evidence for pervasive melt–rock reaction during heating of subcontinental lithosphere by upwelling asthenosphere: Journal of Petrology, v. 40, no. 5, p. 729-754.

Gill, J. B., 1981, Orogenic Andesites and Plate Tectonics, Berlin, Springer-Verlag.

Green, D. H., 1972, Magmatic activity as the major process in the chemical evolution of the earth's crust and mantle: Tectonophysics, v. 13, p. 42-71.

Gurnis, M., Hall, C., and Lavier, L., 2004, Evolving force balance during incipient subduction: Geochemistry, Geophysics, Geosystems, v. 5, no. 7, p. n/a-n/a.

Hall, C. E., Gurnis, M., Sdrolias, M., Lavier, L. L., and Müller, R. D., 2003, Catastrophic initiation of subduction following forced convergence across fracture zones: Earth and Planetary Science Letters, v. 212, no. 1-2, p. 15-30.

Harte, B., Hunter, R. H., and Kinny, P. D., 1993, Melt geometry, movement and crystallization, in relation to mantle dykes, veins and metasomatism: Philosophical Transactions Royal Society of London: Physical Sciences and Engineering, v. 342, p. 1-21.

Hellebrand, E., Snow, J. E., Dick, H. J. B., and Hofmann, A. W., 2001, Coupled major and trace elements as indicators of the extent of melting in mid-ocean-ridge peridotites: Nature, v. 410, p. 677-681.

Holtzman, B. K., Kohlstedt, D. L., Zimmerman, M. E., Heidelbach, F., Hiraga, T., and Hustoft, J., 2003a, Melt segregation and strain partitioning: implications for seismic anisotropy and mantle flow: Science, v. 301, p. 1227-1230.

Holtzman, B. K., Groebner, N. J., Zimmerman, M. E., Ginsberg, S. B., and Kohlstedt, D. L., 2003b, Stress-driven melt segregation in partially molten rocks: Geochemistry, Geophysics, Geosystems, v. 4, 8607.

Houghton, B. F., and Landis, C. A., 1989, Sedimentation and volcanism in a Permian arc-related basin, southern New Zealand: Bulletin of Volcanology, v. 51, no. 6, p. 433-450.

Hughes, K. S., Hibbard, J. P., and Miller, B. V., 2013, Relationship between the Ellisville pluton and Chopawamsic fault: Establishment of significant Late Ordovician faulting in the Appalachian Piedmont of Virginia: American Journal of Science, v. 313, no. 6, p. 584-612.

Ishizuka, O., Tani, K., Reagan, M. K., Kanayama, K., Umino, S., Harigane, Y., Sakamoto, I., Miyajima, Y., Yuasa, M., and Dunkley, D. J., 2011, The timescales of subduction initiation and subsequent evolution of an oceanic island arc: Earth and Planetary Science Letters, v. 306, p. 229-240.

Johnson, D., Hooper, P., and Conrey, R., 1999, XRF analysis of rocks and minerals for major and trace elements on a single low dilution Li-tetraborate fused bead: Advances in X-ray Analysis, v. 41, p. 843-867.

Johnston, M. R., 1981, Sheet 027AC - Dun Mountain: Department of Scientific and Industrial Research.

Johnston, M. R., 1982, Sheet M28BD - Red Hills: Department of Scientific and Industrial Research.

Johnston, M. R., 1983, Sheet N28AC - Motupiko: Department of Scientific and Industrial Research.

Johnston, M. R., 1990, Geology of the St. Arnaud District, Southeast Nelson (sheet N29), 119.

Jugum, D., 2009, A tectonic synthesis of the Dun Mountain Ophiolite Belt [Ph.D.: University of Otago, 368 p.

Kelemen, P. B., Shlmlzu, N., and Saltersi, V. J., 1995, Extraction of mid-ocean-ridge basalt from the upwelling mantle by focused flow of: Nature, v. 375, p. 29.

Kimbrough, D. L., Mattinson, J. M., Coombs, D. S., Landis, C. A., and Johnston, M. R., 1992, Uranium-lead ages from the Dun Mountain ophiolite belt and Brook Street terrane, South Island, New Zealand: Geological Society of America Bulletin, v. 104, no. 4, p. 429-443.

Kimura, J.-I., and Sano, S., 2012, Reactive melt flow as the origin of residual mantle lithologies and basalt chemistries in mid-ocean ridges: Implications from the Red Hills peridotite, New Zealand: Journal of Petrology, v. 53, no. 8, p. 1637-1671.

Knaack, C. M., Cornelius, S., and Hooper, P. R., 1994, Trace element analysis of rocks and minerals by ICP-MS: Washington State University.

Koepke, J., Feig, S. T., Snow, J., and Freise, M., 2004, Petrogenesis of oceanic plagiogranites by partial melting of gabbros: an experimental study: Contributions to Mineralogy and Petrology, v. 146, no. 4, p. 414-432.

Kushiro, I., 1968, Compositions of magmas formed by partial zone melting of the Earth's upper mantle: Journal of Geophysical Research, v. 73, p. 619-634.

Lamb, W. M., 1993, Retrograde deformation within the Carthage-Colton Zone as recorded by fluid inclusions and feldspar compositions: tectonic implications for the southern Grenville Province: Contributions to Mineralogy and Petrology, v. 114, p. 379-394.

Lamb, W. M., and Popp, R. K., 2009, Amphibole equilibria in mantle rocks: Determining values of mantle aH20 and implications for mantle H2O contents: American Mineralogist, v. 94, p. 41-52.

Le Roux, V., Bodinier, J.-L., Tommasi, A., Alard, O., Dautria, J.-M., Vauchez, A., and Riches, A., 2007, The Lherz spinel lherzolite: refertilized rather than pristine mantle: Earth and Planetary Science Letters, v. 259, no. 3, p. 599-612.

Lecuyer, C., and Ricard, Y., 1999, Long-term fluxes and budget of ferric iron: implication for the redox states of the Earth's mantle and atmosphere: Earth and Planetary Science Letters, v. 165, no. 2, p. 197-211.

Lenardic, A., and Moresi, L. N., 1999, Some thoughts on the stability of cratonic lithosphere: Effects of buoyancy and viscosity: Journal of Geophysical Research, v. 104, no. B6, p. 12747.

Lenoir, X., Garrido, C. J., Bodinier, J.-L., Dautria, J.-M., and Gervilla, F., 2001, The recrystallization front of the Ronda peridotite: evidence for melting and thermal erosion of subcontinental lithospheric mantle beneath the Alboran Basin: Journal of Petrology, v. 42, no. 1, p. 141-158.

Lin, S., Jiang, D., and Williams, P. F., 1998, Transpression (or transtension) zones of triclinic symmetry: Natural example and theoretical modelling: Geological Society, London, Special Publications, v. 135, p. 41-57.

Macpherson, C. G., Dreher, S. T., and Thirlwall, M. F., 2006, Adakites without slab melting: high pressure differentiation of island arc magma, Mindanao, the Philippines: Earth and Planetary Science Letters, v. 243, no. 3, p. 581-593.

Malatesta, C., Gerya, T., Crispini, L., Federico, L., and Capponi, G., 2013, Oblique subduction modelling indicates along-trench tectonic transport of sediments: Nat Commun, v. 4, p. 2456.

Marques, F. O., Cabral, F. R., Gerya, T. V., Zhu, G., and May, D. A., 2014, Subduction initiates at straight passive margins: Geology, v. 42, no. 4, p. 331-334.

Mattinson, J. M., 2005, Zircon U–Pb chemical abrasion (“CA-TIMS”) method: Combined annealing and multi-step partial dissolution analysis for improved precision and accuracy of zircon ages: Chemical Geology, v. 220, no. 1-2, p. 47-66.

Mysen, B. O., 1973, Melting in a hydrous mantle: Phase relations of mantle peridotite with controlled water and oxygen fugacities: Carnegie Institute of Washington Yearbook, v. 72, p. 467-477.

Navon, O., and Stolper, E., 1987, Geochemical consequences of melt percolation: the upper mantle as a chromatographic column: The Journal of Geology, p. 285-307.

Nimis, P., and Grutter, H., 2010, Internally consistent geothermometers for garnet peridotites and pyroxenites: Contributions to Mineralogy and Petrology, v. 159, p. 411-427.

Nimis, P., and Taylor, W. R., 2000, Single clinopyroxene thermobarometry for garnet peridotites. Part I. Calibration and testing of a Cr-in-Cpx barometer and an enstatite-in-Cpx thermometer: Contributions to Mineralogy and Petrology, v. 139, p. 541-554.

O'Reilly, S. Y., and Griffin, W., 2013, Mantle metasomatism, Metasomatism and the Chemical Transformation of Rock, Springer, p. 471-533.

O'Neill, H. S. C., and Wall, V., 1987, The Olivine—Orthopyroxene—Spinel oxygen geobarometer, the nickel precipitation curve, and the oxygen fugacity of the Earth's Upper Mantle: Journal of Petrology, v. 28, no. 6, p. 1169-1191.

O'Reilly, S. Y., and Griffin, W., 2000, Apatite in the mantle: implications for metasomatic processes and high heat production in Phanerozoic mantle: Lithos, v. 53, no. 3, p. 217-232.

Ozawa, K., and Shimizu, N., 1995, Open-system melting in the upper mantle: Constraints from the Hayachine-Miyamori ophiolite, northeastern Japan: Journal of Geophysical Research: Solid Earth (1978–2012), v. 100, no. B11, p. 22315-22335.

Parkinson, I. J., and Pearce, J. A., 1998, Peridotites from the Izu–Bonin–Mariana forearc (ODP Leg 125): evidence for mantle melting and melt–mantle interaction in a supra-subduction zone setting: Journal of Petrology, v. 39, no. 9, p. 1577-1618.

Pearce, J. A., Lippard, S. J., and Roberts, S., 1984, Characteristics and tectonic significance of supra-subduction zone ophiolites: Geological Society, London, Special Publications, v. 16, p. 77-94.

Pearce, J., Barker, P., Edwards, S., Parkinson, I., and Leat, P., 2000, Geochemistry and tectonic significance of peridotites from the South Sandwich arc–basin system, South Atlantic: Contributions to Mineralogy and Petrology, v. 139, no. 1, p. 36-53.

Pearce, J. A., and Robinson, P. T., 2010, The Troodos ophilitic complex probably formed in a subduction initiation, slab edge setting: Gondwana Research, v. 18, no. 1, p. 60-81.

Poudjom Djomani, Y. H., Griffin, W. L., O'Reilly, S. Y., and Doyle, B. J., 2005, Lithospheric domains and controls on kimberlite emplacement, Slave Province, Canada:

Evidence from elastic thickness and upper mantle composition: Geochemistry, Geophysics, Geosystems, v. 6, no. 10, p. n/a-n/a.

Powell, R., Holland, T., and Worley, B., 1998, Calculating phase diagrams involving solid solutions via non-linear equations, with examples using THERMOCALC: Journal of Metamorphic Geology, v. 16, p. 577-588.

Rampone, E., Piccardo, G. B., Vannucci, R., and Bottazzi, P., 1997, Chemistry and origin of trapped melts in ophiolitic peridotites: Geochimica et Cosmochimica Acta, v. 61, no. 21, p. 4557-4569.

Rattenbury, M. S., Cooper, R. A., and Johnston, M. R., 1998, Geology of the Nelson area: Institute of Geological and Nuclear Sciences, scale 1:250,000.

Reagan, M. K., Ishizuka, O., Stern, R. J., Kelley, K. A., Ohara, Y., Blichert-Toft, J., Bloomer, S. H., Cash, J., Fryer, P., Hanan, B. B., Hickey-Vargas, R., Ishii, T., Kimura, J., Peate, D. W., Rowe, M. C., and Woods, M., 2010, Fore-arc basalts and subduction initiation in the Izu-Bonin-Mariana system: Geochemistry, Geophysics, Geosystems, v. 11, no. 3.

Regenauer-Lieb, K., Yuen, D. A., and Branlund, J., 2001, The initiation of subduction: criticality by addition of water?: Science, v. 294, no. 5542, p. 578-580.

Rollinson, H., and Adetunji, J., 2013, Mantle podiform chromitites do not form beneath mid-ocean ridges: A case study from the Moho transition zone of the Oman ophiolite: Lithos, v. 177, p. 314-327.

Rollinson, H., and Adetunji, J., 2015, The geochemistry and oxidation state of podiform chromitites from the mantle section of the Oman ophiolite: A review: Gondwana Research, v. 27, no. 2, p. 543-554.

Sano, S., and Kimura, J. I., 2007, Clinopyroxene REE Geochemistry of the Red Hills Peridotite, New Zealand: Interpretation of Magmatic Processes in the Upper Mantle and in the Moho Transition Zone: Journal of Petrology, v. 48, no. 1, p. 113-139.

Sano, S., Tazaki, K., Koide, Y., Nagao, T., Watanabe, T., and Kawachi, Y., 1997, Geochemistry of dike rocks in Dun Mountain Ophiolite, Nelson, New Zealand: New Zealand Journal of Geology and Geophysics, v. 40, no. 2, p. 127-136.

Shervais, J. W., 2001, Birth, death, and resurrection; the life cycle of suprasubduction zone ophiolites: Geochemistry, Geophysics, Geosystems, v. 2, no. 1, p. 45.

Shervais, J. W., Kimbrough, D. L., Renne, P., Hanan, B. B., Murchey, B., Snow, C. A., Schuman, M. M. Z., and Beaman, J., 2004, Multi-Stage Origin of the Coast Range

Ophiolite, California: Implications for the Life Cycle of Supra-Subduction Zone Ophiolites: International Geology Review, v. 46, p. 289-315.

Sisson, T. W., and Grove, T. L., 1993, Experimental investigations of the role of H2O in calc-alkaline differentiation and subduction zone magmatism: Contributions to Mineralogy and Petrology, v. 113, p. 143-166.

Sivell, W. J., and McCulloch, M. T., 2000, Reassessment of the origin of the Dun Mountain Ophiolite, New Zealand: Nd-isotopic and geochemical evolution of magma suites: New Zealand Journal of Geology and Geophysics, v. 43, p. 133-146.

Spiegelman, M., Kelemen, P. B., and Aharonov, E., 2001, Causes and consequences of flow organization during melt transport: The reaction infiltration instability in compactible media: Journal of Geophysical Research, v. 106, p. 2061-2077.

Stern, R. J., 2004, Subduction initiation: spontaneous and induced: Earth and Planetary Science Letters, v. 226, no. 3-4, p. 275-292.

Stern, R. J., and Bloomer, S. H., 1992, Subduction zone infancy: Examples from the Eocene Izu-Bonin-Mariana and Jurassic California arcs: Geological Society of America Bulletin, v. 104, no. 12, p. 1621-1636.

Stern, R. J., Reagan, M., Ishizuka, O., Ohara, Y., and Whattam, S., 2012, To understand subduction initiation, study forearc crust: To understand forearc crust, study ophiolites: Lithosphere, v. 4, no. 6, p. 469-483.

Stevenson, D. J., 1989, Spontaneous small-scale melt segregation in partial melts undergoing deformation: Geophysical Research Letters, v. 16, p. 1067-1070.

Sullivan, W. A., 2013, L tectonites: Journal of Structural Geology, v. 50, p. 161-175.

Sun, S.-S., and McDonough, W. F., 1989, Chemical and isotopic systematics of oceanic basalts: implications for mantle composition and processes: Geological Society, London, Special Publications, v. 42, no. 1, p. 313-345.

Sutherland, R., 1999, Cenozoic bending of New Zealand basement terranes and Alpine Fault displacement: A brief review: New Zealand Journal of Geology and Geophysics, v. 42, no. 2, p. 295-301.

Takazawa, E., Frey, F., Shimizu, N., Obata, M., and Bodinier, J., 1992, Geochemical evidence for melt migration and reaction in the upper mantle: Nature, v. 359, no. 6390, p. 55-58.

Taylor, W. R., 1998, An experimental test of some geothermometer and geobarometer formulations for upper mantle peridotites with application to the thermobarometry of fertile lherzolite and garnet websterite: Neues Jahrbuch fur Mineralogie, v. 172, p. 381-408.

Teyssier, C., and Tikoff, B., 1999, Fabric stability in oblique convergence and divergence: Journal of Structural Geology, v. 21, p. 969-974.

Tikoff, B., and Fossen, H., 1999, Three-dimensional reference deformations and strain facies: Journal of Structural Geology, v. 21, p. 1497-1512.

Tikoff, B., Larson, C. E., Newman, J., and Little, T., 2010, Field-based constraints on finite strain and rheology of the lithospheric mantle, Twin Sisters, Washington: Lithosphere, v. 2, no. 6, p. 418-422.

Tommasi, A., Tikoff, B., and Vauchez, A., 1999, Upper mantle tectonics: three-dimensional deformation, olivine crystallographic fabrics and seismic properties: Earth and Planetary Science Letters, v. 168, p. 173-186.

Van der Wal, D., and Bodinier, J.-L., 1996, Origin of the recrystallisation front in the Ronda peridotite by km-scale pervasive porous melt flow: Contributions to Mineralogy and Petrology, v. 122, no. 4, p. 387-405.

Vernières, J., Godard, M., and Bodinier, J. L., 1997, A plate model for the simulation of trace element fractionation during partial melting and magma transport in the Earth's upper mantle: Journal of Geophysical Research: Solid Earth (1978–2012), v. 102, no. B11, p. 24771-24784.

Walcott, R. I., 1969, Geology of the Red Hill complex, Nelson, New Zealand: Transactions of the Royal Society of New Zealand, v. 7, no. 5, p. 57-88.

Webber, C. E., Little, T., Newman, J., and Tikoff, B., 2008, Fabric superposition in upper mantle peridotite, Red Hills, New Zealand: Journal of Structural Geology, v. 30, no. 11, p. 1412-1428.

Webber, C., Newman, J., Holyoke III, C. W., Little, T., and Tikoff, B., 2010, Fabric development in cm-scale shear zones in ultramafic rocks, Red Hills, New Zealand: Tectonophysics, v. 489, p. 55-75.

Wellman, H. W., 1956, Structural outline of New Zealand: Bulletin of the New Zealand Department of Scientific and Industrial Research, p. 35.

Wood, B. J., Bryndzia, L. T., and Johnson, K. E., 1990, Mantle oxidation state and its relationship to tectonic environment and fluid speciation: Science, v. 248, no. 4953, p. 337-345.

Wood, B. J., and Virgo, D., 1989, Upper mantle oxidation state: Ferric iron contents of Iherzolite spinels by 57Fe Mössbauer spectroscopy and resultant oxygen fugacities: Geochimica et Cosmochimica Acta, v. 53, p. 1277-1291.

Woodland, A., Kornprobst, J., McPherson, E., Bodinier, J.-L., and Menzies, M., 1996, Metasomatic interactions in the lithospheric mantle: petrologic evidence from the Lherz massif, French Pyrenees: Chemical geology, v. 134, no. 1, p. 83-112.

Zimmerman, M. E., Zhang, S., Kohlstedt, D. L., and Karato, S.-i., 1999, Melt distribution in mantle rocks deformed in shear: Geophysical Research Letters, v. 26, no. 10, p. 1505-1508.

APPENDIX A

SUPPLEMENTAL TABLES FOR CHAPTER II

Sample	Plagioclase zone - RH12_23		Two tarns harzburgite - 11ES19		Two tarns harzburgite - RH12ES14	
Phase	opx*	cpx	opx	cpx	opx*	cpx (reintegrated)
Wt% oxides						
SiO2	55.20	51.47	56.32	52.85	55.14	51.94
TiO2	0.12	0.31	0.03	0.06	0.03	0.08
Al2O3	2.61	3.99	2.26	2.68	4.09	4.12
Cr2O3	0.65	1.31	0.72	1.08	0.84	1.07
Fe2O3						
FeO	6.05	2.16	5.62	2.19	5.76	2.22
MnO	0.15	0.08	0.14		0.14	
MgO	33.31	17.41	32.99	17.66	32.16	16.76
CaO	1.04	23.11	2.05	23.24	1.83	23.76
NiO	0.09	0.05	0.09		0.10	
Na2O	0.01	0.21	0.01	0.22	0.01	0.07
Total	99.23	100.1	100.21	99.99	100.10	100.02
Atomic units						
Si	1.921	1.864	1.944	1.915	1.908	1.886
AlIV	0.079	0.136	0.056	0.085	0.092	0.114
AlVI	0.028	0.034	0.036	0.029	0.075	0.063
Ti	0.003	0.008	0.001	0.002	0.001	0.002
Cr	0.018	0.038	0.020	0.031	0.023	0.031
FeIII	0.028	0.063	0.000	0.037	-0.006	0.021
FeII	0.148	0.002	0.163	0.029	0.173	0.046
Mn	0.004	0.003	0.004		0.004	
Ni	0.003	0.002	0.002		0.003	
Mg	1.728	0.940	1.698	0.954	1.658	0.908
Ca	0.039	0.896	0.076	0.902	0.069	0.925
Na	0.001	0.015	0.001	0.015	0.001	0.005
Total	4.000	4.000	4.000	4.000	4.000	4.000
Geothermometry						
2-px (Brey and Kohler, 1990)		920		910		860
Ca in Opx (Nimis and Grutter, 2010)		1000		1220		1190
2-px (Taylor, 1998)		880		880		850
Enstatite in cpx (Nimis and Taylor,		920		900		850
*Same opx as Table 2						

Table A-1 – Supplemental electron microprobe analyses and geothermometry results.

Sample ID	Rock type	Country	UTM (New Zealand Transverse Mercator projection, NZGD2000 Datum)	
RH12ES13	Plagioclase harzburgite	New Zealand	1601950 E	5381960 N
RH12ES14	Harzburgite	New Zealand	1606425 E	5388375 N
12RH14a	Plagioclase lherzolite	New Zealand	1600561 E	5380732 N
11ES19	Harzburgite	New Zealand	1604750 E	5386910 N
11ES27	Lherzolite	New Zealand	1601510 E	5389875 N
RH12-23-1	Plagioclase lherzolite	New Zealand	1602820 E	5391909 N
10ES05	Harzburgite	New Zealand	1599540 E	5380700 N
RH09_39	Plagioclase lherzolite	New Zealand	1602121 E	5385979 N
11ES15	Plagioclase lherzolite	New Zealand	1601800 E	5386565 N
11ES25	Plagioclase harzburgite	New Zealand	1604525 E	5390250 N

Table A-2 – Universal Transverse Mercator (UTM) coordinates of sample locations from Chapter II.

APPENDIX B

SUPPLEMENTAL TABLES FOR CHAPTER III

	ICP-MS Detection limits (from Knaack, unpublished data)	RH12_22_3 duplicate analysis
La ppm	0.007	0.056
Ce ppm	0.012	0.121
Pr ppm	0.009	0.017
Nd ppm	0.045	0.114
Sm ppm	0.014	0.057
Eu ppm	0.010	0.038
Gd ppm	0.026	0.137
Tb ppm	0.007	0.029
Dy ppm	0.024	0.209
Ho ppm	0.006	0.047
Er ppm	0.021	0.148
Tm ppm	0.006	0.024
Yb ppm	0.023	0.161
Lu ppm	0.007	0.026
Ba ppm	0.258	0.946
Th ppm	0.009	0.029
Nb ppm	0.018	0.018
Y ppm	0.015	1.192
Hf ppm	0.032	0.028
Ta ppm	0.014	0.029
U ppm	0.014	DL
Pb ppm	0.204	DL
Rb ppm	0.057	0.144
Cs ppm	0.014	DL
Sr ppm	0.115	6.435
Zr ppm	0.059	0.531

Table B-1 – Detection limits for the ICP-MS and duplicate analysis results.

Plateau complex	Total	Olivine	Cpx	Opx	Spinel	Plag	Matrix
11ES15	562	0.573	0.142	0.214	0.021	0.050	0.000
12RH14a	612	0.644	0.123	0.170	0.018	0.046	0.000
RH12ES10	645	0.972	0.009	0.005	0.014	0.000	0.000
RH12ES12	548	0.759	0.100	0.093	0.009	0.038	0.000
12RH07	563	0.641	0.036	0.300	0.023	0.000	0.000
12RH29	542	0.980	0.011	0.002	0.007	0.000	0.000
RH12ES13	511	0.759	0.039	0.153	0.020	0.029	0.000
RH04_52	267	0.730	0.075	0.172	0.000	0.022	0.000
RH04_24	513	0.827	0.029	0.138	0.006	0.000	0.000
RH04_19B	543	0.967	0.000	0.004	0.029	0.000	0.000
RH04_8B	512	0.613	0.057	0.309	0.021	0.000	0.000
RH04_89	503	0.797	0.004	0.189	0.010	0.000	0.000
RH04_90	521	0.760	0.002	0.228	0.010	0.000	0.000
RH04_21	508	0.789	0.026	0.159	0.026	0.000	0.000
Two tarns harzburgite							
11ES19	756	0.747	0.015	0.212	0.022	0.000	0.000
12RH22	652	0.798	0.002	0.198	0.003	0.000	0.000
RH12ES14	546	0.595	0.022	0.170	0.027	0.000	0.185
Ellis Stream complex							
12RH27	580	0.629	0.000	0.207	0.009	0.155	0.000
12RH19b	687	0.818	0.076	0.095	0.012	0.000	0.000
12RH26a	546	0.886	0.005	0.093	0.015	0.000	0.000
12RHES01	585	0.916	0.000	0.000	0.039	0.044	0.000
12RHES04b	516	0.928	0.016	0.010	0.023	0.023	0.000
Plagioclase zone							
12RH24	473	0.634	0.129	0.184	0.000	0.053	0.000
12RH25	565	0.660	0.088	0.221	0.005	0.025	0.000
RH12_23_2	516	0.651	0.079	0.267	0.002	0.000	0.000
RH04_83	500	0.968	0.000	0.000	0.010	0.022	0.000
11ES25	508	0.746	0.022	0.179	0.026	0.028	0.000

Table B-2 – Point count results, given as fractional values.

Sample ID	Rock type	Country	UTM (New Zealand Transverse Mercator projection, NZGD2000 Datum)	
RH12ES01	Plagioclase dunite	New Zealand	1601750 E	5389700 N
RH12 ES02	Plagioclase harzburgite	New Zealand	1601730 E	5389740 N
12RHES04b	Plagioclase dunite	New Zealand	1601240 E	5389995 N
RH12ES10	Dunite	New Zealand	1601315 E	5383705 N
RH12ES12	Plagioclase lherzolite	New Zealand	1601850 E	5382610 N
RH12ES13	Plagioclase harzburigite	New Zealand	1601950 E	5381960 N
RH12ES14	Harzburgite	New Zealand	1606425 E	5388375 N
12RH7	Harzburgite	New Zealand	1599943 E	5380808 N
12RH10	Lherzolite	New Zealand	1602669 E	5382928 N
12RH14a	Plagioclase lherzolite	New Zealand	1600561 E	5380732 N
12RH14b	Harzburgite	New Zealand	1600561 E	5380732 N
12RH19b	Lherzolite	New Zealand	1601080 E	5387499 N
12RH22	Harzburgite	New Zealand	1602371 E	5385669 N
12RH23	Dunite	New Zealand	1602339 E	5385720 N
12RH24	Plagioclase lherzolite	New Zealand	1602299 E	5385779 N
12RH25	Plagioclase lherzolite	New Zealand	1602121 E	5385979 N
12RH26a	Harzburgite	New Zealand	1600840 E	5387299 N
12RH27	Harzburgite	New Zealand	1600107 E	5387117 N
12RH28	Harzburgite	New Zealand	1602108 E	5386721 N
12RH29	Dunite	New Zealand	1602108 E	5386721 N
12RH33	Dunite	New Zealand	1601951 E	5386121 N
11ES05	Harzburgite	New Zealand	1604650 E	5388275 N
11ES12	Harzburgite	New Zealand	1600450 E	5387110 N
11ES15	Plagioclase lherzolite	New Zealand	1601800 E	5386565 N
11ES19	Harzburgite	New Zealand	1604750 E	5386910 N
11ES24	Harzburgite	New Zealand	1604050 E	5390120 N
11ES25	Plagioclase harzburgite	New Zealand	1604525 E	5390250 N
11ES26	Harzburgite	New Zealand	1602810 E	5389440 N
11ES27	Lherzolite	New Zealand	1601510 E	5389875 N
RH12-14a	Lherzolite	New Zealand	1600561 E	5380732 N
RH12-18-2	Harzburgite	New Zealand	1601954 E	5392605 N
RH12-22-3	Plagioclase lherzolite	New Zealand	1601408 E	5392822 N
RH12-23-1	Plagioclase lherzolite	New Zealand	1602820 E	5391909 N
RH12-23-2	Lherzolite	New Zealand	1602820 E	5391909 N
10ES05	Harzburgite	New Zealand	1599540 E	5380700 N
RH09_39	Plagioclase lherzolite	New Zealand	1602121 E	5385979 N
RH09_56	Plagioclase lherzolite	New Zealand	1601733 E	5387752 N

Table B-3 - Universal Transverse Mercator (UTM) coordinates of sample locations from Chapter III.

APPENDIX C

SUPPLEMENTAL FIGURES AND TABLES FOR CHAPTER IV

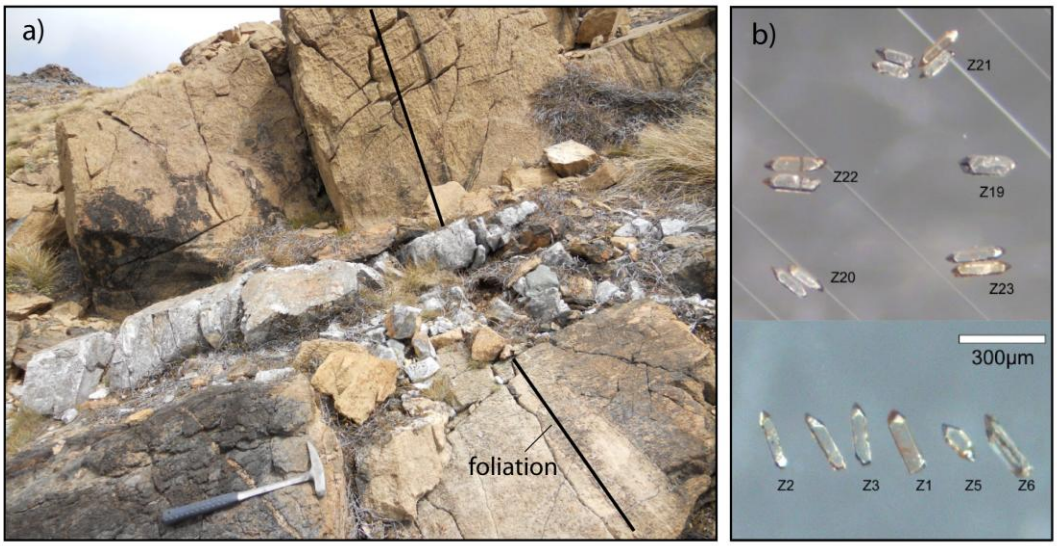

Figure C-1 – a. Outcrop photo of plagiogranite dike samples for U-Pb zircon geochronology. Note the dike cross-cuts the mantle foliation. b. Separated zircons analyzed.

	Compositional Parameters							Radiogenic Isotope Ratios										Isotopic Ages					
Sample (# grains) (a)	U (ng) (b)	Th/U (c)	Pb (pg) (b)	$^{206}Pb^*$ x10^{-13} mol (d)	mol% $^{206}Pb^*$ (d)	$Pb^*/P b_c$ (d)	Pb_c (pg) (d)	$^{206}Pb/^{204}Pb$ (e)	$^{208}Pb/^{206}Pb$ (f)	$^{207}Pb/^{206}Pb$ (f)	% err (g)	$^{207}Pb/^{235}U$ (f)	% err (g)	$^{206}Pb/^{238}U$ (f)	% err (g)	corr. coef.	$^{207}Pb/^{206}Pb$ (h)	± (g)	$^{207}Pb/^{235}U$ (h)	± (g)	$^{206}Pb/^{238}U$ (h)	± (g)
12RH35																							
(Z1) single prismatic grain	217.53	0.262	12.5	0.396	91.0%	2.9	3.21	203	0.083	0.052034	1.509	0.313270	1.713	0.043665	0.352	0.646	286.9	34.5	276.7	4.1	275.5	0.9
(Z2) single prismatic grain	121.81	0.347	6.5	0.221	93.6%	4.4	1.21	293	0.111	0.052108	1.649	0.312250	1.858	0.043461	0.514	0.523	290.2	37.7	275.9	4.5	274.2	1.4
(Z3) single prismatic grain	82.7	0.268	6.2	0.151	82.2%	1.3	2.67	103	0.085	0.052066	3.400	0.313797	3.68	0.043711	0.568	0.552	288.3	77.7	277.1	8.9	275.8	1.5
(Z5) single prismatic grain	115.99	0.285	10.9	0.211	74.9%	0.8	5.88	72	0.091	0.052473	3.826	0.316199	4.16	0.043704	0.838	0.483	306.1	87.1	279.0	10.1	275.8	2.3
(Z6) single prismatic grain	292.7	0.266	14.7	0.53	94.9%	5.4	2.32	363	0.084	0.051787	1.086	0.310314	1.255	0.043459	0.288	0.662	276.0	24.9	274.4	3.0	274.2	0.8
(Z19) single prismatic grain	238.16	0.251	11.3	0.432	96.7%	8.5	1.19	567	0.080	0.051971	1.003	0.311432	1.205	0.043461	0.449	0.598	284.1	22.9	275.3	2.9	274.3	1.2
(Z20) two prismatic grains	179.07	0.288	10	0.324	91.9%	3.3	2.34	227	0.091	0.051607	1.878	0.308977	2.068	0.043423	0.399	0.552	268.0	43.1	273.4	5.0	274.0	1.1
(Z21) four prismatic grains	352.16	0.282	17.1	0.639	96.1%	7.2	2.09	478	0.089	0.051740	0.953	0.310237	1.133	0.043488	0.325	0.653	273.9	21.8	274.4	2.7	274.4	0.9
(Z22) two prismatic grains	226.98	0.282	11.4	0.412	95.1%	5.6	1.72	378	0.088	0.051203	1.324	0.307037	1.498	0.043491	0.315	0.626	250.0	30.5	271.9	3.6	274.4	0.8
(Z23) two prismatic grains	288.85	0.279	13.4	0.524	97.5%	11.4	1.08	750	0.088	0.051290	0.896	0.307409	1.042	0.043469	0.305	0.592	253.9	20.6	272.2	2.5	274.3	0.8

(a) Z1, Z2 etc. are internl laboratory labels for fractions composed of single zircon grains or two-grain aliquots; all fractions annealed and chemically abraded after Mattinson (2005).

(b) U and total Pb content of zircon remnants after chemical abrasion.

(c) Model Th/U ratio calculated from radiogenic 208Pb/206Pb ratio and 207Pb/235U age.

(d) Pb* and Pbc represent radiogenic and common Pb, respectively; mol % 206Pb* with respect to radiogenic, blank and initial common Pb.

(e) Measured ratio corrected for spike and fractionation only.

Daly Pb analyses corrected for 0.22%/AMU mass bias based on repeat analysis of NBS-981.Faraday U analyses corrected for mass bias based on measured 233U/235U ratio.

(f) Corrected for fractionation, spike, and common Pb; up to 1 pg of common Pb was assumed to be procedural blank: 206Pb/204Pb = 18.66 ± 0.60%; 207Pb/204Pb = 15.54 ± 0.25%;

208Pb/204Pb = 37.62 ± 0.55% (all uncertainties 1-sigma). Excess over blank was assigned to initial common Pb.

(g) Errors are 2-sigma, propagated using the algorithms of Schmitz and Schoene (2007) and Crowley et al. (2007).

(h) Calculate ages are based on the decay constants of Jaffey et al. (1971).

Table C-2 – U-Pb isotopic data for plagiogranite sample 12RH35.